이학박사학위논문

Dynamic Force Spectroscopy for Studies of the Nanometric Water Column

나노 크기 물기둥 연구를 위한 동역학적 힘의 분석

2014년 2월

서울대학교 대학원

물리·천문학부

김 종 우

Dynamic Force Spectroscopy for Studies of the Nanometric Water Column

by

Jongwoo Kim, B.S.

Supervised by

Professor Wonho Jhe

A Dissertation Submitted to the Faculty of

Seoul National University

in Partial Fulfillment of the Requirements

for the Degree of

Doctor of Philosophy

February 2014

Department of Physics and Astronomy

The Graduate School

Seoul National University

Dynamic Force Spectroscopy for Studies of the Nanometric Water Column

나노 크기 물기둥 연구를 위한 동역학적 힘의 분석

지도교수 **제 원 호**

이 논문을 이학박사학위논문으로 제출함

2013년 11월

서울대학교 대학원

물리·천문학부

김 종 우

김종우의 박사학위논문을 인준함

2013년 12월

위 원 장 박 건 식 印

부위원장 제 원 호 印

위 원 홍 승 훈 印

위 원 이 규 철 印

위 원 곽 호 영 印

Abstract

Dynamic Force Spectroscopy for Studies of the Nanometric Water Column

Jongwoo Kim

Department of Physics and Astronomy

The Graduate School

Seoul National University

Water at interfaces plays a crucial role in various fields. In particular, a water column formed naturally between solid surfaces is the size of nanometer scale due to roughness of the surfaces. It is important for natural phenomena such as adhesion, friction and for nanotechnology scanning probe microscope, microelectromechanical systems. An atomic force microscope (AFM) based on a quartz tuning fork (QTF) is set up to investigate the dynamics of the nanometric water column. Particularly, a preamplifier with linear response for QTFs of different eigenfrequencies is composed. Also, an optimum QTF is determined to be used as a force sensor in atomic force microscopy based on measurements of piezoelectric coupling constant, response time and noise level of the QTFs. [Chapter 2]

The determination of the stiffness of quartz tuning fork is very important to quantitatively measure tiny forces interacting at the nanometer scale. The

stiffness of the quartz tuning fork as well as the qPlus sensor, in which one prong of QTF is firmly fixed, is investigated. The formulas to calculate the spring constant of both quartz tuning fork and qPlus sensor are established, the stiffness of QTF and qPlus sensor with different eigenfrequencies is measured by using the mass-attachment method. It is demonstrated that the suggested formulas are very consistent with the experimental results; however, the formula that has been widely employed to estimate the spring constant of cantilever is found to cause significant error. Comparing the spring constant of QTF with that of qPlus sensor, in addition, it is shown that the spring constant of QTF is twice as much as that of qPlus sensor with no remarkable coupling stiffness between two prongs of QTF. [Chapter 3]

It is crucial to quantify the noise level and understand the minimum detectable force in atomic force microscopy. A new method to determine the minimum detectable force in atomic force microscopy by quantifying the noise level is presented. In addition, it is investigated how the control of quality factor (so-called Q-control) affects the minimum detectable force. It is shown that the signal-to-noise ratio does not change by the Q-control. In constrast, it is found that the minimum detectable force can be adjusted by the Q-control even though the signal-to-noise ratio remains constant. It is attributed to the frequency noise that is inversely proportional to the effective quality factor. In addition, the optimization of the force sensitivity is discussed on the basis of the relation between the minimum detectable force and the response time of force sensor. [Chapter 4]

The mechanical properties of the water column formed in ambient condition are measured by using the non-contact atomic force microscope based on the QTF. In particular, it is observed that the mechanical relaxation time of the water column increases with the elongation of the bridge by increasing the tip-sample distance. On the other hand, its dependence on the volume of the bridge is not found. The increase of the relaxation time during elongation may be attributed to the increased surface of the bridge. These results could provide an insight into the water nanobridge formed in ambient conditions as well as the nanoconfined water in other systems. [Chapter 5]

A novel technique called time-resolved dynamic force spectroscopy to observe the temporal changes of dynamic properties of nanomaterials is presented. Applying the time-resolved spectroscopy to the formation and growth of the nanometric water column, it is demonstrated that an activation time to form the nanometric water column can be quantitatively measured. The results provide experimental evidence that the approach rate rises the effective temperature when the nanometric water meniscus is formed. In addition, the growth of the nanometric water column can be very slow; thus, it takes up to several seconds, which may indicate that the diffusion process is very slow for its growth. An experimental evidence that a periodic approach of the tip and sample enhances the effective temperature in the formation process of the nanometric water column is presented. It is demonstrated that the effect of the thermal drift at nanoscale during measurements is extracted and compensated. [Chapter 6]

In summary, the atomic force microscopy for studies of the nanometric water column based on a quartz tuning fork is investigated. The method to determine the spring constant of QTF, the most important property for quantitative force measurements, is also presented and it is demonstrated that the suggested formula agrees well with the experimental measurements. In addition, the quantifying method of noise on interaction force is suggested and by introducing the method, it is shown that Q-control may be employed to optimize the force sensitivity in the amplitude-modulation AFM. It is also found that the mechanical relaxation time of the water nanobridge increases as it is elongated; however, its dependence on the volume is found to be not relevent. It suggests that the increase of the mechanical relaxation time during elongation may be attributed to the increased surface of the bridge, and that the non-contact AFM may be a novel tool to study the mechanical properties of water at air/water interface. This advanced techniques of atomic force microscopy based on a quartz tuning fork is expected to be an important tool to investigate the dynamic properties of not only the nanometric water column but also nanomaterials.

Keywords: viscoelasticity, relaxation time, quartz tuning fork, noise, time-resolved dynamic force spectroscopy

Student number: 2007-20412

Contents

List of Figures

Chapter 1

Introduction

1.1 The properties of water at interfaces

Understanding the interfacial water is very important in a wide range of science and technology such as friction, adhesion, protein folding, hydrophobic interaction, scanning probe microscopy and microelectromechanical systems. For example, the relative humidity and its exposing time affect the stability of granular materials such as sand piles. [1, 2] Here, the interfacial water plays a crucial role to enhance the adhesion force by the formation of water bridge between their asperities. Furthermore, the enhanced adhesion force also increase the friction between two solid surfaces. [3–5] The water channel also plays a key role in molecular transport in dip-pen nanolithography. [6]

Due to both of its scientific and technological importance, many studies have been mainly paid attention to the interfacial water confined between two

hydrophilic surfaces down to 3-4 monolayers. The mechanical properties, especially viscosity, of the confined water have been widely investigated by using surface force apparatus. Klein and his co-workers reported that the effective viscosity of the confined water is within three times of its bulk value, [7] whereas the effective viscosity of confined octamethylcyclotetrasiloxane (OMCTS) is found to be at least seven orders of magnitude increased. [8] Granick group reported that the effective viscosity of water confined between two mica crystals varied by orders of magnitude as the twist angle of two surfaces was changed. [9] On the basis of this observation, the authors suggested that the effective viscosity of ultrathin liquid depends on how much the confining lattice are aligned.

The viscoelastic properties of nanoconfined water between two hydrophilic surfaces have been also studied by using atomic force microscopy (AFM). Riedo group reported that the intrinsic relaxation time of the nanoconfined water is in the range from 100 milliseconds to 100 microseconds, which shows very slow dynamic behavior of the water similar to that found in metastable complex fluids. [10] Hoffmann and his co-workers showed that the elastic and viscous response of nanoconfined films changes dramatically when the approach speed is increased. [11]

Optical measurements have been shown that the water molecules at the vapor/water interface form an approximately icelike hydrogen-bonding network, even though the network is expected to be highly disordered. [12] However, the mechanical properties of water at the vapor/water interface have been still poorly understood. The nanometric water column between the tip and sam-

ple in AFM has high surface-to-volume ratio, thus the effect of water at the vapor/water interface to its mechanical properties would be enormous. In this dissertation, it will be presented how different the mechanical properties of water at vapor/water interface is from its bulk state by touching the water directly using AFM.

1.2 Interfacial water studied by atomic force microscopy

The submicrometer water bridge can be formed using a sharp tip with radius of 10-100 nm in AFM, and it represents the water existing between two hydrophilic surfaces in a single asperity. Studies about friction affected by the water bridge [4, 13–15] as well as adhesion [16, 17] using the AFM have been numerously investigated. Riedo group showed that the time required to form the water bridge grows as temperature decreases, which indicates that the formation of the water bridge is a thermally-activated process. [5]

Under the AFM configuration, theoretical investigations were performed to understand the nanometric water meniscus. The interaction force between two solids mediated by liquid meniscus was studied by Bhushan and his co-workers. [18, 19] Jang and his co-workers have studied the shape, size and force as a function of tip-sample distance by using Monte Carlo method and molecular simulation. [20–22] The formation, rupture and hysteresis of the capillary water bridge as a function of tip-sample distance were investigated by Zhang and his

co-workers. [23, 24]

As experimental studies, it was shown that the nanoscopic water bridge is not in thermodynamically equilibrium but in almost constant volume when it is stretched. [25] The measured viscosity of the water meniscus between two hydrophilic surfaces is seven orders of magnitude larger than that of bulk water, which results from a cooperative effect of hydrogen bonding of water molecules. [26] Experimental studies of the nanometric water column are somewhat less vigorous than the theoretical ones because it is diffcult manipulating the water column using the commercial AFM due to its mechanical instability.

To overcome the mechanical instability (so-called jump-to-contact instability), another type of AFM based on a quartz tuning fork (QTF) is introduced, [27–29] which allows to study the nanometric water column with avoiding the tip-sample contact. In particular, an unusual stepwise decrease of the elasticity associated with the nanometric water column was observed during its stretch. [27] Such elasticity indicates stick-slip in atomic scale at the water-tip interface. In addition, the mechanical properties such as elasticity, viscosity and dissipation energy of the water column were also measured during its manipulation. [28]

In the experimental studies using QTF-based AFM, it is still lack of quantitative measurements of the mechanical properties of the nanometric water column. In particular, it has been still debated on the effective stiffness of QTF, [30–32] which is the most important property in quantitative analysis of force. To resolve this, a novel method to calculate and experimentally determine the

effective stiffness of QTF will be also presented. Besides, not only a method for quantifying the noise on the amplitude, phase and force gradient in AFM but also the effect of Q-control on the interaction force gradient will be addressed in this dissertation. It is expected that to be associated with how small the water column can be measured in the AFM.

1.3 Outline of this thesis

The focus of this dissertation is QTF-AFM for investigating the mechanical properties of nanometric water column and its kinetics.

In Chapter 2, a dynamic force microscope (DFM) based on a quartz tuning fork (QTF) is set up to study the mechanical properties and kinetics of the nanometric water column. A preamplifier with linear response for QTFs of different eigenfrequencies is introduced. In addition, based on measurements of piezoelectric coupling constant, response time, and noise level of the QTFs, the performance of the QTFs is confirmed, and an optimum QTF for a force sensor used in atomic force microscopy is determined.

In Chapter 3, the effective stiffness of qPlus sensor and QTF is investigated by using various kinds of quartz resonators for quantitative force measurements. The stiffness of each qPlus sensor and QTF is experimentally determined by the mass-attachment method. It is compared with that calculated by the suggested formula as well as that estimated by the cantilever beam theory. The stiffness calculated by the cantilever beam theory is found to be overesti-

mated, whereas that calculated by the suggested formula is consistent with the measured one. It is also demonstrated that the effective stiffness of QTF is twice that of qPlus sensor, which agrees well with the recently proposed model.

In Chapter 4, a method to quantify the noise on force gradient and to control of force sensitivity in Q-controlled amplitude modulation (AM)-AFM is presented. It is found that the phase noise determined by its standard deviation in time domain is identical to the amplitude noise divided by oscillation amplitude in AM-AFM. In particular, it is observed that while Q-control does not adjust the signal-to-noise ratio, it changes the detection sensitivity because the minimum detectable force gradient is inversely proportional to the effective quality factor for large bandwidths, which is due to reduction of frequency noise.

In Chapter 5, the mechanical properties of the water nanobridge as a function of the tip-sample distance is presented. Its mechanical relaxation time becomes longer as it is stretched by increasing the tip-sample distance. On the other hand, it is observed that the relaxation time is not relevant to the volume of the water nanobridge. It may suggest that the mechanical relaxation time does not depend on the size of the nanobridge, but does depend on its shape.

In Chapter 6, time-resolved dynamic force spectroscopy technique and its applications are presented. Using this technique, the formation process of the nanometric water column is found to be an activation process which accompanies an incubation delay, which provides experimental evidence that periodic movement of the tip and sample is responsible for an increase of effective temperature in the formation process. The growth of the nanometric water column

is also observed in real time, and the time constant of growth is found to be up to several seconds. In addition, it is demonstrated that a simple method allows to determine and compensate the effect of thermal drift in force spectroscopy.

References

[1] L. Bocquet, E. Charlaix, S. Ciliberto, and J. Crassous, Nature **396**, 735 (1998).

[2] T. C. Halsey and A. J. Levine, Phys. Rev. Lett. **80**, 3141 (1998).

[3] *Sliding Friction: Physical Principles and Applications*, 2nd ed., edited by B. N. J. Persson (Springer-Verlag, Berlin, 2000).

[4] E. Riedo, F. Levy, and H. Brune, Phys. Rev. Lett. **88**, 185505 (2002).

[5] R. Szoszkiewicz and E. Riedo, Phys. Rev. Lett. **95**, 135502 (2005).

[6] R. D. Piner *et al.*, Science **283**, 661 (1999).

[7] U. Raviv, P. Laurat, and J. Klein, Nature **413**, 51 (2001).

[8] J. Klein and E. Kumacheva, Science **269**, 816 (1995).

[9] Y. Zhu and S. Granick, Phys. Rev. Lett. **87**, 096104 (2001).

[10] T.-D. Li and E. Riedo, Phys. Rev. Lett. **100**, 106102 (2008).

[11] S. H. Khan, G. Matei, S. Patil, and P. M. Hoffmann, Phys. Rev. Lett. **105**, 106101 (2010).

[12] Y. R. Shen and V. Ostroverkhov, Chem. Rev. **106**, 1140 (2006).

[13] K. B. Jinesh and J. W. M. Frenken, Phys. Rev. Lett. **96**, 166103 (2006).

[14] K. B. Jinesh and J. W. M. Frenken, Phys. Rev. Lett. **101**, 036101 (2008).

[15] C. Greiner *et al.*, Nano Lett. **10**, 4640 (2010).

[16] J. Grobelny, N. Pradeep, D.-I. Kim, and Z. C. Ying, Appl. Phys. Lett. **88**, 091906 (2006).

[17] O. Noel, P.-E. Mazeran, and H. Nasrallah, Phys. Rev. Lett. **108**, 015503 (2012).

[18] T. Stifter, O. Marti, and B. Bhushan, Phys. Rev. B **62**, 13667 (2000).

[19] S. Cai and B. Bhushan, Nanotechnology **18**, 465704 (2007).

[20] J. Jang, G. C. Schatz, and M. A. Ratner, Phys. Rev. Lett. **92**, 085504 (2004).

[21] H. J. Choi *et al.*, Mol. Simulat. **35**, 466 (2009).

[22] H. Kim, B. Smit, and J. Jang, J. Phys. Chem. C **116**, 21923 (2012).

[23] Y. Men, X. Zhang, and W. Wang, J. Chem. Phys. **131**, 184702 (2009).

[24] Y. Men, X. Zhang, and W. Wang, J. Chem. Phys. **134**, 124704 (2011).

[25] L. Sirghi, R. Szoszkiewicz, and E. Riedo, Langmuir **22**, 1093 (2006).

[26] R. C. Major *et al.*, Phys. Rev. Lett. **96**, 177803 (2006).

[27] H. Choe *et al.*, Phys. Rev. Lett. **95**, 187801 (2005).

[28] M. Lee, B. Sung, N. Hashemi, and W. Jhe, Faraday Discuss. **141**, 415 (2009).

[29] S. An *et al.*, Appl. Phys. Lett. **101**, 053114 (2012).

[30] G. H. Simon, M. Heyde, and H.-P. Rust, Nanotechnology **18**, 255503 (2007).

[31] A. Castellanos-Gomez, N. Agraït, and G. Rubio-Bollinger, Nanotechnology **20**, 215502 (2009).

[32] F. J. Giessibl *et al.*, Phys. Rev. B **84**, 125409 (2011).

Chapter 2

Experimental Setup

2.1 System overview

Atomic force microscope (AFM) has been employed to investigate the interfacial water in many studies. In detail, AFM based on a cantilever as a force sensor has usually introduced to study the mechanical properties of the nanoconfined water between two solid surfaces [1–4] in water or to investigate the water meniscus formed in ambient conditions or its effect on friction. [5–7] For the case of the water meniscus, it gives rise to the capillary force which is larger than the order of several nanonewtons. The cantilever is in general too compliant to withstand such an attraction force, which causes a hysteresis during approach-retraction cycle. [8, 9] It indicates that the manipulation of the water bridge is difficult when cantilever is employed as a force sensor.

Several conditions of the force sensor in AFM would be considered for

investigation of the nanometric water column as follows. (1) The stiffness of the force sensor should be high enough to avoid the mechanical instability due to the water column and other attractive forces. (2) The sensor allows a small oscillation amplitude to keep the pertubation on the water column as small as possible. (3) The sensor has small dissipation itself to minimize the effect the dissipation on the water column.

Quartz tuning fork (QTF) has been often introduced in AFM to fulfill the conditions. In general, QTF has stiffness in the order of kN/m and high sensitivity because of its high quality factor. In addition, small oscillation of subnanometer is also possible by using QTF. It also allows a self-sensing due to its piezoelectricity, without any optical detection which provide energy to the sample or the water column. [10] Another advantage of using QTF is mounting custom tips of considerable size, which gives a wide choise of tip which has different materials and radii. [11]

Figure 2.1 shows a schematic diagram of the QTF-based amplitude-modulation atomic force microscope (AM-AFM). The equipped QTF is actuated by a function generator (33220A, Agilent Technologies) by applying voltage between two electrodes via the piezoelectric properties of quartz. To oscillate the QTF in the order of a subnanometer, a home-made voltage divider is introduced between the function generator and the QTF. The gain of the voltage divider was measured to be $G_{\mathrm{VD}} = 1.021 \times 10^{-3}$ (see Appendix A). The preamplifier is composed of an operational amplifier (LF357N, National Semiconductor) and a resistor with nominal resistance of 10 MΩ, which amplifies the current flow-

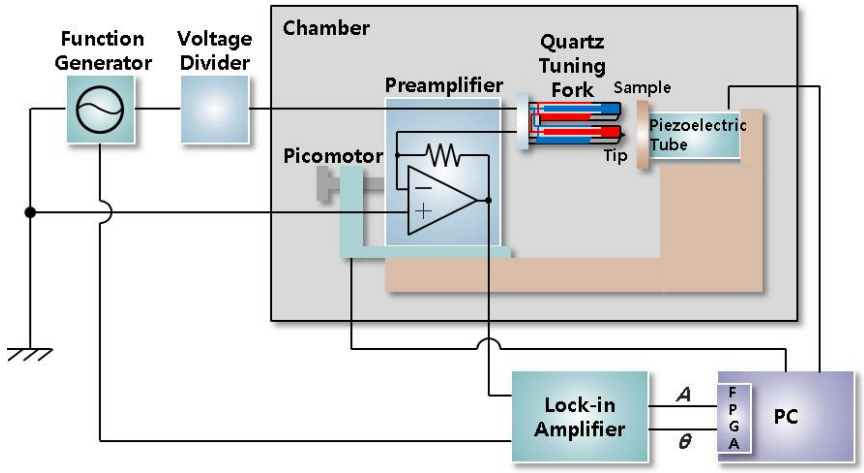

Figure 2.1: The schematic diagram of atomic force microscope based on quartz tuning fork is depicted.

ing out from the QTF. A lock-in amplifier (SR830, Stanford Research Systems) is employed to measure the amplitudes and the phase differences of the output voltage of the preamplifier. A picomotor (New Focus) and piezoelectric tube (PI) control the tip-sample distance coarsely and finely, respectively. The amplitude and the phase difference signals are recorded by a computer and the tip-sample distance is controlled by applying feedback potentials to the piezoelectric transducer on which the sample is attached in response to the signal change. The computer is equipped with a field programmable gate array (FPGA) module which allows fast measurements (see Appendix D for more details).

The tip oscillates laterally to the sample keeps the tip-sample distance fixed during the oscillation. It provides an advantage in quantitative measurements of the mechanical properties of the water column between solid surfaces

Furthermore, the distance-dependent forces such as the van der Waals force are not detected.

The head part of the AFM consists of a QTF, preamplifier and piezoelectric transducer measures the force as a function of the tip-sample distance. The components of the head part are attached onto a small single-body brass to reduce the thermal drift which is critical for the tip-sample distance regulation. In addition, the head part is enclosed by an acrylic chamber with thickness of 15 mm to maintain the temperature and humidity conditions. The relative humidity is controlled by flowing dry nitrogen and water vapor through the chamber.

In this setup, seven different kinds of QTFs which have various eigenfrequencies of tens of kilohertz, QTF-A (C-005R, 32.768 kHz), QTF-B (C-004R, 32.768 kHz), QTF-C (C-002RX, 32.768 kHz), QTF-D (C-2 type, 20.0 kHz), QTF-E (C-2 type, 65.535 kHz), QTF-F (C-2 type, 76.8 kHz) and QTF-G (C-2 type, 100 kHz)* were tested. The objectives of this test is 1) to find the more appropriate QTF to investigate the properties of the water column quantitatively and 2) to study the mechanical properties of the water column dependent on the driving frequency later.

First of all, a preamplifier which supports various kinds of QTF with different eigenfrequencies. LF357N (National Semiconductor) allows a linear response over the range from 20 to 100 kHz. With 10 MΩ of nominal resistance, it is shown that the preamplifier has the I-V gain of 11.6 MΩ (see Section 2.2

*The QTFs tested are available from Epson-Toyocom Corporation

for more details). The effective stiffness (see Chapter 3 for more details) and the piezoelectric coupling constant (see Section 2.3) of QTF were determined. In addition, the response time of QTF was also determined and found to be consistent with the theoretical expectation (Section 2.4). Lastly, the noise on the interaction stiffness of QTFs was determined by using the measured effective stiffness and piezoelectric coupling constant of each QTF (see Section 2.5). It was found that QTF-C (C-002RX, 32.768 kHz) is the most appropriate QTF to study the mechanical properties of the nanometric water column on the basis of its noise level and cost.

2.2 Preamplifier for quartz tuning forks

To produce an electrical deflection signal, the QTF needs only one more component, the preamplifier, which is a current-to-voltage amplifier that converts the flowing charge from the QTF into a voltage. The current-to-voltage (I-V) gain of the preamplifier is dependent on the driving frequency in general. Therefore, the model which includes a parasitic capacitance connected in parallel to a resistance has often been considered. [12,13] To measure the frequency response of the I-V gain, we have applied five capacitors of different capacitances to provide current to the preamplifier.

According to the results shown in Fig. 2.2(a), the measured gain of the preamplifier G is proportional to the driving frequency f and thus Z_{G} can be extracted from the slope of plot in Fig. 2.2(b). It is worth noting that the

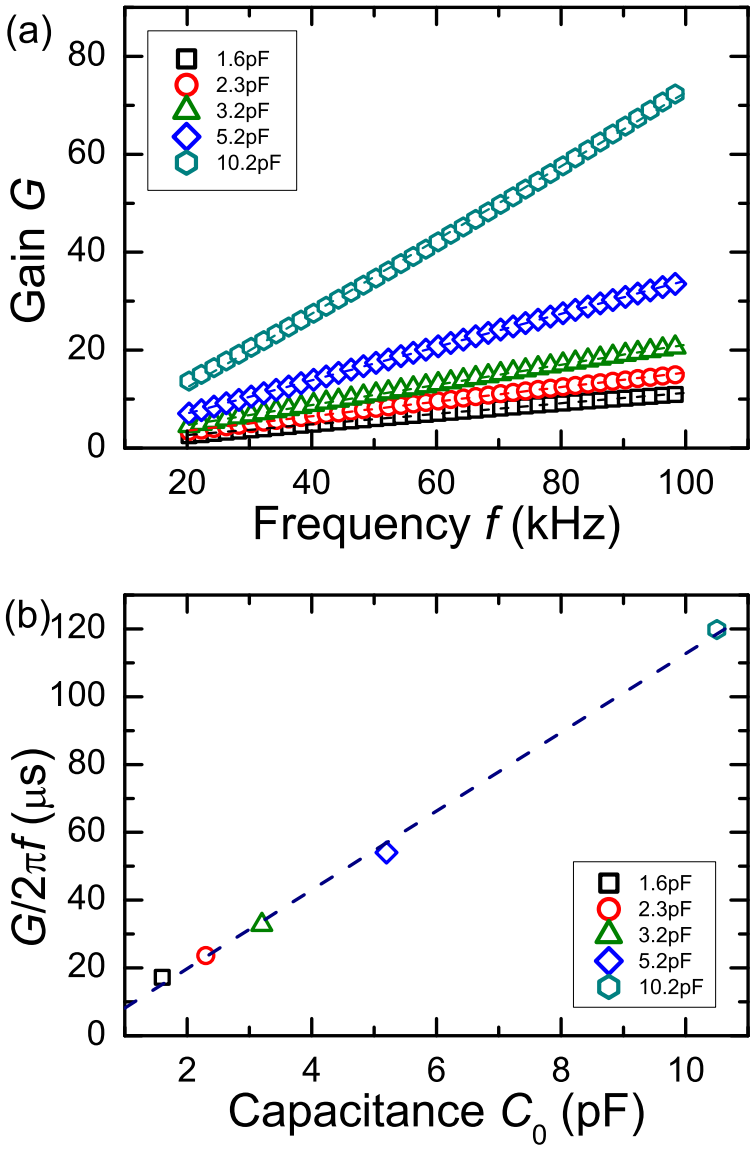

Figure 2.2: (a) Linearity of the gain as a function of the driving frequency is shown. (b) The gain divided by the driving frequency versus the capacitance is depicted. The I-V gain $Z_{\rm G}$ is extracted by using several test capacitors.

operational amplifier LF357N gives the linear response, whereas the dependence of G on f is not linear when LF356N is employed as a operational amplifier (see Appendix A for more details). Figure 2.2(b) shows G divided by f as a function of the test capacitance C_0 obtained by using different capacitances.

Let $V_{\rm out}$ be the voltage output from the preamplifier when the test capacitor of capacitance C_0 is driven by a voltage $V_{\rm d}$ at the driving frequency f. Then $V_{\rm out}$ is given by

$$V_{\rm out}(f) = Z_{\rm G}(f) \cdot 2\pi f \cdot C_0 V_{\rm d}, \tag{2.1}$$

where $Z_{\rm G}(f)$ is the I-V gain of the preamplifier, which is dependent on f, in general. Let G be the gain of this system, the ratio of $V_{\rm out}$ to $V_{\rm d}$, given by

$$G(f) = \frac{V_{\rm out}(f)}{V_{\rm d}} = Z_{\rm G}(f) \cdot 2\pi f \cdot C_0. \tag{2.2}$$

Note that the gain G is proportional to the test capacitance C_0 and the I-V gain $Z_{\rm G}$.

The measured I-V gain $Z_{\rm G}$ is 11.6 MΩ, independent of the driving frequency over the range from 20 to 100 kHz, which indicates that the cutoff frequency is higher than 100 kHz. [13] Therefore, the preamplifier has a linear response in the given range of frequency. The linearity of the preamplifier makes the analysis simple when QTFs which have various eigenfrequencies.

2.3 Mechanical oscillation amplitude of quartz tuning fork

When quartz tuning fork is driven electrically, it is usually treated as a resonant LRC series circuit and modeled as a mechanical oscillator. [14, 15] When QTF is driven with ac voltage V_0 at the angular frequency ω, the charge q on the QTF is described by a differential equation given by

$$L\ddot{q} + R\dot{q} + \frac{1}{C}q = V_0 e^{\imath\omega t}, \tag{2.3}$$

where the eigenfrequency ω_0 and the quality factor Q of QTF, which are defined by

$$\omega_0 = 2\pi f_0 = \frac{1}{\sqrt{LC}}, \quad Q = \frac{1}{R}\sqrt{\frac{L}{C}}, \tag{2.4}$$

respectively, and the motional capacitance C are three parameters used to describe the properties of the electrical resonator. In addition, there is a parasitic capacitance C_0 connected in parallel to the resonator (the so-called Butterworth-van Dyke circuit) when QTF is driven electrically, [14–17] thus electrically-driven QTF is represented by four parameters, f_0, Q, C and C_0.

The parasitic capacitance C_0 causes a distortion of the resonance curves, thus an additional variable capacitor has been used to reduce the effect of the parasitic capacitance. [14, 16, 18] On the other hand, C_0 can be compensated by mathematical formulas, as has been similarly done for the qPlus sensor. [17] Let A_e (A_m) be the current amplitude and θ_e (θ_m) the phase difference between with and without interaction in the Butterworth-van Dyke circuit (LRC series

circuit with the parasitic capacitance compensated). Then $A_{\rm m}$ and $\theta_{\rm m}$ are given by (see Appendix B.1 for more details)

$$A_{\rm m} = \left[A_{\rm e}^2 - 2A_{\rm e}A_{\rm c}\sin(\theta_0+\theta_{\rm e}) + A_{\rm c}^2\right]^{1/2} , \tag{2.5}$$

$$\theta_{\rm m} = \tan^{-1}\left[\frac{A_{\rm e}\sin(\theta_0+\theta_{\rm e}) - A_{\rm c}}{A_{\rm e}\cos(\theta_0+\theta_{\rm e})}\right] , \tag{2.6}$$

where $A_{\rm c} = \omega C_0 V_0$ is the current through C_0 and $\theta_0 = \tan^{-1}(C_0/QC)$ which is the phase difference between the electrical signal at free oscillation and the mechanical signal. Equations (2.5) and (2.6) may be useful to image a solid surface by using electrically-driven QTF because compensation of the parasitic capacitance during imaging is also possible with the help of one-to-one correspondence between ($A_{\rm m}$, $\theta_{\rm m}$) and ($A_{\rm e}$, $\theta_{\rm e}$).

To convert the electrical signal of QTF to the mechanical oscillation signal, it is usually assumed that the charge q is proportional to the deflection x, i.e., $q = \alpha x$ where α is called the piezoelectric coupling constant. [14, 15, 19, 20] In addition, the relationship between the driving voltage and the oscillation amplitude for QTFs has been reported previously, [21,22] and the output current $I_{\rm rms}$ is observed to be linearly proportional to the deflection x up to several micrometers. [18, 20] Introducing the piezoelectric coupling constant, Eq. (2.3) becomes

$$(L\alpha)\ddot{x} + (R\alpha)\dot{x} + \left(\frac{\alpha}{C}\right)x = V_0 e^{\imath\omega t}, \tag{2.7}$$

which has the same form of equation of motion as the simple harmonic oscillator which is given by

$$m_0\ddot{x} + b_0\dot{x} + k_0 x = F_0 e^{\imath\omega t}, \tag{2.8}$$

where m_0, b_0 and k_0 denote the effective mass, effective damping coefficient and effective stiffness of QTF, respectively, and F_0 is the effective force exerted on the QTF sensor. Here, the eigenfrequency ω_0 and quality factor Q of QTF are given by

$$\omega_0 = \sqrt{\frac{k_0}{m_0}}, \quad Q = \frac{\sqrt{m_0 k_0}}{b_0}, \tag{2.9}$$

respectively.

A simple relation $C = 2\alpha^2/k_0$ for electrically-driven QTF has been usually used with an assumption of $F_0 = \alpha V_0$ to estimate the effective stiffness k_0. [14, 15] However, the use of this assumption has not been justified nor addressed. Let the force-voltage conversion factor β be

$$\beta = \frac{F_0}{V_0} = \frac{k_0 C}{\alpha}, \tag{2.10}$$

where β has the same unit of the piezoelectric constant α. Then, if β/α is constant for ED-QTF, the effective stiffness k_0 can be obtained from the motional capacitance C and the piezoelectric coupling constant α.

Figure 2.3(a) depicts the rms mechanical oscillation amplitude x_{rms} which was directly measured by an optical microscope as a function of the driving amplitude V_0 of QTF. The oscillation amplitude is linearly proportional to the driving amplitude, and the piezoelectric coupling constant α can be obtained from the slope of Fig. 2.3(a). α can be obtained from Eq. (2.13) and the force-voltage conversion factor β can be calculated from Eq. (2.10).

With these results, if the piezoelectric coupling constant α and the I-V gain Z_{G} are known, the deflection x can be obtained from V_{out}, the output

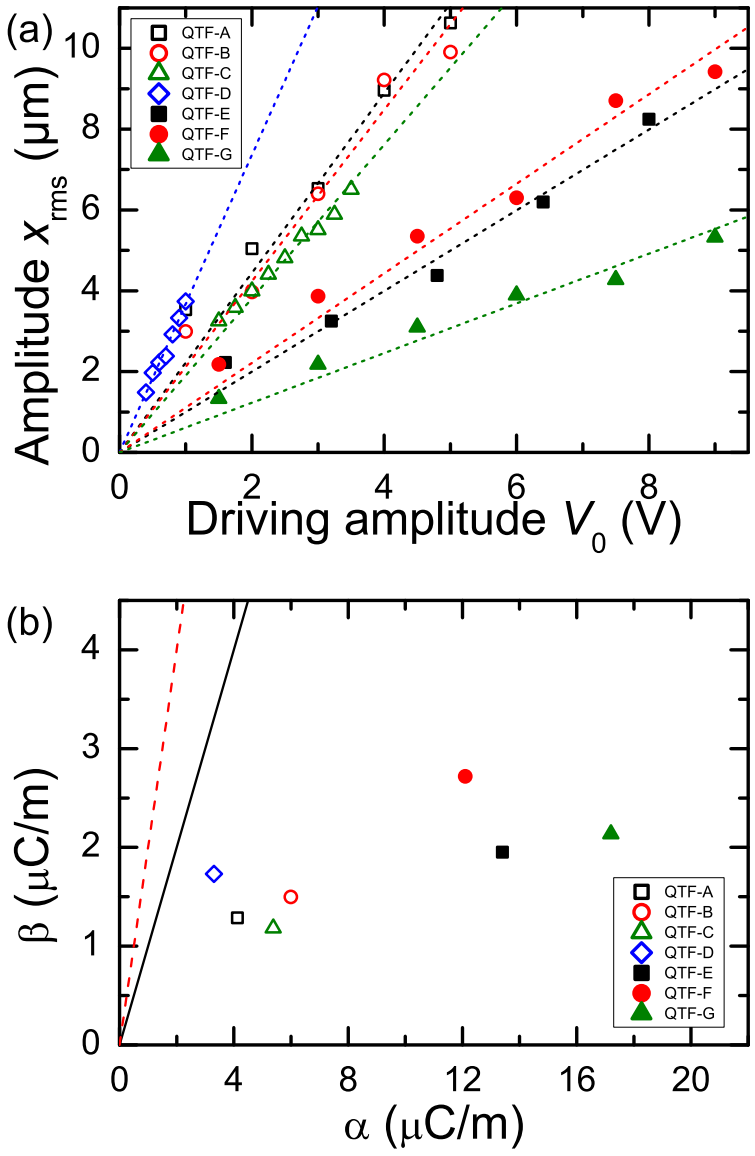

Figure 2.3: (a) The linear dependence of the root-mean-square mechanical oscillation amplitude versus the driving amplitude for several types of QTF. The piezoelectric coupling constant can be extracted from the slope of each curve by Eq. (2.13). (b) Conversion factor $\beta = k_0 C/\alpha$ versus piezoelectric coupling constant α for each QTF is depicted. The black solid and the red dashed lines represents the slope of unity and two, respectively.

voltage of QTF from the lock-in amplifier. Here $V_{\rm out}$, which is induced by the rms deflection $x_{\rm rms}$ of QTF, can be expressed by

$$V_{\rm out} = Z_{\rm G} \cdot I_{\rm rms} = Z_{\rm G}\omega\alpha x_{\rm rms}. \tag{2.11}$$

When QTF is driven at a driving voltage V_0 and frequency ω_0, $V_{\rm out}$ is also written as

$$V_{\rm out} = Z_{\rm G} \cdot \frac{V_0}{R} = Z_{\rm G} Q \omega_0 C V_0, \tag{2.12}$$

which is obtained by using the equivalent LRC series circuit model. From Eqs. (2.11) and (2.12), the relation between $x_{\rm rms}$ and V_0 is then given by

$$x_{\rm rms} = \frac{V_{\rm out}}{Z_{\rm G}\omega\alpha} = \frac{QC}{\alpha} \cdot V_0. \tag{2.13}$$

For all the QTFs tested, the value of β/α is neither 2.0 nor constant, which does not agree with the previous studies. [14, 15] It implies that the assumption $F_0 = \alpha V_0$ and therefore simple relations between the parameters in the LRC series circuit and the mechanical oscillator, such as $L = m/(2\alpha^2)$, $C = 2\alpha^2/k$, and $R = mb/(2\alpha^2)$ do not hold in general. Thus the relations cannot be introduced to estimate the effective stiffness or the piezoelectric coupling constant of electrically-driven QTF.

2.4 Response time of quartz tuning fork

The response time of a force sensor, $\tau_{\rm QTF}$, is the time constant of the transient change of signal when the interaction is exerted on the force sensor oscillating in

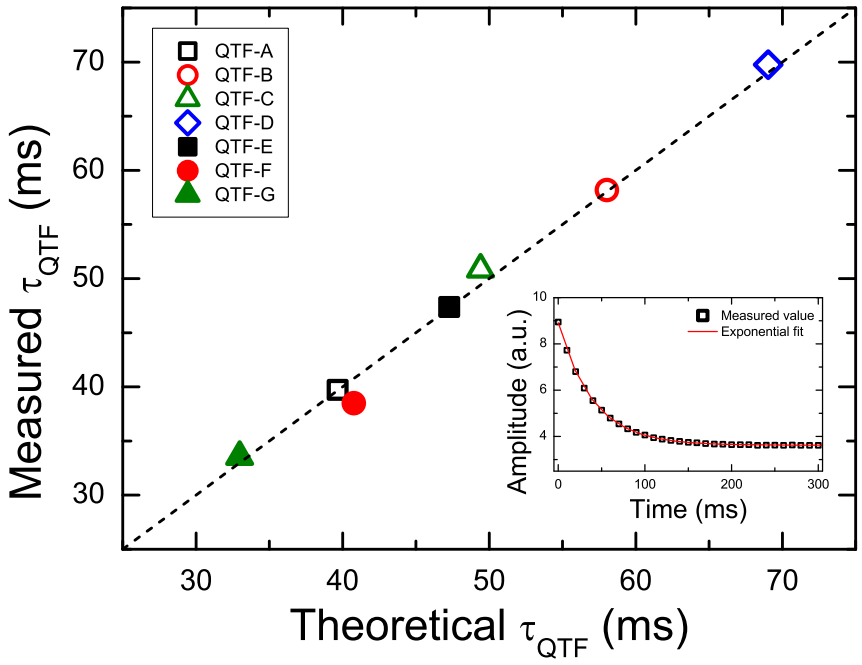

Figure 2.4: The response time of each QTF is depicted. The theoretical response time was calculated using $\tau_{\mathrm{QTF}} = 2Q/\omega_0$. The measured one was obtained from temporal changes in oscillation amplitude. The inset shows the response in amplitude after an abrupt change of QTF-A. The measured τ_{QTF} was extracted from the exponential fit (red solid line).

a steady-state. τ_{QTF} is proportional to the quality factor Q of the force sensor, which is given by [23]

$$\tau_{\mathrm{QTF}} = \frac{2Q}{\omega_0}, \tag{2.14}$$

where $\omega_0 = 2\pi f_0$. It is important for determining the time interval of movement in controlling the tip-sample distance.

Figure 2.4 presents a comparison between the measured response time of QTF and the theoretically expected one for each QTF. The temporal response of

oscillation amplitude of QTF was observed after a sudden change in the driving amplitude to determine the response time experimentally as shown in the inset of Fig. 2.4. The time constant of the exponential fit of the temporal response represents the response time of QTF. In Fig. 2.4, the measured response time of QTF has a good agreement with the theoretically expected one. In addition, the response times of every kinds of QTF are the order of tens of milliseconds because f_0 is tens of kilohertz and Q is the order of 10^3. The time interval of movement to control the tip-sample distance should be several time as much as the response time of each QTF to measure the signal in a steady state. Since the response time of QTF-C is about 50 ms, the time interval of movement is set to be longer than 500 ms in experiments.

2.5 Measurement of noise on interaction stiffness

The noise in AFM is the most crucial factor for imaging the surface and measuring the force because it determines both the minimum detectable force gradient and scanning speed. The noise on the interaction force gradient can be obtained from its standard deviation measured in time domain (see Chapter 4 for details). [24]

Figure 2.5 shows the relationship between the noise on interaction stiffness, δk_{int}, and the root-mean-square (rms) oscillation amplitude A. δk_{int} for several kinds of QTFs is inversely proportional to A, which is consistent with

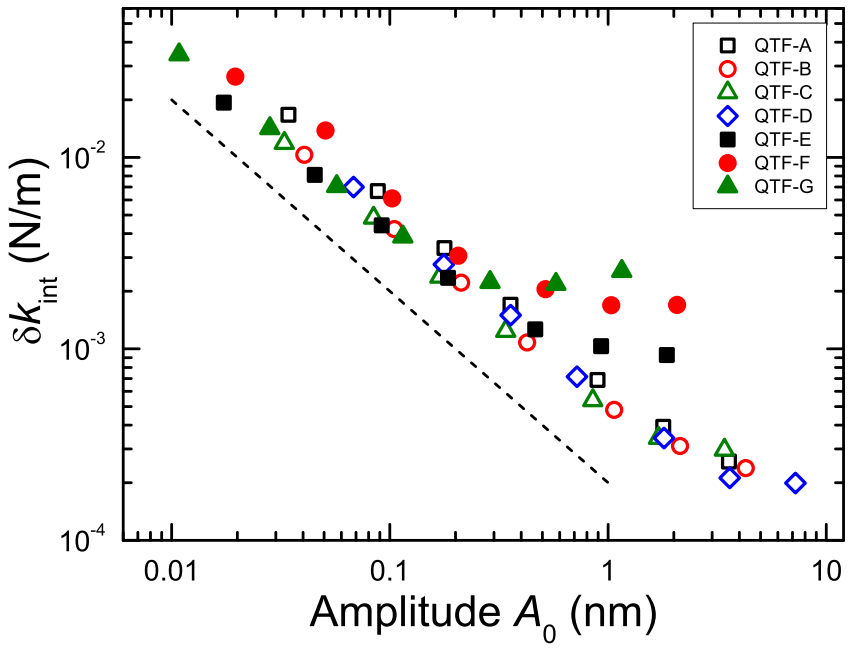

Figure 2.5: The standard deviation (SD) of the interaction stiffness, δk_{int}, as a function of the oscillation amplitude A for various kinds of quartz tuning fork is depicted. The time constant of the lock-in amplifier was 1 ms. The result indicates that δk_{int} is inversely proportional to A. The black dashed line has the slope of -1 in the plot for eye guide.

the previous result. [24] For $A = 0.1$ nm, δk_{int} is from 3.4 mN/m (QTF-E) to 5.8 mN/m (QTF-A) when the time constant of the lock-in amplifier is set to be 1 ms and the slope of low-pass filter to be 24 dB which corresponds to an equivalent noise bandwidth of 78.13 Hz. δk_{int} for all the QTFs tested are almost same because the dominant noise in ambient conditions is usually the thermal noise, which is proportional to $(k_0/Q)^{1/2}$. [13] This noise level is sufficient to measure the force gradient exerted by the nanometric water column, in the order of 0.10 N/m. [25] In addition, δk_{int} reaches a saturation for high amplitudes

especially for QTF-E, F and G. It results from the limit of the measurement resolution (0.01°) in the phase of the lock-in amplifier.

From the result, QTF-C is chosen to be introduced in AFM during experiments because QTF-C has a good noise level about 3.9 mN/m at amplitude of 0.1 nm. In addition, it is cheaper than QTF-A and B because the size with its canister is larger compared to that of QTF-A and B. QTF-E and G have higher noise level than QTF-C at larger amplitudes than $A_0 > 0.1$ nm. The oscillation amplitude should be appropriately chosen based on the results from the viewpoints of small perturbation on the nanometric water column and enough sensitivity of measurements. If the noise on force gradient is required to be reduced, Q-control may be employed putting up with lengthening the response time of the force sensor. [24, 26]

References

[1] S. Jeffery *et al.*, Phys. Rev. B **70**, 054114 (2004).

[2] T.-D. Li *et al.*, Phys. Rev. B **75**, 115415 (2007).

[3] T.-D. Li and E. Riedo, Phys. Rev. Lett. **100**, 106102 (2008).

[4] S. H. Khan, G. Matei, S. Patil, and P. M. Hoffmann, Phys. Rev. Lett. **105**, 106101 (2010).

[5] R. Szoszkiewicz and E. Riedo, Phys. Rev. Lett. **95**, 135502 (2005).

[6] K. B. Jinesh and J. W. M. Frenken, Phys. Rev. Lett. **96**, 166103 (2006).

[7] K. B. Jinesh and J. W. M. Frenken, Phys. Rev. Lett. **101**, 036101 (2008).

[8] M. Lee and W. Jhe, Phys. Rev. Lett. **97**, 036104 (2006).

[9] Y. Seo and W. Jhe, Rep. Prog. Phys. **71**, 016101 (2008).

[10] *Noncontact Atomic Force Microscopy Vol. 2*, edited by S. Morita, F. J. Giessibl, and R. Wiesendanger (Springer-Verlag, Berlin, 2009), Chap. 6.

[11] B. J. Albers *et al.*, Rev. Sci. Instrum. **79**, 033704 (2008).

[12] R. D. Grober *et al.*, Rev. Sci. Instrum. **71**, 2776 (2000).

[13] F. J. Giessibl *et al.*, Phys. Rev. B **84**, 125409 (2011).

[14] Y. Qin and R. Reifenberger, Rev. Sci. Instrum. **78**, 063704 (2007).

[15] J. Rychen *et al.*, Rev. Sci. Instrum. **71**, 1695 (2000).

[16] B. P. Ng, Y. Zhang, S. W. Kok, and Y. C. Soh, Ultramicroscopy **109**, 291 (2009).

[17] M. Lee, J. Jahng, K. Kim, and W. Jhe, Appl. Phys. Lett. **91**, 023117 (2007).

[18] R. H. M. Smit *et al.*, Rev. Sci. Instrum. **78**, 113705 (2007).

[19] F. J. Giessibl, Appl. Phys. Lett. **76**, 1470 (2000).

[20] A. Castellanos-Gomez, N. Agraït, and G. Rubio-Bollinger, Nanotechnology **20**, 215502 (2009).

[21] G. H. Simon, M. Heyde, and H.-P. Rust, Nanotechnology **18**, 255503 (2007).

[22] A. Castellanos-Gomez, C. R. Arroyo, N. Agraït, and G. Rubio-Bollinger, Microsc. Microanal. **18**, 353 (2012).

[23] T. R. Albrecht, P. Grütter, D. Horne, and D. Rugar, J. Appl. Phys. **69**, 668 (1991).

[24] J. Kim, B. Sung, B. I. Kim, and W. Jhe, J. Appl. Phys. **114**, 054302 (2013).

[25] M. Lee, B. Sung, N. Hashemi, and W. Jhe, Faraday Discuss. **141**, 415 (2009).

[26] J. Jahng *et al.*, Appl. Phys. Lett. **91**, 023103 (2007).

Chapter 3

Effective stiffness of quartz tuning fork and qPlus sensor

3.1 Introduction

Quartz tuning forks (QTFs) have been widely used in scanning probe microscopy to image the surfaces in atomic scale. [1–6] High stiffness of QTF ($> 10^3$ N/m) compared to the cantilever allows non-contact atomic force microscopy under the van der Waals forces or the capillary forces between two solid surfaces. [7] Its quality factor ($> 10^3$ in ambient conditions) offers high sensitivity enough to measure the tiny interaction forces between the tip and the material in nanoscale, while it is insensitive to the temperature variation resulting in very small temperature-induced eigenfrequency shift. [8] In addition, the piezoelectricity of quartz allows self-sensing, which enables one to measure

the forces without optical detection. [8] Because of these advantages, qPlus sensors in which one of two prongs of QTF is held fixed as well as QTFs itself with a sharp tip attached have been increasingly employed in scanning probe microscopy.

Recently, the importance of quantitative measurement of the interacting forces and consistent understanding of the interaction at the nanoscale has been gradually recognized. [9–14] In particular, the interaction force gradient and energy dissipation are expressed in terms of both the stiffness (spring constant) of force sensor and the measured quantities such as amplitude, phase or frequency shift. [11–18] Thus, it is crucial to determine the stiffness of qPlus sensor or QTF for its use as a quantitative force sensor.

For this reason, the stiffness of qPlus sensor and QTF has been recently investigated in detail. [19–21] It was observed that the stiffness of qPlus sensor is quite smaller than that calculated by the widely-used cantilever beam theory. [19] In addition, it was claimed that the effective stiffness of QTF is larger than twice the stiffness of its single prong, which is due to the coupling stiffness in the linear coupled harmonic oscillator model. [20] However, it is still questioned whether the proposed model for QTF describes properly the resonance frequency. Furthermore, any explicit formula to calculate the stiffness of qPlus sensor or QTF has not been neither derived nor experimentally verified yet. Particularly, it is also required to compare the stiffness of QTF with that of qPlus sensor to understand the model that describes QTF.

In this chapter, new formulas that allow calculation as well as quantitative

measurement of the stiffness of both QTFs and qPlus sensors are presented. By comparing the experimental results with the cantilever beam theory, it is shown that the stiffness estimated by the theory for qPlus sensor and QTF are vastly overestimated. On the other hand, the results are in good agreement with the suggested formulas for several kinds of QTF tested. In addition, it is also demonstrated that the effective stiffness of QTF is twice the stiffness of qPlus sensor which corresponds to one prong of QTF.

3.2 Theory

The cantilever beam theory has been widely used to estimate the stiffness of one prong of QTF. From the theory, the stiffness of one prong, $k_{\mathrm{length}}^{\prime\mathrm{theory}}$, is given by [20–24]

$$k_{\mathrm{length}}^{\prime\mathrm{theory}} = \frac{Ew}{4}\left(\frac{t}{l}\right)^3, \tag{3.1}$$

where E is the Young's modulus, l, t and w are the length, thickness and width of a cantilever, respectively. In addition, the resonance frequency for a rectangular cantilever, $f_0^{\prime\mathrm{theory}}$, is given by [25–27]

$$f_0^{\prime\mathrm{theory}} = \frac{1}{2\pi}\sqrt{\frac{k'}{m^*}} = 0.162\sqrt{\frac{E}{\rho}}\frac{t}{l^2}, \tag{3.2}$$

where m^* and ρ are the effective mass and the mass density of the cantilever, respectively. Eliminating l from Eq. (3.1) by using (3.2), $k_{\mathrm{freq}}^{\prime\mathrm{theory}}$ is given by

$$k_{\mathrm{freq}}^{\prime\mathrm{theory}} = 3.83(E\rho^3)^{1/4}\cdot w\cdot t^{3/2}\cdot f_0^{\prime 3/2}, \tag{3.3}$$

which is described in terms of width, thickness and resonance frequency f_0'.

3.3 Experimental Details

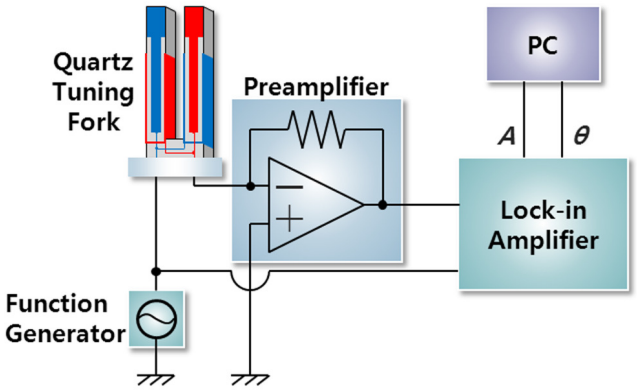

Figure 3.1: The schematic diagram for characterization of QTFs and qPlus sensors is depicted.

The schematic diagram for measurement of the stiffness of QTFs and qPlus sensors is shown in Fig. 3.1. Seven different types of QTF oscillating at various eigenfrequencies were employed (called Type A to G) to investigate the stiffness.* The tested QTF force sensors of all the types (called QTF-A to QTF-G) were used after removing their canister. In preparing the qPlus sensors of all the types (called qPlus-A to qPlus-G), one prong of another QTF of each type was firmly fixed on an L-shape ceramic massive substrate by using a rigid epoxy resin (Torr Seal, Varian) and the other prong was made freely oscillate without a tip. The quartz resonators were actuated by a function generator

*All the types of QTF were purchased from Epson-Toyocom Corporation: Type A (C-005R), B (C-004R) and C (C-002RX) have nominal resonance frequency of 32.768 kHz, and Type D, E, F and G are C-2 type and have nominal resonance frequencies of 20.000, 65.536, 76.800 and 100.000 kHz, respectively.

by applying voltage between two electrodes via the piezoelectric properties of quartz. The preamplifier was composed of an operational amplifier (LF357N, National Semiconductor) and a resistor with nominal resistance of 10 MΩ. The amplitude and phase difference of output voltage of the preamplifier were measured by a lock-in amplifier (SR830, Stanford Research Systems) and recorded by a computer. The experiments were carried out in ambient conditions.

3.4 Results and Discussion

3.4.1 Effective stiffness of quartz tuning fork

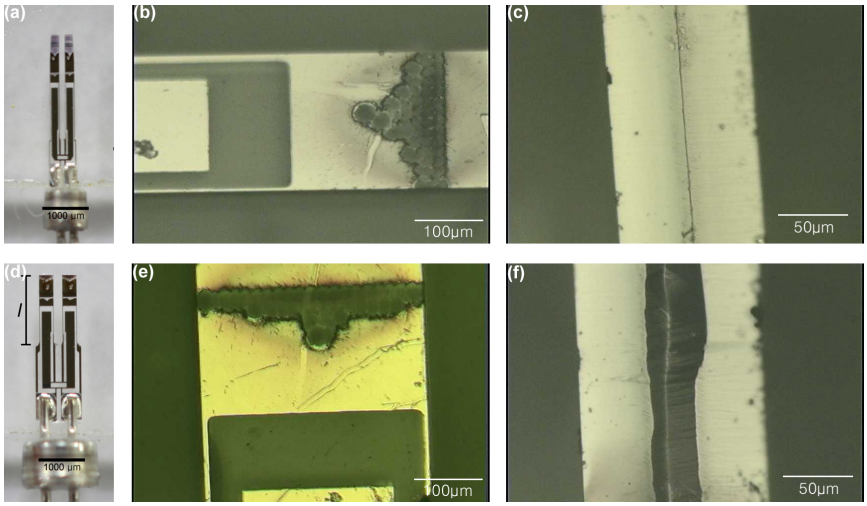

Figure 3.2: Photographs of QTF-A (a)-(c) and QTF-G (d)-(e) are depicted. Parts (a) and (d) show an overall shape and length by using the camera; parts (b) and (e) show the thickness and parts (c) and (f) show the width by using an optical microscope. The definition of the apparent length l of a prong is depicted in (d).

Representative photographs of QTF-A and QTF-G are shown in Fig. 3.2. The overall shape of each QTF was taken as shown in Figs. 3.2(a) and 3.2(d) by a high-resolution digital camera (Canon EOS 5D Mark II equipped with Canon EF 100 mm f/2.8L macro lens) and the length l was determined therefrom.[†] The thickness t and width w were determined by an optical microscope as depicted in Figs. 3.2(b), 3.2(c), 3.2(e) and 3.2(f).[‡] For l, t and w, allowable maximum and minimum distances of a prong of each QTF were chosen in the photograph and the average of the two are taken. Each error in l, t and w was obtained by dividing the difference between the maximum and the minimum by two. The theoretical resonance frequency of a prong of QTFs, $f_0'^{\mathrm{theory}}$, was obtained from Eq. (3.2) and the measured dimensions. In addition, the calculated stiffness of a prong of QTFs, $k_{\mathrm{length}}'^{\mathrm{theory}}$, was obtained by Eq. (3.1) The maximum and minimum values of $f_0'^{\mathrm{theory}}$ and $k_{\mathrm{length}}'^{\mathrm{theory}}$ were obtained with considering the errors in l, t and w, and the errors in $f_0'^{\mathrm{theory}}$ and $k_{\mathrm{length}}'^{\mathrm{theory}}$ come from their maximum value of error, regardless of whether it is a positive or negative one. The elastic modulus $E = 78.7$ GPa and the density $\rho = 2650$ kg/m^3 for quartz [28] were used to calculate $f_0'^{\mathrm{theory}}$ and $k_{\mathrm{length}}'^{\mathrm{theory}}$. The dimensions l, t and w and the calculated values of the resonance frequency $f_0'^{\mathrm{theory}}$ and stiffness $k_{\mathrm{length}}'^{\mathrm{theory}}$ are summarized in Table 3.1.

Figures 3.3 and 3.4 shows the result for QTFs which have two prongs free to oscillate. When a quartz resonator is driven electrically, it can be described

[†]The measured resolution of this equipment is 6.7 μm/pixel

[‡]A pixel in measuring width and thickness corresponds to 0.72 μm and 0.36 μm, respectively.

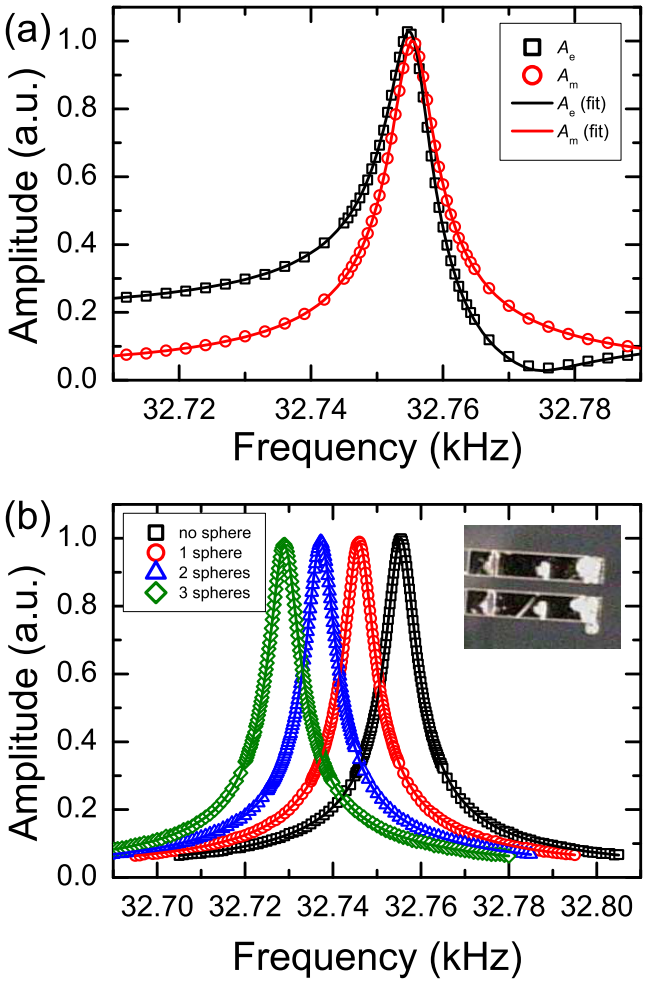

Figure 3.3: (a) Resonance curves of QTF-A are depicted. Squares (black color) represent the amplitude of the current flowing through the QTF ($A_{\rm e}$) and circles (red color) indicate the amplitude without the effect of parasitic capacitance ($A_{\rm m}$). Solid lines represent their Lorentzian fit. The offset of two curves comes from its parasitic capacitance (see text). (b) Resonance curves of QTF-A with respect to the attached mass are depicted. The resonance frequency decreases as the number of spheres attached onto a prong of QTF increases. The inset of (b) shows the 40 μm sphere attached onto the end of a prong.

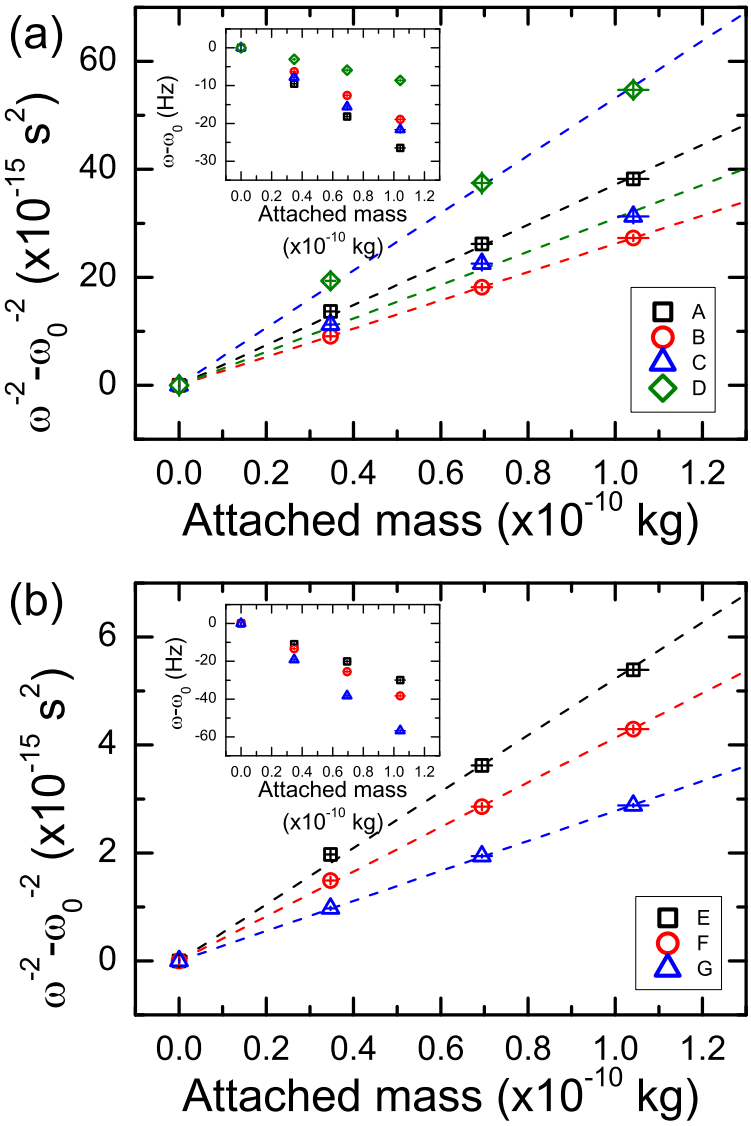

Figure 3.4: Attached mass and its corresponding shift of resonance frequency for QTF-A, B, C and D are depicted in (a) and for QTF-E, F and G in (b). The insets of (a) and (b) show the linear frequency shift.

Type	l	t	w	$f_0'^{\text{theory}}$	$k_{\text{length}}'^{\text{theory}}$
A	2239 (15)	199 (1)	104 (1)	35060 (653)	1439 (66)
B	2415 (24)	259 (1)	103 (1)	39163 (1099)	2481 (161)
C	2302 (15)	240 (2)	103 (1)	39990 (1033)	2305 (159)
D	2980 (19)	240 (3)	132 (2)	23869 (710)	1364 (119)
E	1835 (23)	336 (4)	133 (2)	88106 (3327)	16038 (1481)
F	1692 (17)	333 (4)	135 (2)	102583 (3036)	20178 (1505)
G	1451 (21)	135 (3)	132 (2)	138870 (5833)	30894 (3071)

Table 3.1: The measured dimensions, length l, thickness t, and width w, of a prong of QTFs are represented in μm. The theoretical resonance frequencies of a prong of QTFs, $f_0'^{\text{theory}}$, are in Hz. Their calculated values of stiffness $k_{\text{length}}'^{\text{theory}}$ by Eq. (3.1) are in N/m. Each value in parenthesis denotes its error with the same unit as the value in front of the parenthesis (see text).

as the Butterworth-van Dyke equivalent circuit (see Fig. 2(a) in Ref. [16]). [16, 29, 30] The parasitic capacitance C_0 which is connected in parallel to RLC series circuit distorts the resonance curve. The effect of C_0 on the resonance curve is eliminated by the formula given by [16]

$$A_{\text{m}} = \sqrt{A_{\text{e}}^2 - 2A_{\text{e}}A_{\text{c}}\sin\theta_{\text{e}} + A_{\text{c}}^2} \tag{3.4}$$

where A_{e} (θ_{e}) and A_{m} represent the amplitude (phase) of the current flowing through quartz resonator with and without the effect of the parasitic capacitance, respectively, and $A_{\text{c}} = 2\pi f C_0 V_0$ is the current flowing through the parasitic capacitance when V_0 is the driving amplitude. The resonance curves are depicted in Fig. 3.3(a), A_{e} is the measured amplitude of current flowing out of the QTF via frequency sweeping, and A_{m} is the amplitude in which the effect of the parasitic capacitance is compensated by using Eq. (3.4). The Lorentzian fit

of A_{m} agrees well with the compensated result, which indicates that Eq. (3.4) is effective to compensate the parasitic capacitance of QTF even though there is no additional compensation circuit. [25, 31]

Figure 3.3(b) represents the shift of resonance curve of the QTF when the mass is attached onto the end of prong. Microspheres (polystyrene with density of 1.05 g/cm^3) were attached onto the end of its top face for the mass by tiny capillary force without using glue as shown in the inset of Fig. 3.3(b). For all the QTFs tested, microspheres with diameter of 40 μm (4240A, Thermo Scientific, real diameter of 39.82 ± 0.44 μm were employed for the mass. It was found that the resonance frequency gets smaller as a heavier mass is attached onto the prong. It is important to note that the quality factor Q was almost unchanged whereas the mass imbalance of two prongs may cause decrease in Q. This implies that the mass attached onto a prong is much lighter than that of a prong of QTF, [32] and correspondingly the mass attachment has little effect on the antiparallel oscillation of two prongs. [31]

The frequency shifts $\omega^{-2} - \omega_0^{-2}$ (ω and ω_0 are the angular resonance frequency of QTF with and without attached mass, respectively) as a function of attached mass for QTF-A, B, C and D are depicted in Fig. 3.4(a), and those for QTF-E, F and G are in Fig. 3.4(b). It was found that the results for QTFs are also consistent with the equation given by [20, 21, 33]

$$\frac{1}{\omega^2} = \frac{m}{k} + \frac{1}{k}(\Delta m) = \frac{1}{\omega_0^2} + \frac{1}{k}(\Delta m) \ , \tag{3.5}$$

where k and m represent the effective stiffness and effective mass of QTF, re-

spectively. Here the unprimed variables such as k and m denote those values of QTF. In Figs. 3.4(a) and 3.4(b), the x-axis error bars come from the uncertainty in diameter of microspheres. The y-axis error bars represent the minimum and maximum values in measuring the resonance frequency obtained from the fit in Fig. 3.3(b). As shown in Figs. 3.4(a) and 3.4(b), the experimental results are in very good agreement with Eq. (3.5). The linear fits in Figs. 3.4(a) and 3.4(b) are based on Eq. (3.5). The slope of each linear fit represents an inverse of the stiffness of the QTF, k^{exp}. Further discussion will be added in the last subsection after dealing with the results of qPlus sensors.

3.4.2 Stiffness of qPlus sensor

Figure 3.5(a) shows the resonance curves of qPlus-A which is driven electrically. For qPlus sensors, it is found that the offset of the two curves of A_{e} and A_{m} is significantly larger than that of QTFs because A_{m} is quite smaller than A_{c} for qPlus sensors due to their reduced quality factor whereas A_{m} is larger than A_{c} for QTFs. Figure 3.5(b) shows the shift of resonance curves resulting from the mass attached onto the end of qPlus-A to measure the stiffness of the sensor. As shown in Fig. 3.5(b), the resonance frequency decreases as the spheres attach onto the qPlus sensor, which is consistent with the previous result. [21]

Figure 3.6(a) shows the shift of resonance frequency represented by $\omega'^{-2} - \omega_0'^{-2}$ (ω' and ω_0' are the angular resonance frequency of qPlus sensor with and without attached mass, respectively) as a function of the attached mass for qPlus-A, B, C and D when aforementioned microspheres with diameter of 40

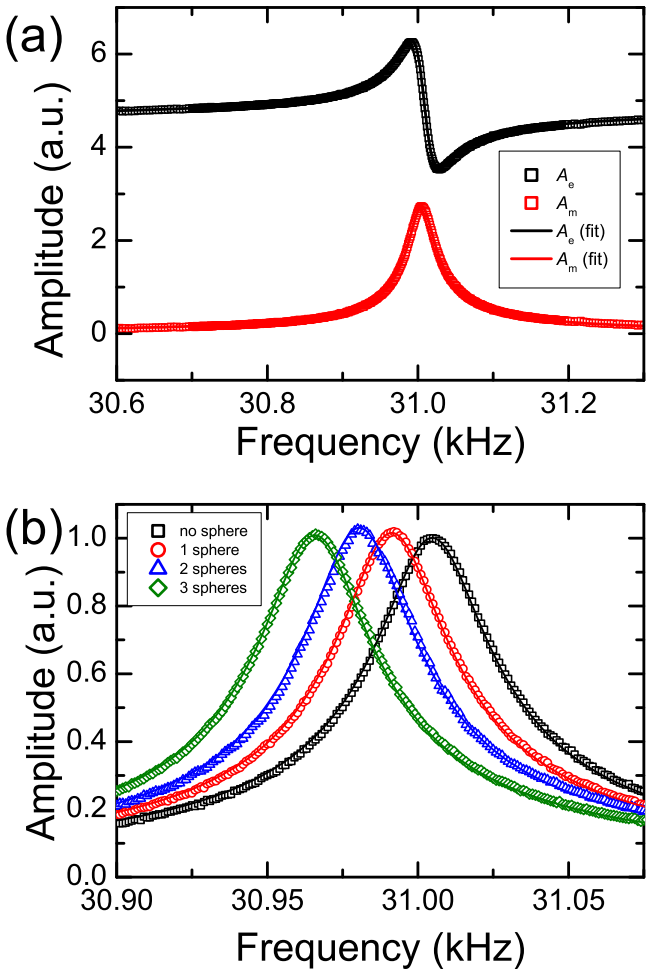

Figure 3.5: (a) Resonance curves of qPlus-A are depicted. Squares (black color) denote the amplitude of the current flowing through the qPlus sensor (A_{e}) and circles (red color) denote the amplitude without the effect of parasitic capacitance (A_{m}). Solid lines represent their Lorentzian fit. The offset of two curves comes from its parasitic capacitance (see text). (b) Resonance curves of qPlus-A with respect to the attached mass are depicted. The resonance frequency decreases as the number of spheres attached onto a prong increases.

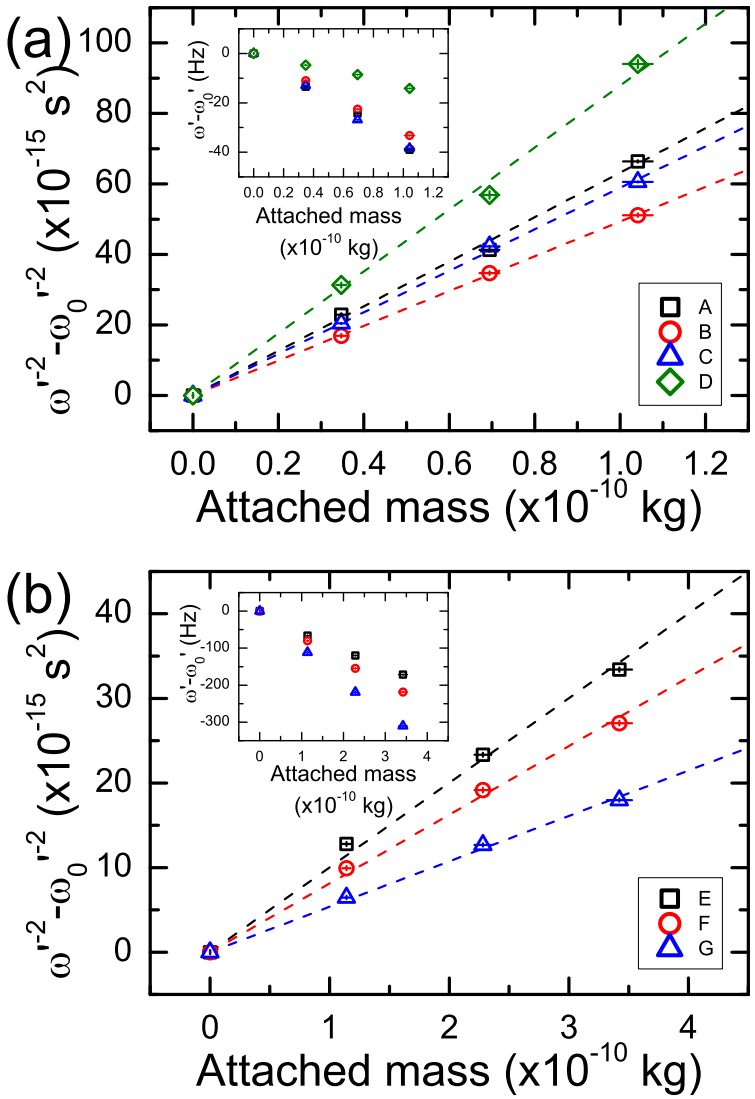

Figure 3.6: Attached mass and its corresponding shift of resonance frequency for qPlus-A, B, C and D are depicted in (c) and for qPlus-E, F and G in (d). The insets of (c) and (d) show the linear frequency shift.

μm (4240A, Thermo Scientific) were employed. In Fig. 3.6(b) also depicts the shift for qPlus-E, F and G which have high stiffness when microspheres with diameter of 60 μm (4260A, Thermo Scientific, real diameter of 59.20 ± 0.60 μm) was introduced to observe the shift more clearly. It is worth noting that the mass of a sphere of 4240A and 4260A are 34 ng and 114 ng, respectively, which is very small compared to the effective mass of one prong (40 to 75 μg for qPlus sensors used here). The relation between the shift of resonance frequency and the attached mass is given by

$$\frac{1}{\omega'^2} = \frac{m'}{k'} + \frac{1}{k'}(\Delta m) = \frac{1}{\omega_0'^2} + \frac{1}{k'}(\Delta m) \ , \tag{3.6}$$

where k' denotes the stiffness of qPlus sensor and m' and Δm represent the effective mass of qPlus sensor and the attached mass, respectively. Here the primed variables such as k' and m' represent those values of qPlus sensor. The error bars in Figs. 3.6(a) and 3.6(b) are marked in the same manner as Fig. 3.4. The linear fits in Figs. 3.6(a) and 3.6(b) are based on Eq. (3.6). As shown in Figs. 3.6(a) and 3.6(b), the experimental results are in very good agreement with Eq. (3.6). The slope of each linear fit represents an inverse of the stiffness of the qPlus sensor.

3.4.3 Discussion

Tables 3.2 and 3.3 summarize the experimentally determined and theoretically expected resonance frequency and stiffness, respectively. The error in the measured resonance frequency of each QTF $f_0^{\rm exp}$ and that of each qPlus sensor

$f_0'^{\text{exp}}$ represents the standard error. It has been found that the measured resonance frequency of qPlus sensors is smaller than that of same kinds of QTF, which is consistent with previous experiments. [16, 28, 34] It has been observed that $f_0'^{\text{exp}}$ is smaller than $f_0'^{\text{theory}}$ for all qPlus sensors tested, as shown in Table 3.2. Interestingly, f_0^{exp} is also smaller than $f_0'^{\text{theory}}$ for every QTF, and the difference between them is up to 39% for QTF-G. This relationship was also found in another experimental study which employs a different kind of QTF ($f_0^{\text{exp}} = 32.566$ kHz and $f_0'^{\text{theory}} = 34.39$ kHz). [25]

Type	f_0^{exp}	$f_0'^{\text{exp}}$	$f_0'^{\text{theory}}$
A	32755.4 (0.34)	31005 (0.11)	35060 (653)
B	32756.6 (0.24)	32060 (0.18)	39163 (1099)
C	32754.0 (0.44)	31817 (0.04)	39990 (1033)
D	19991.0 (0.16)	19714 (0.06)	23869 (710)
E	65540.0 (0.31)	63940 (0.65)	88106 (3327)
F	76782.0 (0.33)	74340 (0.90)	102583 (3036)
G	99994.0 (0.31)	95786 (1.75)	138870 (5833)

Table 3.2: The experimental resonance frequency of QTFs, f_0^{exp}, and the experimental and theoretical resonance frequencies of qPlus sensors, $f_0'^{\text{exp}}$ and $f_0'^{\text{theory}}$, are represented in Hz. Each value in parenthesis denotes the error with the same unit as the value in front of the parenthesis (see text).

The measured stiffness of QTF k^{exp} and that of qPlus sensor k'^{exp} were determined from the slope of Figs. 3.4 and 3.6, respectively. The calculated stiffness of a prong, $k_{\text{freq}}'^{\text{theory}}$ was obtained from Eq. (3.3). The error in k^{exp} and k'^{exp} in Table 3.3 represents the standard error whereas the error in $k_{\text{freq}}'^{\text{theory}}$ is obtained with considering the errors in t, w and $f_0'^{\text{exp}}$ similar to the method for

the error in $k_{\mathrm{length}}^{\prime\mathrm{theory}}$.

Type	k^{exp}	$k^{\prime\mathrm{exp}}$	$k_{\mathrm{length}}^{\prime\mathrm{theory}}$	$k_{\mathrm{freq}}^{\prime\mathrm{theory}}$
A	2692(31)	1582(26)	1439(66)	1196(21)
B	3817(1)	2027(10)	2481(161)	1836(39)
C	3234(71)	1697(20)	2305(159)	1634(47)
D	1880(20)	1137(29)	1362(119)	1022(41)
E	19135(272)	9992(235)	16038(1481)	9905(329)
F	24191(153)	12313(248)	20178(1505)	12435(356)
G	36011(118)	18627(319)	30894(3073)	17679(594)

Table 3.3: The measured stiffness of QTFs, k^{exp}, that of qPlus sensors, $k^{\prime\mathrm{exp}}$, and calculate values of stiffness, $k_{\mathrm{length}}^{\prime\mathrm{theory}}$ and $k_{\mathrm{freq}}^{\prime\mathrm{theory}}$ are depicted in N/m. Each value in parenthesis denotes the error with the same unit as the value in front of the parenthesis (see text).

For comparison, $k_{\mathrm{length}}^{\prime\mathrm{theory}}$ and $k_{\mathrm{freq}}^{\prime\mathrm{theory}}$ with respect to $k^{\prime\mathrm{exp}}$ are depicted in Fig. 3.7. The x-axis error bars represent the error in measuring $k^{\prime\mathrm{exp}}$ and the y-axis error bars indicate the maximum and minimum of $k^{\prime\mathrm{theory}}$. Interestingly, it has been observed that $k_{\mathrm{length}}^{\prime\mathrm{theory}}$ is not in good agreement with $k^{\prime\mathrm{exp}}$ and it is overestimated. This behavior is remarkable for qPlus sensors which have high resonance frequency (qPlus-E, F and G). In particular, $k_{\mathrm{length}}^{\prime\mathrm{theory}}$ is overestimated up to 66% with respect to $k^{\prime\mathrm{exp}}$ for qPlus-G. On the other hand, the discrepancy between $k_{\mathrm{freq}}^{\prime\mathrm{theory}}$ and $k^{\prime\mathrm{exp}}$ is as small as 5% for qPlus-G, which indicates $k_{\mathrm{freq}}^{\prime\mathrm{theory}}$ is consistent with $k^{\prime\mathrm{exp}}$. Moreover, the intrinsic error in $k_{\mathrm{freq}}^{\prime\mathrm{theory}}$ is small compared to $k_{\mathrm{freq}}^{\prime\mathrm{theory}}$ because the resonance frequency can be determined within the error of 10^{-5} of the resonance frequency. Therefore, it has been found that Eq. (3.3) well describes the stiffness of qPlus sensor and correspondingly the stiffness can

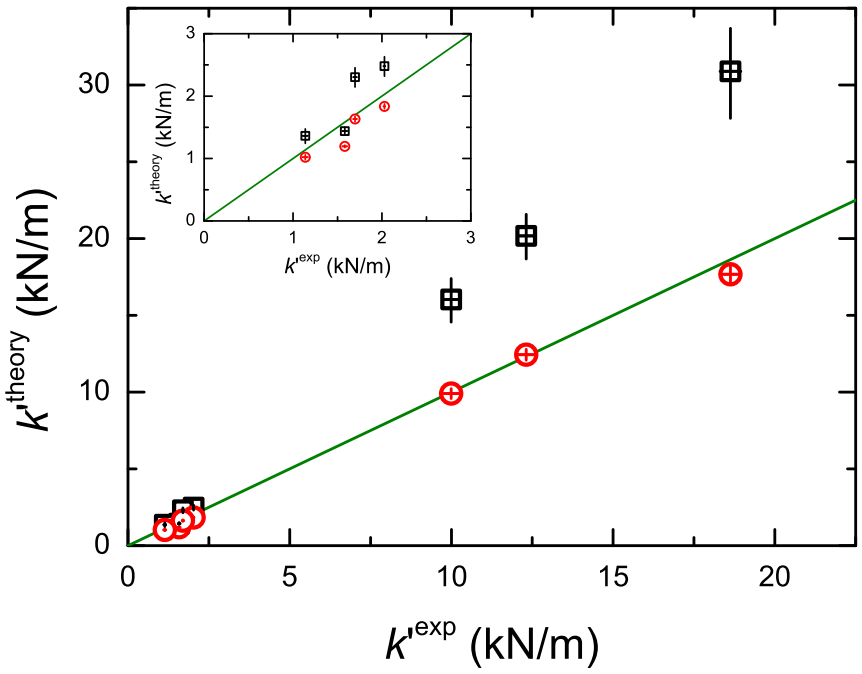

Figure 3.7: The experimental and theoretical results for stiffness of qPlus sensors are depicted. k'^{exp} is experimentally determined for seven kinds of qPlus sensor [see Fig. 3.6]. $k'^{\mathrm{theory}}_{\mathrm{length}}$ (black squares) and $k'^{\mathrm{theory}}_{\mathrm{freq}}$ (red circles) are determined from Eqs. (3.1) and (3.3), respectively. The green solid line of slope unity indicates the result expected if the values of the theory coincides with that of the experimentally determined k'^{exp}. The inset shows the same but magnified plot for the result for qPlus sensors of small stiffness.

be estimated more accurately when the resonance frequency of qPlus sensor is considered.

It has been also shown that the measured stiffness and resonance frequency are respectively smaller than the expected ones using cantilever beam theory by Eqs. (3.1) and (3.2) in qPlus sensors. When a qPlus sensor is considered as a cantilever, these results indicate the length of the cantilever is longer

than the apparent length of the qPlus sensor. It is because the prong of qPlus sensor is not ideally rigid supported, according to finite element method. [19] It has been suggested that the length of oscillating cantilever can be estimated using Eq. (3.2) by substituting the resonance frequency with the measured one, and it has been shown that this estimation of length works well in calculation of the stiffness of qPlus sensor, and that Eq. (3.3) well describes the stiffness of qPlus sensor.

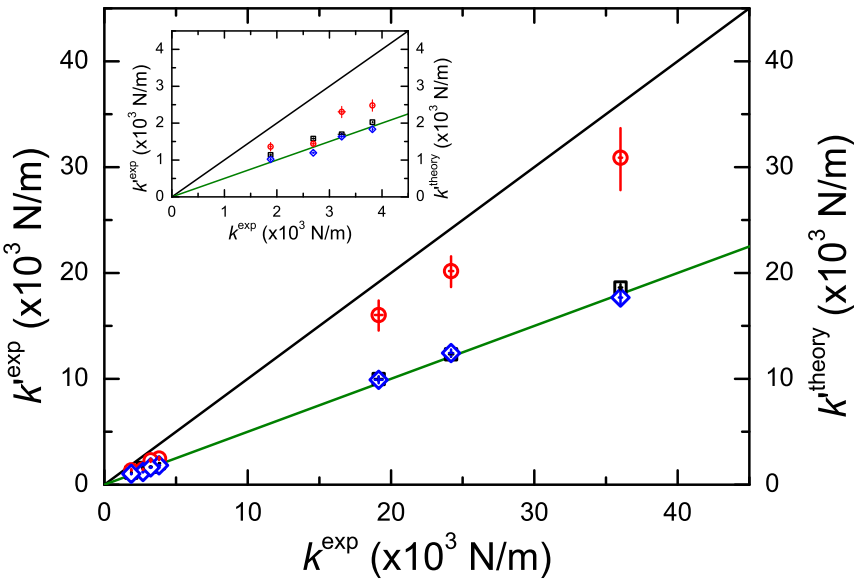

Figure 3.8: The experimental and theoretical results for stiffness of QTFs are depicted. k^{exp} is experimentally determined for seven kinds of QTF [see Fig. 3.4]. Squares (black), circles (red) and diamonds (blue) represents the measured stiffness of qPlus sensors, k'^{exp}, and two calculated values of stiffness of qPlus sensors, $k'^{\mathrm{theory}}_{\mathrm{length}}$ and $k'^{\mathrm{theory}}_{\mathrm{freq}}$, respectively. The black and green solid lines have slopes of unity and an half, respectively. The inset shows the same but magnified plot for the result for QTFs of small stiffness.

Figure 3.8 shows the values of stiffness obtained from qPlus sensors, k'^{exp}, $k'^{\mathrm{theory}}_{\mathrm{length}}$ and $k'^{\mathrm{theory}}_{\mathrm{freq}}$ with respect to k^{exp}. The error bars in Fig. 3.8 are also represented as the same way in Fig. 3.7. It has been found that the calculated stiffness of QTFs estimated by Eq. (3.1) based on the cantilever beam theory, $2k'^{\mathrm{theory}}_{\mathrm{length}}$, is seriously overestimated with respect to k^{exp} (up to 72% for QTF-G) as shown in Fig. 3.8. Furthermore, it has been observed that the value of k^{exp} is twice that of k'^{exp} or $k'^{\mathrm{theory}}_{\mathrm{freq}}$, which is consistent with the recently proposed model by Giessibl *et al.* [26] However, the significant coupling between two prongs in the coupled oscillator model of the previous study [20] is not observed in this investigation.

Thus, the effective stiffness of QTF is expressed by

$$k^{\mathrm{theory}}_{\mathrm{freq}} \approx 2 \cdot 3.83 (E\rho^3)^{1/4} \cdot w \cdot t^{3/2} \cdot f_0^{3/2} \,, \tag{3.7}$$

where E and ρ are the Young's modulus and density of quartz, respectively, w and t are the width and thickness of one prong of QTF, respectively, and f_0 is the resonance frequency of QTF. To hold Eq. (3.7), two prongs of QTF should oscillate antiparallel and symmetric each other. It is known that mass imbalance of two prongs of QTF results in decrease of Q. [35] Since a tip is usually attached onto single prong of QTF, a small mass was attached onto one prong of QTFs and it was observed the corresponding shift of resonance frequency. Additionally, the quality factor Q was monitored to study the effect of this mass imbalance on the symmetric oscillation as the mass increases. It could not be found large decrease in the quality factor Q (within 3% for QTF-

A, B, C and D, and within 12% for QTF-E, F and G) as shown in Fig. 3.3(b) whereas qPlus sensors show a big drop in quality factor compared with that of QTFs, i.e., quality factors of qPlus-A, B, C and D are as small as 1/3-1/6 of those of same kinds of QTF, and those of qPlus-E, F and G are 1/23-1/67 of QTF-E, F and G [see Figs. 3.3(a) and 3.5(a)]. The small change in quality factor during mass attachment implies that the antiparallel and symmetric oscillation does not change significantly.

The discrepancy between $k'^{\mathrm{theory}}_{\mathrm{length}}$ and k'^{exp} in Fig. 3.7 and between $k'^{\mathrm{theory}}_{\mathrm{length}}$ and $k^{\mathrm{exp}}/2$ in Fig. 3.8 becomes wider with increasing stiffness and resonance frequency of the force sensor. The tendency comes from the difference of the cantilever length (i.e., the oscillating length from the viewpoint of cantilever) and the apparent length. For all the types of QTF tested, it has been found that the cantilever length is longer than the apparent length. Furthermore, the length difference is from 226 μm (QTF-B) to 276 μm (QTF-D) except QTF-A (77 μm), which is interestingly not so scattered. Since the $k'^{\mathrm{theory}}_{\mathrm{length}}$ is inversely proportional to the cube of the length, the discrepancy increases as the apparent length decreases due to the large portion of the length difference.

According to the linear coupled oscillator model, [20] the coupling stiffness k_{c} can be obtained from the ratio of angular resonance frequencies of QTF ω and qPlus sensor ω' in this study given by

$$\frac{k_{\mathrm{c}}}{k'} = \frac{1}{2}\left[\left(\frac{\omega}{\omega'}\right)^2 - 1\right] \ . \tag{3.8}$$

From Eq. (3.8), the ratio k_{c}/k' are about 1-6% for QTFs, which is very small

compared to that of the previous study. [20] In addition, applying Eq. (3.2) to their study, it was obtained that $f_0'^{\text{theory}} = 20.260$ kHz for TF-A and it is 33.195 kHz for TF-B. It was found that the values of $f_0'^{\text{theory}}$ for TF-A and TF-B have a very small error (1.3%) of their resonance frequencies (for antiparallel oscillation), f_0 (20.000 and 32.766 kHz, respectively), rather far from the parallel (or in-phase) oscillation frequencies (18.255 and 27.800 kHz). It indicates that the resonance frequencies of a prong of TF-A and TF-B are almost equal to those of QTFs, f_0, which is not consistent with their large coupling stiffness. Therefore, not only the stiffness but also the resonance frequency should be considered to describe the quartz tuning forks more precisely.

3.5 Conclusions

In this work, the stiffness of qPlus sensor and QTF has been investigated. It has been found that the stiffness and resonance frequency estimated by the cantilever beam theory are larger than the measured ones, which indicates the length of cantilever is underestimated. It has been proposed a formula to calculate the effective stiffness of qPlus sensor or QTF in terms of the resonance frequency instead of the length, based on the cantilever beam theory. Then, it has been demonstrated that the formula describes the measured effective stiffness well. From the results, it has been also shown that the effective stiffness of QTF is twice that of qPlus sensor, which is consistent with the recently proposed model. This work provides consistent and reliable use of qPlus sensor and QTF

for quantitative force measurement in atomic force microscopy or spectroscopy.

References

[1] F. J. Giessibl, Science **267**, 68 (1995).

[2] F. J. Giessibl, S. Hembacher, H. Bielefeldt, and J. Mannhart, Science **289**, 422 (2000).

[3] L. Gross *et al.*, Science **324**, 1428 (2009).

[4] J. Welker and F. J. Giessibl, Science **336**, 444 (2012).

[5] T. Ihn *et al.*, Physica E **13**, 671 (2002).

[6] L. Lichtenstein, M. Heyde, and H.-J. Freund, Phys. Rev. Lett. **109**, 106101 (2012).

[7] Y. Seo and W. Jhe, Rep. Prog. Phys. **71**, 016101 (2008).

[8] *Noncontact Atomic Force Microscopy Vol. 2*, edited by S. Morita, F. J. Giessibl, and R. Wiesendanger (Springer-Verlag, Berlin, 2009), Chap. 6.

[9] H. Choe *et al.*, Phys. Rev. Lett. **95**, 187801 (2005).

[10] T.-D. Li and E. Riedo, Phys. Rev. Lett. **100**, 106102 (2008).

[11] R. Garcia *et al.*, Phys. Rev. Lett. **97**, 016103 (2006).

[12] S. H. Khan, G. Matei, S. Patil, and P. M. Hoffmann, Phys. Rev. Lett. **105**, 106101 (2010).

[13] M. Lee, B. Sung, N. Hashemi, and W. Jhe, Faraday Discuss. **141**, 415 (2009).

[14] S. An *et al.*, Appl. Phys. Lett. **101**, 053114 (2012).

[15] M. Lee and W. Jhe, Phys. Rev. Lett. **97**, 036104 (2006).

[16] M. Lee, J. Jahng, K. Kim, and W. Jhe, Appl. Phys. Lett. **91**, 023117 (2007).

[17] S. Jeffery *et al.*, Phys. Rev. B **70**, 054114 (2004).

[18] J. Kim, B. Sung, B. I. Kim, and W. Jhe, J. Appl. Phys. **114**, 054302 (2013).

[19] G. H. Simon, M. Heyde, and H.-P. Rust, Nanotechnology **18**, 255503 (2007).

[20] A. Castellanos-Gomez, N. Agraït, and G. Rubio-Bollinger, Nanotechnology **20**, 215502 (2009).

[21] J. Berger *et al.*, Beilstein J. Nanotechnol. **4**, 1 (2013).

[22] K. Karrai and R. D. Grober, Appl. Phys. Lett. **66**, 1842 (1995).

[23] W. H. J. Renson, N. F. van Hulst, A. G. T. Ruiter, and P. E. West, Appl. Phys. Lett. **75**, 1640 (1999).

[24] R. D. Grober *et al.*, Rev. Sci. Instrum. **71**, 2776 (2000).

[25] Y. Qin and R. Reifenberger, Rev. Sci. Instrum. **78**, 063704 (2007).

[26] F. J. Giessibl *et al.*, Phys. Rev. B **84**, 125409 (2011).

[27] C. J. Chen, *Introduction to Scanning Tunneling Microscopy* (Oxford University Press, New York, 1993).

[28] F. J. Giessibl, Appl. Phys. Lett. **73**, 3956 (1998).

[29] J. Rychen *et al.*, Rev. Sci. Instrum. **71**, 1695 (2000).

[30] J. Zelenka, *Piezoelectric Resonators and their Applications* (North Holland, Amsterdam, 1986).

[31] B. P. Ng, Y. Zhang, S. W. Kok, and Y. C. Soh, Ultramicroscopy **109**, 291 (2009).

[32] A. Castellanos-Gomez, N. Agraït, and G. Rubio-Bollinger, Nanotechnology **21**, 145702 (2010).

[33] J. P. Cleveland, S. Manne, D. Bocek, and P. K. Hansma, Rev. Sci. Instrum. **64**, 403 (1993).

[34] F. J. Giessibl, Appl. Phys. Lett. **76**, 1470 (2000).

[35] A. Castellanos-Gomez, N. Agraït, and G. Rubio-Bollinger, Ultramicroscopy **111**, 186 (2011).

Chapter 4

Optimization of force sensitivity in Q-controlled amplitude-modulation atomic force microscopy*

4.1 Introduction

Since its invention, atomic force microscope (AFM), [2] has been used in such diverse research fields as physics, chemistry, biology and engineering. In particular, it has been introduced to study subatomic features of individual adatoms [3] or to measure the charge state of an adatom, [4] which requires high measure-

*This chapter was rewritten on the basis of the work published in J. Appl. Phys. 114, 054302 (2013) [1]

ment sensitivity characterized by the minimum detectable force gradient. [5] In addition, for biological samples, increase of the scan speed of AFM is important for studying the dynamic behavior of biomolecules. [6–8] However, the signal can only be obtained at a limited accuracy and for a finite acquisition time due to the presence of noise. Therefore, the measurement noise is a critical factor that determines both the minimum detectable force gradient and the scan speed in AFM.

To determine the noise in AFM, the thermal noise spectra of oscillation amplitude has been usually measured in both amplitude modulation (AM)-AFM and frequency modulation (FM)-AFM. Recently, it was pointed out that the evolution of phase fluctuation to frequency fluctuation is important in FM-AFM. [9] However, little attention has been paid on the phase fluctuation or the fluctuation of force-gradient measurement in AM-AFM.

Q-control technique has been employed to increase Q for enhancement of force sensitivity at low-Q environment (e.g., in liquid). In contrast, shorter relaxation time is required for faster imaging of the solid surface in AM-AFM; low Q is needed for high Q force sensors such as the quartz tuning fork. [10] Because of these conditions, reduction of Q as well as its enhancement are both required in AM-AFM. Meanwhile, there have been many debates about the effect of Q-control on the noise. It has been claimed that higher effective Q-factor confers little advantage in the signal-to-noise ratio because thermal noise is also amplified by Q-control in AM-AFM. [11] On the other hand, Kobayashi *et al.* demonstrated that the force sensitivity can be increased by Q-control

in phase-modulation (PM)-AFM, [12, 13] where the minimum detectable force was found to be proportional to $Q^{-1/2}$ for high Q. However, no experimental investigation of noise control using Q-control has been performed in AM-AFM so far. Besides, how the Q-control affects the noise in AM-AFM has not been clearly understood either.

In this chapter, the dependence of effective Q-factor on the noise of oscillation amplitude, phase and force gradient in AM-AFM is addressed. It is shown that the standard deviation of the phase fluctuation is the same as that of amplitude fluctuation divided by oscillation amplitude, which validates the method for quantification of noise. Based on this method, it is exhibited that the signal-to-noise ratio does not explicitly change by Q-control. Nevertheless, it is demonstrated that the minimum detectable force gradient can be adjusted by using Q-control, which is shown to be proportional to Q^{-1} with large bandwidths.

4.2 Theory

Interaction stiffness has been frequently employed for quantitative description of the tip-sample interaction force. [14–17] To find the conversion formula of the interaction stiffness from the amplitude and phase, the response of QTF is considered when an external force is exerted. First of all, the equation of motion for an oscillator driven by a force F_0 in the absence of interaction (i.e.,

free oscillation) is

$$m_0\ddot{x}^{(0)} + b_0\dot{x}^{(0)} + k_0x^{(0)} = F_0e^{\imath\omega t}, \tag{4.1}$$

where the displacement at free oscillation $x^{(0)}(t)$ can be written as $x^{(0)}(t) = A_0e^{\imath(\omega t+\varphi)}$ (here A_0 is the amplitude of free oscillation and φ is the phase difference between the driving force and the displacement at the driving frequency ω). When the driving frequency is equal to the resonance frequency, i.e., $\omega = \omega_0$, then $\varphi = -\pi/2$. If the interaction force F_{int} is exerted on the force sensor, the equation of motion becomes

$$m_0\ddot{x} + b_0\dot{x} + k_0x = F_0e^{\imath\omega t} + F_{\text{int}}, \tag{4.2}$$

and the displacement $x(t)$ in the presence of interaction is expressed by $x(t) = Ae^{\imath\theta}e^{\imath(\omega t+\varphi)}$ where A is the amplitude in the presence of interaction and θ is the difference between the phases with and without the interaction at the driving frequency. If the oscillation amplitude is small compared to the characteristic length of the interaction [18–20] F_{int} is given by

$$F_{\text{int}} = -b_{\text{int}}\dot{x} - k_{\text{int}}x. \tag{4.3}$$

where b_{int} and k_{int} denote the damping coefficient and the stiffness of the exerted interaction, respectively.

Inserting Eq. (4.3) into Eq. (4.2) and subtracting Eq. (4.1) from Eq. (4.2) to eliminate F_0 yield,

$$\imath b_{\text{int}}\omega + k_{\text{int}} = \left(-m_0\omega^2 + \imath b_0\omega + k_0\right) \cdot f(A, \theta), \tag{4.4}$$

where

$$f(A,\theta) = \left(\frac{A_0}{A}\cos\theta - 1\right) + \imath\left(-\frac{A_0}{A}\sin\theta\right). \tag{4.5}$$

Comparing the real part on both sides, the conversion formula for $k_{\rm int}$ is obtained;

$$k_{\rm int} = k_0\left[\frac{\omega}{Q\omega_0}\frac{A_0}{A}\sin\theta + \left(1-\frac{\omega^2}{\omega_0^2}\right)\left(\frac{A_0}{A}\cos\theta - 1\right)\right]. \tag{4.6}$$

Note that the conversion formula for $b_{\rm int}$ is also obtained from the imaginary part, which is expressed by

$$b_{\rm int} = \frac{k_0}{\omega}\left[\frac{\omega}{Q\omega_0}\left(\frac{A_0}{A}\cos\theta - 1\right) - \left(1-\frac{\omega^2}{\omega_0^2}\right)\frac{A_0}{A}\sin\theta\right]. \tag{4.7}$$

Equations (4.6) and (4.7) are exactly equivalent to those in the previous studies (see Appendix B.2 for more details). [15, 18, 19] A_0 and θ in previous studies represent the peak amplitude at the resonance frequency (not the driving frequency) in the absence of interaction, and the phase at the driving frequency in the presence of interaction with respect to the phase at the resonance frequency without interaction, respectively.

4.3 Experimental Details

The experiments were performed with our home-built AM-AFM that employs a quartz tuning fork (QTF)[†] as the force sensor in ambient conditions at temperature $T = 297.9 \pm 0.5$ K. It was experimentally determined that the effective stiffness of QTF was $k_0 = 3820$ N/m by the mass-attachment method, [21, 22]

[†]Epson C-004R purchased from Digikey Corporation

and its piezoelectric coupling constant $\alpha = 5.99\ \mu$C/m by direct observation via an optical microscope. [22] The QTF was driven at the resonance frequency, $f_0 = 32.76$ kHz by using a function generator (33120A, Agilent Technologies) that was equipped with a 1/1000 voltage divider. The resulting current due to oscillation of QTF was converted and amplified into voltage by a preamplifier. A lock-in amplifier (SR830, Standard Research Systems) decomposed the output into amplitude and phase, which were recorded by a computer. Part of the signal that passed through the preamplifier was fed back to the driving signal to the QTF via our home-made feedback circuit to control the quality factor. [10]

4.4 Results and Discussion

4.4.1 The fluctuation of amplitude and phase

Figure 4.1(a) shows the measured phase as a function of time for several oscillation amplitudes. It clearly shows that the larger oscillation amplitude results in the smaller fluctuation of the phase. To investigate the fluctuation quantitatively, it was analyzed the standard deviation (SD) of the fluctuation of the phase and amplitude when the signal reaches the steady state.[‡] Figure 4.1(b) presents $\delta\theta$ (SD of phase) and $\delta A/A_0$ (SD of amplitude divided by the oscillation amplitude) as a function of A_0 for various bandwidths B which were controlled by adjusting the time constant of the lock-in amplifier.

[‡]The data analysis started after the initial two seconds during which the transient signal dies away and the steady state is reached.

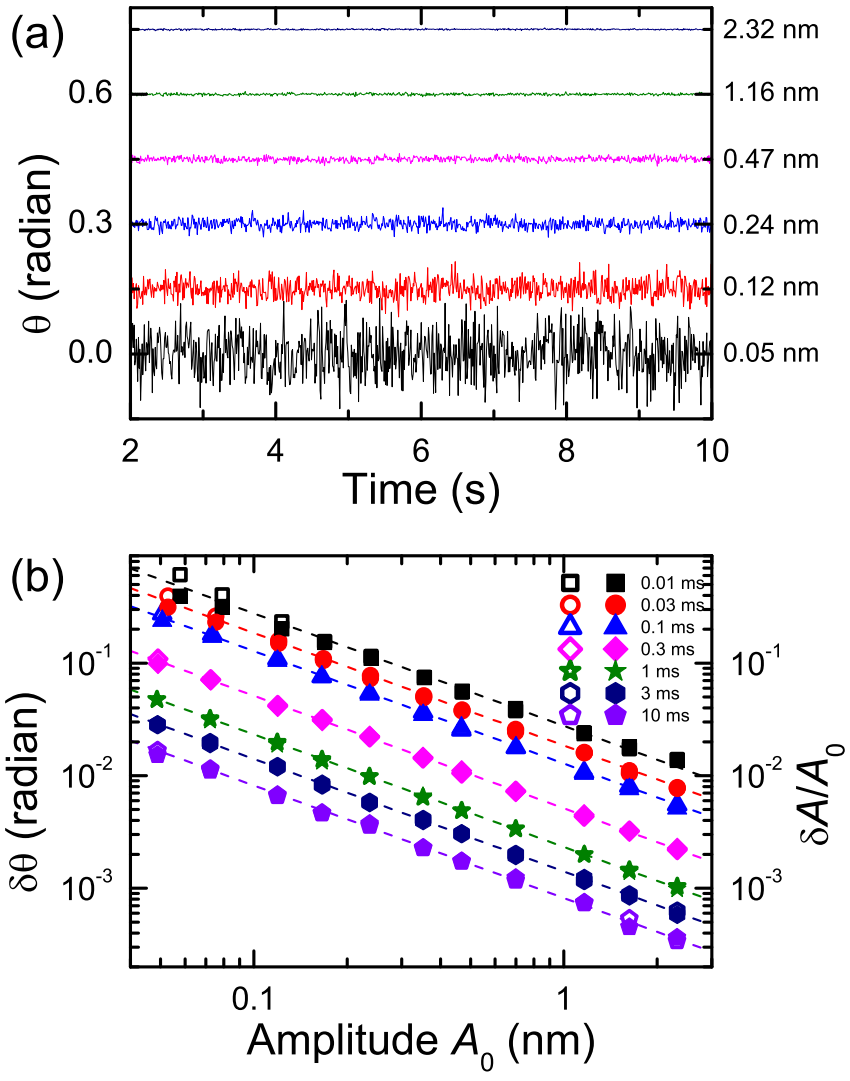

Figure 4.1: (a) The fluctuation of the phase in time domain for several values of A_0 is shown for $\tau = 1$ ms, and the successive curves are presented with the offset just for clear eye guide. (b) Log-log plots of standard deviation (SD) of the phase, $\delta\theta$ (open points) and SD of the amplitude divided by the oscillation amplitude, $\delta A/A_0$ (filled points) are presented as a function of the rms amplitude A_0 for several time constants τ of lock-in amplifier. The linear fit for SD of the phase exhibits the slope of -1.00. Adapted from Kim *et al.* [1]

It is observed that, first of all, $\delta A/A_0$ is inversely proportional to the oscillation amplitude A_0, which indicates that the noise on the amplitude is constant independent of the oscillation amplitude. In addition, the slope of the plot of $\delta\theta$ versus B was found to be 0.541 ± 0.029 (not shown here), close to $1/2$, suggesting that the noise density is also constant. Besides, $\delta\theta$ is shown to be the same as $\delta A/A_0$, which agrees with the result in PM-AFM, [12] and which also implies that $\delta\theta$ denotes an inverse of the signal-to-noise ratio. From these results, it is confirmed that the standard deviation of phase or amplitude measurement is an excellent measure of noise.

4.4.2 The effect of the Q-control

Figure 4.2 depicts the phase and the amplitude measured as a function of the driving frequency f. The effective quality factor, Q_{eff}, was either enhanced or reduced with respect to the quality factor without Q-control, $Q = 6070$, by controlling the gain of the feedback circuit. It was also observed that the peak amplitude grows as Q_{eff} increases as shown in the inset of Fig. 4.2, which is consistent with the literature. [10, 23]

Let us have a close look at the phase curve with respect to Q-control. A slight shift of the resonance frequency was observed as shown in Fig. 4.2, which is due to parasitic capacitance of electrically-driven QTF. [10] In addition, it was found that as Q_{eff} gets larger, the slope of the phase-frequency graph becomes steeper near the resonance frequency, which is in has good agreement with theoretical study. [24] This indicates smaller frequency fluctuation for larger

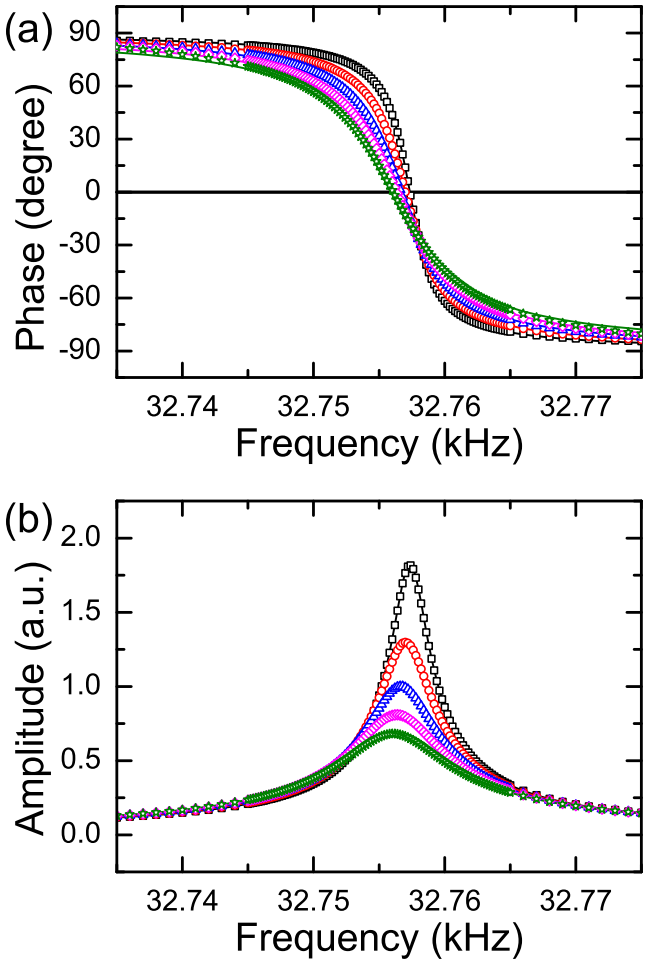

Figure 4.2: (a) The measured phases (open points) and their fits (solid lines) for several effective quality factors are presented as a function of the driving frequency. Squares, circles, triangles, diamonds and stars correspond to the effective quality factor Q_{eff} of 11500, 8050, 6070, 4820, and 3990, respectively. It is clearly observed that the Q-control changes the slope of phase-frequency curve near the resonance frequency. (b) The amplitude response which was obtained by simultaneous measurement of the phase is shown. Here the peak amplitude of the original resonance curve without Q-control ($Q = 6070$) was set to unity. Adapted from Kim *et al.* [1]

Q_{eff} under the same phase fluctuation. In other words, the slope of the phase-frequency graph at the resonance frequency, which is given by

$$\left|\frac{\Delta\theta}{\Delta f}\right| = \frac{2Q_{\text{eff}}}{f_0} = \frac{1}{f_{\text{c}}} \,, \tag{4.8}$$

is proportional to the effective quality factor, Q_{eff}, and roughly constant within $f_0 \pm f_{\text{c}}$ where f_{c} is called the cutoff frequency. [9] It is worth emphasizing that this change of the slope is important in the evolution of the phase fluctuation $\delta\theta$ to the frequency fluctuation δf, i.e.,

$$\delta f = \left|\frac{\Delta f}{\Delta\theta}\right| \delta\theta = \left(\frac{f_0}{2Q_{\text{eff}}}\right) \delta\theta \,, \tag{4.9}$$

and to the fluctuation of force gradient as discussed below.

4.4.3 The signal-to-noise ratio under Q-control

The influence of Q-control on the phase fluctuation and then on the fluctuation of force gradient is now addressed. Figure 4.3 shows that the measured noise on the phase, $\delta\theta$, versus the effective quality factor, Q_{eff}, for various bandwidths when the oscillation amplitude is $A_0 = 0.1$ nm. It was found that $\delta\theta$ is almost constant as Q_{eff} changes, indicating the noise on the phase, $\delta\theta$, the inverse of signal-to-noise ratio, does not change by Q-control. As pointed out by Ashby, [11] it implies that Q-control amplifies the noise as well as the signal when Q_{eff} is increased. In addition, it was observed that the phase noise is increased for large Q_{eff} and small bandwidths (long time constants), suggesting the signal decreases due to small bandwidths comparable to the cutoff frequency f_{c}. For

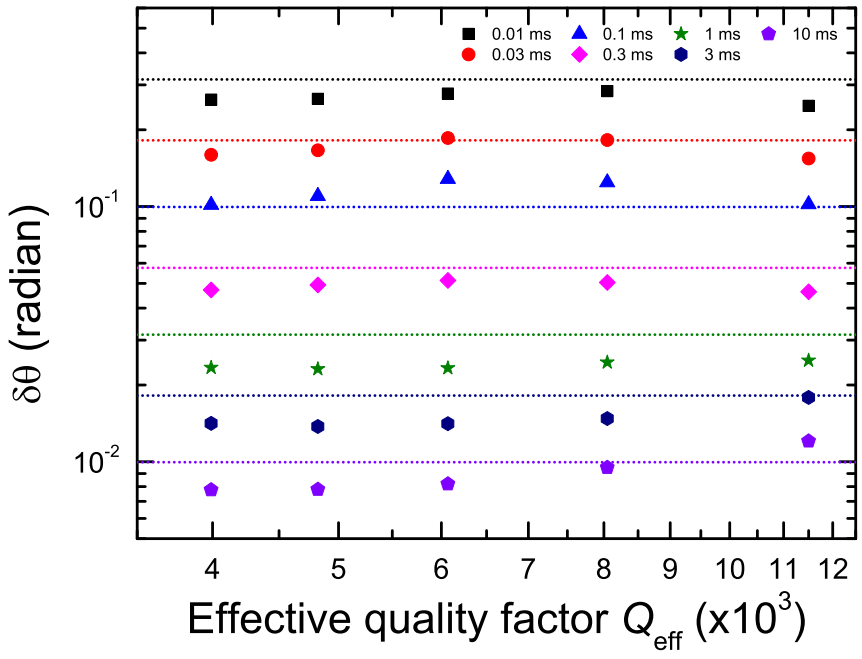

Figure 4.3: The noise on the phase, $\delta\theta$, as a function of the effective quality factor, Q_{eff}, for various bandwidths is depicted when the amplitude is $A_0 = 0.1$ nm (rms). The dashed line of each bandwidth is the theoretical value obtained from Eq. (4.12). The noise on the phase, or the inverse of signal-to-noise ratio, does not change by Q-control. Adapted from Kim *et al.* [1]

example, the half of bandwidth $B/2 = 3.9$ Hz for $\tau = 10$ ms is comparable to $f_c = 2.70$ Hz for $Q_{\text{eff}} = 11500$. The results of phase fluctuation show that Q-control has no advantage in the signal-to-noise ratio in AM-AFM, which is in good agreement with the previous study. [11]

To compare the experimental results to the theoretical ones quantitatively, the thermal noise is considered because the noise density was found to be constant (see Fig. 4.1). The magnitude of the random driving force is given by [9] $F_{\text{th}} = \sqrt{(2k_0 k_B T)/(\pi f_0 Q)}$, where k_B is the Boltzmann constant. In addition, the magnitude of the transfer function $|G(f)|$ is given by

$$|G(f)| = \frac{1}{k_0} \frac{1}{\left[\left(1 - f^2/f_0^2\right)^2 + \left(f/f_0 Q\right)^2 \right]^{1/2}} , \tag{4.10}$$

which becomes $|G(f)| = Q/k_0$ when the force sensor is driven at the resonance frequency. The thermal displacement noise density $n_{\text{th}} = |G(f)|\, F_{\text{th}}$ is given by

$$n_{\text{th}} = \sqrt{\frac{2k_B T Q}{\pi f_0 k_0}} . \tag{4.11}$$

The thermal fluctuation on the phase, θ_{th}, is then given by

$$\delta\theta_{\text{th}} = \frac{\delta A_{\text{th}}}{A_0} = \sqrt{\frac{2k_B T Q B}{\pi f_0 k_0 A_0^2}} . \tag{4.12}$$

The thermal noise on the phase calculated using Eq. (4.12) is also presented as the dashed lines in Fig. 4.3. It is observed that thermal noise is dominant in this experiment, and that the quality factor Q instead of Q_{eff} was involved in Eq. (4.12).

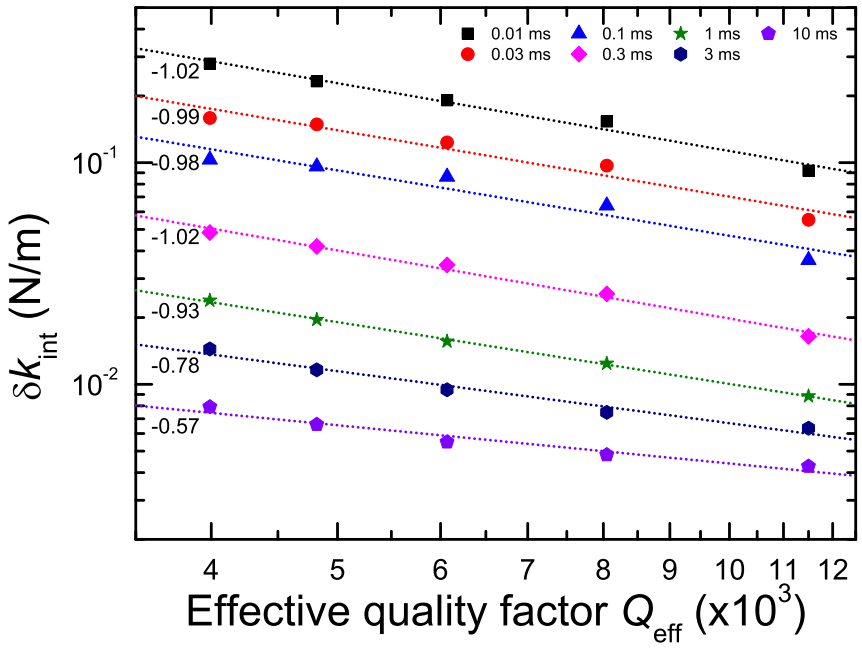

Figure 4.4: Log-log plots of the noise of the interaction stiffness at the rms oscillation amplitude of 0.1 nm versus the effective quality factor Q_{eff} for several time constants are presented. Each dashed line denotes the linear fit, and the value shown at the left-end of the line represents its slope. Adapted from Kim *et al.* [1]

4.4.4 The noise on the interaction stiffness under Q-control

Now how Q-control affects the interaction stiffness is discussed. Figure 4.4 shows the noise on the interaction stiffness (or the minimum detectable force gradient), $\delta k_{\rm int}$, in Q-controlled system for various bandwidths when the oscillation amplitude is 0.1 nm. The interaction stiffness, $k_{\rm int}$, was obtained by using Eq. (4.6) in terms of the measured amplitude A and phase θ. It is worth emphasizing that $Q_{\rm eff}$ should be introduced instead of Q in Eq. (4.6) because the interaction stiffness is obtained from the frequency shift due to the interaction forces.

Interestingly, it was found that large Q reduces $\delta k_{\rm int}$, which clearly shows the improved force sensitivity in AFM with the increase of Q. In particular, $\delta k_{\rm int}$ was observed to be proportional to $Q_{\rm eff}^{-1}$ for large bandwidths. This is not an expected result because the minimum detectable force gradient due to thermal noise is given by [5]

$$\delta k_{\rm int,th} = \sqrt{\frac{2k_0 k_{\rm B} T B}{\pi f_0 Q A_0^2}} \ , \tag{4.13}$$

which is proportional to $Q^{-1/2}$.

To resolve this discrepancy, the relation between $\delta k_{\rm int}$ and $\delta\theta$ is required to be found. For the first step, the frequency shift Δf due to a small interaction stiffness $k_{\rm int}$ is given by [17]

$$\Delta f = f_0 \left(\frac{k_{\rm int}}{2k_0} \right) \ . \tag{4.14}$$

Combining Eq. (4.14) with Eq. (4.9), the noise on the interaction stiffness, $\delta k_{\rm int}$, is given by

$$\delta k_{\rm int} = \left(\frac{2k_0}{f_0} \right) \delta f = \left(\frac{k_0}{Q_{\rm eff}} \right) \delta\theta \ , \tag{4.15}$$

where δf is the frequency noise. Equation (4.15) indicates that the noise on the interaction stiffness, or the minimum detectable force gradient, is inversely proportional to Q_{eff} under the same phase fluctuation $\delta\theta$. Then the relation between the noise on the interaction stiffness with Q-control δk_{int} and that without Q-control $\delta k_{\text{int}}^{(0)}$ is given by

$$\delta k_{\text{int}} = \left(\frac{Q}{Q_{\text{eff}}}\right) \delta k_{\text{int}}^{(0)} \ . \tag{4.16}$$

The result shown in Fig. 4.4 is consistent with Eq. (4.16), which clearly shows that the minimum detectable force gradient (or δk_{int}) and the minimum detectable interaction force δF are inversely proportional to Q_{eff} for sufficiently large bandwidths. It is important to note that when the phase fluctuation $\delta\theta$, or the deflection fluctuation δA is constant, Eq. (4.16) holds no matter what kind of noise actually works.

In spite of the controllability of the force sensitivity, there is a trade-off between the minimum detectable force gradient and the scan speed, which is inversely proportional to the relaxation time of the force sensor in AM-AFM. The relaxation time, which is the time constant of a change until the signal at one state reaches another steady state, is given by $\tau_{\text{sensor}} = Q_{\text{eff}}/(2\pi f_0)$, [10] which is proportional to Q_{eff}. It implies that when Q_{eff} is adjusted to κQ, δk_{int} and τ_{sensor} becomes, respectively, $1/\kappa$ and κ times their original values without Q-control, and correspondingly the scan speed under Q-control becomes $1/\kappa$ times the speed without Q-control. Therefore, the effective quality factor Q_{eff} can be properly selected using Q-control depending on the specific purpose such

as the increased sensitivity or the increased measurement speed in AM-AFM.

Comparing with the result obtained in PM-AFM, where δF is proportional to $Q_{\text{eff}}^{-1/2}$ for large bandwidths, [12, 13] it is inconsistent with our result in AM-AFM. It is because the noise on the amplitude (the deflection noise) δA (or $\delta\theta$) is proportional to $Q_{\text{eff}}^{1/2}$ in PM-AFM, whereas $\delta\theta$ is independent of Q_{eff} in AM-AFM. Therefore, the enhancement or reduction of the force sensitivity both in AM-AFM and in PM-AFM results from the variation of the slope in the phase-frequency plot (see Fig. 4.2). In addition, the $1/Q_{\text{eff}}$-dependence of δk_{int} in Q-controlled AM-AFM is similar to the oscillator noise in FM-AFM, [9, 17] because the frequency noise due to the oscillator noise, δf_{osc}, is proportional to the derivative of frequency with respect to phase shift, $\Delta f/\Delta\theta$. [9]

4.5 Conclusions

It has been demonstrated that the minimum detectable force gradient is adjustable by Q-control in QTF-based AM-AFM. It has been found that the noise on the phase is identical to the noise on the amplitude divided by the oscillation amplitude, which indicates that the standard deviation of the phase or amplitude is a proper measure of noise. It has also shown that while the signal-to-noise ratio does not change under Q-control, the minimum detectable force gradient is inversely proportional to the effective quality factor for sufficiently large bandwidths. Therefore, Q-control can be employed to enhance the force sensitivity or the scanning speed in AM-AFM.

References

[1] J. Kim, B. Sung, B. I. Kim, and W. Jhe, J. Appl. Phys. **114**, 054302 (2013).

[2] G. Binnig, C. F. Quate, and C. Gerber, Phys. Rev. Lett. **56**, 930 (1986).

[3] F. J. Giessibl, S. Hembacher, H. Bielefeldt, and J. Mannhart, Science **289**, 422 (2000).

[4] L. Gross *et al.*, Science **324**, 1428 (2009).

[5] *Springer Handbook of Nanotechnology*, 3rd ed., edited by B. Bhushan (Springer-Verlag, Heidelberg, 2010).

[6] S. E. Cross, Y.-S. Jin, J. Rao, and J. K. Gimzewski, Nat. Nanotechnol. **2**, 780 (2007).

[7] M. J. Higgins *et al.*, Nanotechnology **16**, S85 (2005).

[8] T. Ando *et al.*, P. Natl. Acad. Sci. USA **98**, 12468 (2001).

[9] K. Kobayashi, H. Yamada, and K. Matsushige, Rev. Sci. Instrum. **80**, 043708 (2009).

[10] J. Jahng *et al.*, Appl. Phys. Lett. **91**, 023103 (2007).

[11] P. D. Ashby, Appl. Phys. Lett. **91**, 254102 (2007).

[12] N. Kobayashi *et al.*, J. Appl. Phys. **103**, 054305 (2008).

[13] N. Kobayashi *et al.*, Appl. Phys. Lett. **97**, 011906 (2010).

[14] S. H. Khan, G. Matei, S. Patil, and P. M. Hoffmann, Phys. Rev. Lett. **105**, 106101 (2010).

[15] M. Lee, B. Sung, N. Hashemi, and W. Jhe, Faraday Discuss. **141**, 415 (2009).

[16] S. An *et al.*, Appl. Phys. Lett. **101**, 053114 (2012).

[17] F. J. Giessibl *et al.*, Phys. Rev. B **84**, 125409 (2011).

[18] M. Lee, J. Jahng, K. Kim, and W. Jhe, Appl. Phys. Lett. **91**, 023117 (2007).

[19] M. Lee and W. Jhe, Phys. Rev. Lett. **97**, 036104 (2006).

[20] S. Jeffery *et al.*, Phys. Rev. B **70**, 054114 (2004).

[21] J. P. Cleveland, S. Manne, D. Bocek, and P. K. Hansma, Rev. Sci. Instrum. **64**, 403 (1993).

[22] A. Castellanos-Gomez, N. Agraït, and G. Rubio-Bollinger, Nanotechnology **20**, 215502 (2009).

[23] J. Jahng *et al.*, Phys. Rev. A **84**, 022318 (2011).

[24] H. Hölscher, D. Ebeling, and U. D. Schwarz, J. Appl. Phys. **99**, 084311 (2006).

Chapter 5

Observation of the mechanical relaxation time in the elongated water nanobridge*

5.1 Introduction

There are many examples in the fields of chemistry, physics, and tribology, where the water are not in the bulk state, but in confined geometries and small numbers. [2–6] The dynamics of the confined water is known to be different from the bulk. There are many model systems of the confined water such as water nanofilm, water nanodroplet, and water nanobridge.

First, the water nanofilm is the water confined between two solid surfaces.

*This chapter was modified and rewritten on the basis of the work which was accepted to J. Phys. Chem. Lett. [1]

Studies on the water nanofilm has been performed mainly by force measurements using surface force apparatus (SFA) [7–9] or atomic force microscope (AFM). [3,4,10,11] It has been reported that the water shows more viscous than the bulk and solid-like response as the gap between the two surfaces is commensurate to the size of a water molecule. [4, 8, 10, 11] In particular, Hoffmann and his co-workers showed the solid-like response of water nanofilm depends on the approach rate via its mechanical relaxation time, which is independent of tip size. [4]

Second, the water nanodroplet (or water nanopool) has been widely used as a model system of the confined water in reverse micelles. [12] The water nanodroplet is surrounded by surfactants that have both hydrophobic and hydrophilic groups. The size of the nanopool is the order of several nanometers, which contains from 10^2 to 10^6 molecules of water. [13] Optical measurements showed that the dynamics of the confined water is significantly slower than bulk water dynamics, and it depends on its size. [13,14] Fayer and his co-workers suggested and tested the core-shell model to describe the slow dynamics of hydrogen bonding network. [13] Comparing the dynamics of the water confined in surfactants with ionic and nonionic head groups, it was shown that the slow dynamics of hydrogen bonding network is attributed to the confinement, but it is not attributed to the nature of the interface. [15] There has been considerable debate as to whether the nanoconfinement or droplet size down to the nanometric scale affects the structural rearrangements of liquid water. The slow dynamics of water in nanodroplets has been observed by several techniques, [13–17] but it

remained unclear whether the water mobility in nanodroplets decreases overall, or whether molecules located near the surface and in the core of the droplets show different dynamic behavior.

Lastly, the water nanobridge (or water nanomeniscus) is also another form of confined water in nature, which plays a crucial role in a wide range of surface science and technology such as adhesion, [2, 18] friction [5, 6, 19] and nanolithography. [20] The atomic force microscope (AFM) with a sharp tip (with a radius of curvature of typically 10 to 100 nm) has enabled numerous experimental studies of a single asperity of liquid. [21–24] In particular, it was reported that the experimental results are well explained by a theoretical model that considers constant water volume and decrease of water meniscus curvature during its elongation. [22] It was demonstrated that the viscoelastic properties of the water nanobridge can be simultaneously measured by using non-contact AFM based on the quartz tuning fork (QTF) during its manipulation. [23] However, the quantitative approach about its viscoelastic properties has been limited due to insufficient information of its cross-sectional area.

In this chapter, the mechanical properties of the water nanomeniscus is investigated as a function of the tip-sample distance using the non-contact AFM. A key advantage of the QTF-based AFM is that one can precisely manipulate the nanometric water column and change its shape by controlling the tip-sample distance while avoiding its mechanical instability due to contact damage with the sample surface. In particular, it is observed that the mechanical relaxation time, which is independent of the cross-sectional area, increases with

increasing the tip-sample distance, whereas it is not relevant to the volume of the nanobridge. These experimental results provide experimental evidence that the dynamic behavior of interfacial water molecules is different from that of molecules inside the bridge.

5.2 Materials and Methods

Experiments were carried out with a home-built amplitude modulation AFM that uses QTF as the force sensor. Since the QTF employed in this setup has a high effective stiffness ($k_0 = 3.35$ kN/m) and high quality factor ($Q \approx 5000$), the mechanical instability due to the interacting force between the tip and sample can be avoided and thus the formed water column can be precisely manipulated. In addition, the self-sensing property of QTF allows to measure the interacting forces without optical detection. [25] A function generator was employed to operate the QTF sinusoidally with a root-mean-square amplitude of $A_0 = 0.34$ nm at its resonant frequency, 32.7 kHz. A preamplifier amplified and converted the resulting current from QTF into voltage. A lock-in amplifier decomposed the signal into amplitude and phase, which were analyzed by a computer.

A silicon tip (CSG10, NT-MDT) with a nominal radius of curvature of 10 nm was attached to a prong of QTF to produce lateral oscillation with respect to the atomically flat muscovite mica (Grade V-1, SPI Chem.) sample. The mica was cleaved using an adhesive tape, rinsed by dilute acetic acid to ex-

change potassium ions for hydrogen ions on the cleaved surface, [26,27] washed with deionized water and then dried with nitrogen gas. The tip was cleaned by sufficient rinse with deionized water. The tip-sample distance was controlled by a commercial piezoelectric tube (PZT, Physik Instrumente). The tip, sample and PZT were contained in an air-tight acrylic chamber. In preparation of the experiment, the chamber was flushed with dry nitrogen and then the relative humidity in the chamber was regulated by injecting nitrogen that contains deionized water vapor. The relative humidity was continuously monitored by a sensor (SHT75, Sensirion, specified accuracy $< 1.8\%$), placed at 2 cm away from the sample.

The approach-retraction curves were obtained repeatedly at several different positions on the sample where the tip approaches at almost constant relative humidity. The amplitude and phase of the oscillating tip were recorded every 10 ms and the stepwise tip-sample distance was controlled by the PZT every 500 ms during acquisition of the approach-retraction curves. [24] The interaction stiffness, damping coefficient and mechanical relaxation time were calculated from the measured amplitude and phase for all the time-resolved data, and then their average and standard deviation at each PZT displacement were obtained by statistical analysis.

The thermal drift of the tip-sample distance was observed by monitoring the displacement of the PZT and the time as retraction started right after the tip-oscillation amplitude became smaller than a specific ratio of the free oscillation amplitude. The relative time, the PZT displacement, and the amplitude

and phase signals were recorded by the computer during more than three consecutive approach-retraction cycles. The drift speed was then calculated with respect to the time and the PZT displacement at the tip-retraction point while assuming the drift speed is constant during cycles. The compensation of the thermal drift was found to work well and thus convince the reproducibility of the force-distance curves when the compensated curves are overlapped onto a single curve, especially in the tip-sample contact region.

5.3 Results and Discussion

Figure 5.1 shows the measured interaction stiffness and damping coefficient while the retraction speed is varied. The retraction speed was controlled by changing the time elapsed between successive displacements of the piezoelectric tube (PZT), we call the staying time t_s, at the fixed distance interval (0.15 nm). This staying time t_s for each PZT displacement was 0.5, 0.7 and 1.0 s, which corresponds to the retraction speed of 0.3, 0.21 and 0.15 nm/s, respectively. The approach speed is 0.3 nm/s, which is very slow compared to the previous studies, [22] and the drift of the tip-sample distance due to thermal fluctuation (typically less than 10 pm/s) is systematically compensated (see Materials and Methods). The interaction stiffness (k_{int}) and damping coefficient (b_{int}) are obtained by the measured amplitude and phase of the probe oscillation. [28] Notice that the interaction stiffness (k_{int}) represents the lateral stiffness experienced by the probe for the tip-sample interaction forces. Since the damping

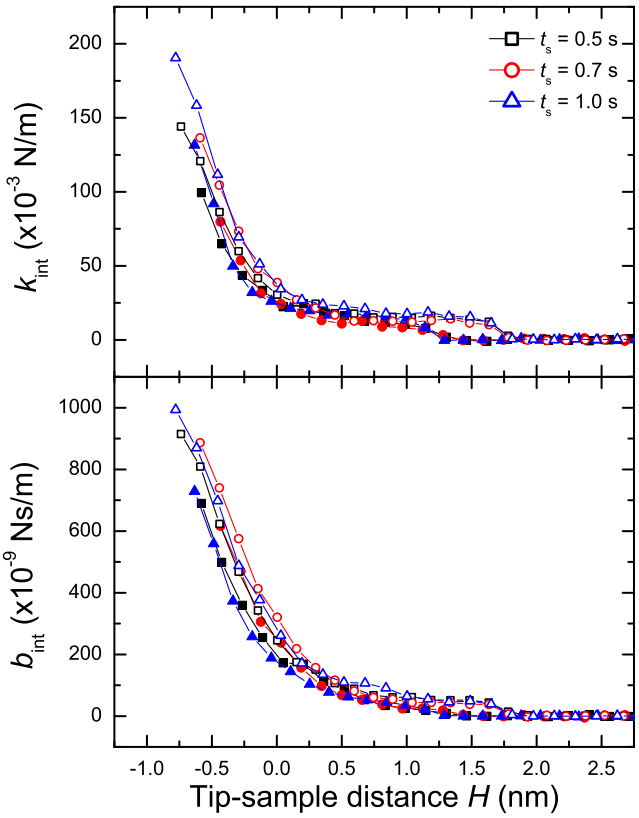

Figure 5.1: The interaction stiffness k_{int} and damping coefficient b_{int} as a function of the tip-sample distance H for different retraction speed or staying time t_{s} when the relative humidity is 32%. The filled points denote the experimental results obtained during approach with $t_{\mathrm{s}} = 0.5$ s while the open points represent each measurement by varying t_{s} during retraction. The data were taken at various positions on the sample. Adapted from Kim *et al.* [1]

coefficient (b_{int}) is a proportionality constant appearing in the dissipated energy per oscillation, $E_{\text{dis}} = \pi b_{\text{int}} \omega A^2$ (ω is the driving angular frequency of QTF), the energy dissipation is due to the hysteresis during one period of the QTF motion resulting from the friction at the nanoscale.

As shown in Fig. 5.1, we cannot find any noticeable dependence of the measured results on the vertical scan speed, in particular, at $H > 0$. This is consistent with the previous experimental study, in which the acquisition time (i.e., the elapsed time to obtain an approach-retraction curve) was varied from 0.01 to 10 s. [22] It indicates that the evaporation process is negligible during the retraction, and the water nanobridge can be considered as water confined by the tip, sample, and air/water interface. The slow evaporation might be attributed to the negative pressure of the water nanobridge.

Figures 5.2a and 5.2b show the approach-retraction curves in which both k_{int} and b_{int} exhibit hysteretic behaviors when RH is 19%. The hysteresis indicates that the existence of the water column between the tip and sample, [21–23] which was formed at $H_{\text{form}} = 0.9$ nm and ruptured at $H_{\text{rup}} = 1.7$ nm. The formation and rupture of the water meniscus are also confirmed by the temporal behaviors of its mechanical responses (see Appendix C). The water meniscus shown in Fig. 5.2 was ruptured at $H_{\text{rup}} = 1.7$ nm, shorter than previous results, [21–23] but is rather comparable to a recent simulation. [29] Assuming that the contact angle of water on mica as well as on silicon that is easily oxidized in air is zero, the volume of the bridge is estimated to be at most

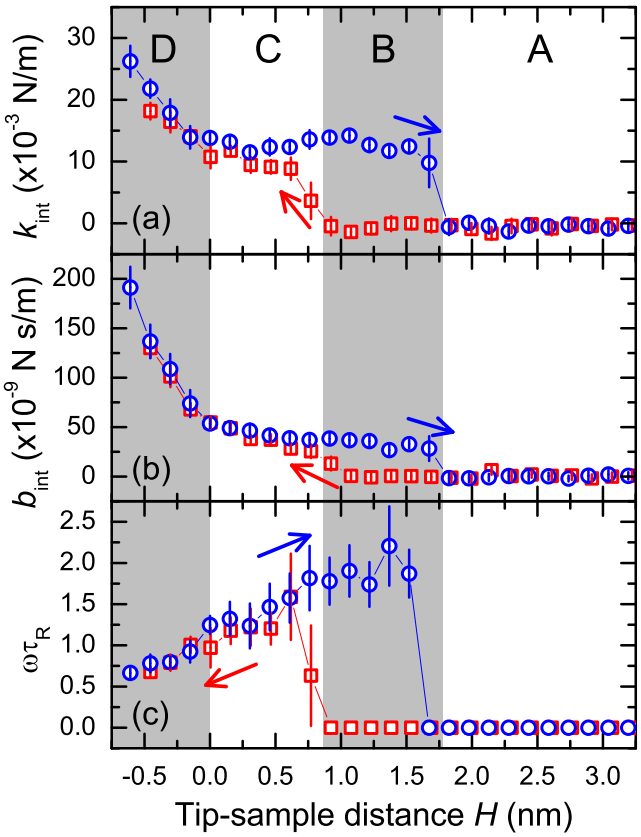

Figure 5.2: (a) The interaction stiffness k_{int}, (b) damping coefficient b_{int} and (c) relaxation time τ_{R} multiplied by the driving angular frequency ω as a function of the tip-sample distance H, where the effect of nanometric water column is present. Squares (red) and circles (blue) represent the measured values during approach and retraction, respectively. The differing regions with respect to H show the differing stability states associated with the water nanomeniscus. Adapted from Kim *et al.* [1]

4.91 nm^3, which corresponds to 164 molecules of water.[†] This number of water molecules shown here is similar to that of water molecules confined in the reverse micelles. [14] The temporal behaviors of k_{int} and b_{int} remain almost constant at each tip-sample distance. These result indicates that the nanometric water meniscus is almost non-volatile, that is, its evaporation during retraction is negligible, which is also consistent with the previous study. [22] Thus the volume of the liquid bridge V_b is related with the rupture distance H_{rup} as given by $H_{rup} = (1 + \theta/4)[V_b^{1/3} - (2/5R)V_b^{2/3}]$. [30] The contact angle θ is assumed to be zero and since $R \gg V_b^{1/3}$, the volume of the bridge is approximated by $V_b \approx H_{rup}^3$.

As far as the stability of the water column is concerned, the approach-retraction curve can be divided into four regions. When H is larger than H_{rup} (Region A), there does not exist any difference between the approach and retraction within the experimental resolution. It indicates that the probe experiences only the force exerted in free space, where the stable state in this region is the state in which the water bridge is absent, i.e., in the vapor state of water.

While the water bridge does not exist during approach, it does exist during retraction when $H_{form} < H < H_{rup}$ (Region B), which implies the coexistence of two states. One is the state in which the water bridge exists between the tip and sample and the other is the state of its absence. Those two states correspond to two local minima in the grand potential. The state at the global minimum

[†]The volume of a water molecule is $V_{H_2O} = 0.03$ nm^3 because the molar mass and the density of liquid water are 18 g/mol and 1 g/cm^3, respectively.

corresponds to the stable state, while the other one having the higher-energy local minimum is the metastable state. The characteristics of these states strongly depend on the tip-sample distance, which determines the relative barrier heights associated with the thermodynamic processes of the meniscus formation as well as its rupture. [31] The formation barrier is defined as the energy needed to overcome to form the water bridge and the rupture barrier as the energy required for its rupture, both of which strongly depend on the tip-sample distance. As the tip-sample distance increases, the rupture becomes more favorable than the formation because the rupture barrier drops whereas the formation barrier rises, and vice versa. Thus, the water bridge becomes less stable as the tip-sample distance increases whereas it gets more stable as the distance decreases. It is also found that both k_{int} and b_{int} decrease gradually during retraction, which is consistent with the previous experiments. [23, 32] The decrease in both k_{int} and b_{int} is attributed to the water column that becomes thinner as it is stretched more during retraction.

In $H < H_{\text{form}}$ (Region C), there is only slight difference between approach and retraction. After the meniscus formation, a rise in k_{int} and b_{int} is observed during with the tip approach, which indicates growth of the width of the water bridge. Notice that the oscillatory force behavior of the confined water, associated with the molecular layering of water molecules, [4, 33] is not observed in k_{int} and b_{int}, which is due to the absence of the bulk water reservoir and the consequent insufficient number of water molecules to be layered. [33] Both k_{int} and b_{int} increase at $H = H_{\text{form}}$ during approach, and this implies that

the water bridge forms between the tip and sample. [23] Since the water column is spontaneously capillary-condensed at $H = H_{\text{form}}$, the water bridge represents the stable state existing between the tip and sample, which agrees well with the previous discussion. [34] When the tip makes a further approach (Region D), it is found that the slopes of k_{int} and b_{int} change, which indicates that the tip is now in contact with the sample. The tip-sample contact point, or $H = 0$, is defined as the position where the slopes of both k_{int} and b_{int} make a rapid increase.

k_{int} and b_{int} are the quantities that depend on the meniscus size, such as the area and length of the water meniscus. As mentioned above, the water meniscus becomes thinner (which causes a decrease of its neck width) and longer (which results in an increase of its length) during retraction, which leads to a decrease of k_{int} and b_{int}, as detailed in the following. The quantities k_{int} and b_{int} are defined based on the viscoelastic Kelvin model where a spring and a dashpot are connected in parallel. If the strain x is applied to the water meniscus in the lateral direction with the angular frequency ω, the relationship between the lateral force F_{L} and x is given by,

$$\frac{F_{\text{L}}}{S} = G^* \frac{x}{H}, \tag{5.1}$$

where S is the (effective) area of the water meniscus and H is the tip-sample distance. G^* is the complex shear modulus that is expressed by $G^* = G' + iG''$. [3] Comparing both the real and imaginary parts of Eq. (5.1) with the equation

$$F_{\text{int}} = -k_{\text{int}} x - b_{\text{int}} \dot{x}, \tag{5.2}$$

allows the following two relations given by

$$k_{\mathrm{int}} = G' \frac{S}{H},\ b_{\mathrm{int}} = \frac{G''}{\omega} \frac{S}{H}. \tag{5.3}$$

The exact determination of G' and G'' has been difficult so far because the information on the meniscus area S is rather limited. Therefore, experimental determination or estimation of the area S may be a milestone for quantitative study of the mechanical properties of the water meniscus using the non-contact AFM technique.

The relaxation time (RT) τ_{R} multiplied by the angular frequency ω is a dimensionless quantity, which is given by, in the viscoelastic Maxwell model, [3, 35]

$$\omega\tau_{\mathrm{R}} = \frac{k_{\mathrm{int}}}{b_{\mathrm{int}}\omega} = \frac{G'}{G''} = \frac{1}{\tan\delta}\ . \tag{5.4}$$

Here, $\tan\delta$ is the loss tangent of the tip-sample interaction. [36] The RT represents the time constant associated with dissipation of the stress when an external strain is applied and it has been employed to understand the mechanical properties of the confined liquids. [4, 37] If the material behaves like liquid, RT is shortened, while if it shows a solid-like behavior, RT becomes lengthened. In addition, the advantageous feature of the RT analysis is that it is independent of the size of the tip. [4]

Figure 5.2c plots $\omega\tau_{\mathrm{R}}$ as a function of H. As shown, τ_{R} decreases as the tip approaches the sample after the formation of the water bridge, which indicates that the interaction exerted on the probe tip shows liquid-like behavior. Since the loss tangent of some polymers such as polystyrene and low-density polyethy-

lene is from approximately 0.02 to 0.2, [38] which corresponds to the from 5 to 50, the elongated water nanobridge is more liquid-like than the polymers. Comparing this result with Fig. 5.1c where the effect of the water meniscus is not found, it is observed that water plays a role as a lubricant between hydrophilic surfaces, whereas it shows differing properties with respect to the results obtained by using the hydrophilic tip and hydrophobic sample in friction force microscopy. [39] It was also observed an increase of τ_{R} for further indentation of the tip beyond the liquid-like response during approach. It indicates that the effects of the confined (or squeezed) water between two solid surfaces and the solid-solid interaction appear to be mixed together beyond the tip contact. As the indentation progresses further, the effect of the water meniscus associated with its squeezing dominates the solid-solid interaction. However, since the water meniscus is gradually squeezed out from the gap with further indentation, the solid-solid interaction eventually dominates the effect of confined water and as a result the relaxation time increases from then on. Notice that the existence of the intrinsic hydration water layer formed on the two hydrophilic surfaces in ambient conditions may in part contribute to the solid-solid interaction (for the repulsive mechanical properties of the hydration water layer). [40]

The increase of the relaxation time is observed during retraction, independent of the meniscus size (Fig. 5.3). The rise of τ_{R} for the elongated water column is different from previous investigations in which water confined between two solid surfaces shows a solid-like behavior when the distance between the two surfaces is commensurate with the molecular spacing of water. [4, 10, 11, 33, 41]

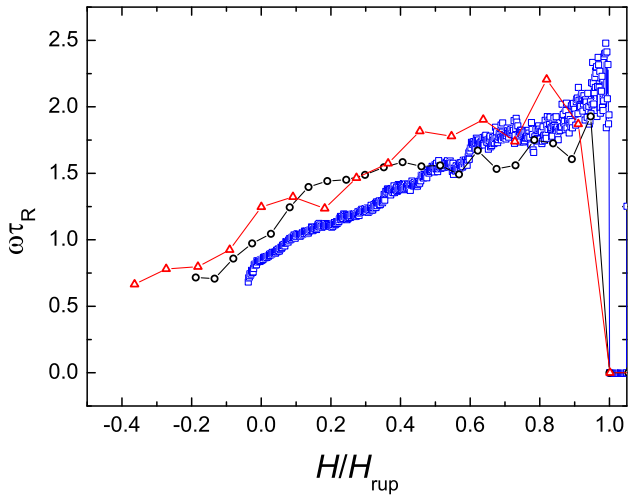

Figure 5.3: The mechanical relaxation time as a function of the normalized H, the ratio of the tip-sample distance H to the rupture distance H_{rup}, during retraction is plotted. Squares (blue), circles (black) and triangles (red) correspond to $H_{\mathrm{rup}} = 98$, 2.8 and 1.7 nm, respectively. Adapted from Kim *et al.* [1]

In particular, the behavior of the mechanical relaxation time is independent of the rupture distance H_{rup} (or volume V_{b}) of the water column in the range from 1.7 to 98 nm, which is varied by changing the tip size.

Since the mechanical relaxation time is independent of the sizes of the tip as well as the water meniscus, it may be described by a function of a dimensionless quantity. For a theoretical description of the formation of the water meniscus, the dimensionless quantity H/H_{c} (where H_{c} is the critical distance) was employed. [42] Intuitively, a similar approach may be also available to help understand the general behavior shown in Fig. 5.3. The volume of the water meniscus is directly related to the rupture distance H_{rup}. [22,30] In addition, an

increase of the tip-sample distance H also results in an increase of the surface area of the water meniscus. Therefore, the ratio H/H_{rup} may be an adequate dimensionless quantity, which roughly describes the surface-to-volume ratio of the water meniscus. In other words, the increased tip-sample distance causes an increase of its surface area during retraction, which in turn leads to the subsequent increase of the ratio of water molecules at the air/water interface to the total water molecules contained in the meniscus. The fundamental mechanism underlying such a general behavior is very interesting and needs further theoretical study for better understanding.

It has been shown by the sum-frequency vibrational spectroscopy that there is a strong hydrogen bond between water molecules at the air/water interface. [43] The orientational correlation of adjacent water molecules at the interface is manifested in the positive part of the imaginary susceptibility in 3000-3200 cm^{-1} region (called OH(x) band). [43, 44] The strong hydrogen bond between water molecules at the air/water interface may be thus attributed to the increased mechanical relaxation time of the elongated water nanobridge.

The dependence of the critical value of the relaxation time on the hydrophilicity of the surface and the relative humidity is an interesting challenge to be addressed as a future work. It is expected that the critical value of the mechanical relaxation time of the water meniscus may change when water at the air/water interface interacts with water molecules in the surrounding vapor because the strong H-bond at the air/water interfaces can be considered as resulting from the lack of hydrogen bond toward the vapor phase. [43] At a low

relative humidity (RH), the water meniscus is small and its length is short, so that the surface area involved in the interaction as well as the number of water molecules near the water meniscus are probably insufficiently low to produce the interaction. Thus, the critical value of the mechanical relaxation time may remain constant when RH is low. At a relatively high RH, on the other hand, water molecules in the vicinity of the water meniscus as well as the surface area may become sufficiently high to induce the interaction. Thus, the intermolecular bonds between water at the air/water interface and water molecules in the surrounding vapor may form and break incessantly. Such temporally fluctuating bonds probably weaken the lateral interaction at the interface. Therefore, the critical value of the relaxation time is expected to decrease as RH increases beyond a certain value of RH.

5.4 Concluding Remarks

The mechanical properties of the nanometric water column is investigated as a function of tip-sample distance by a non-contact atomic force microscope. It is observed that the mechanical relaxation time increases with the stretch of the water nanobridge, but the relevance of the volume of the nanobridge is not found. It indicates that the mechanical relaxation time does not depend on the size of the nanobridge, but does depend on its shape. These results experimental evidence that the dynamic behavior of interfacial water molecules is different from that of molecules inside the bridge. The water nanobridge is expected to be

introduced for a model system to investigate the water at the air/water interface using force spectroscopy.

References

[1] J. Kim, D. Won, B. Sung, and W. Jhe, J. Phys. Chem. Lett. , accepted.

[2] L. Bocquet, E. Charlaix, S. Ciliberto, and J. Crassous, Nature **396**, 735 (1998).

[3] T.-D. Li and E. Riedo, Phys. Rev. Lett. **100**, 106102 (2008).

[4] S. H. Khan, G. Matei, S. Patil, and P. M. Hoffmann, Phys. Rev. Lett. **105**, 106101 (2010).

[5] R. Szoszkiewicz and E. Riedo, Phys. Rev. Lett. **95**, 135502 (2005).

[6] C. Greiner *et al.*, Nano Lett. **10**, 4640 (2010).

[7] U. Raviv, P. Laurat, and J. Klein, Nature **413**, 51 (2001).

[8] Y. Zhu and S. Granick, Phys. Rev. Lett. **87**, 096104 (2001).

[9] U. Raviv, S. Perkin, P. Laurat, and J. Klein, Langmuir **20**, 5322 (2004).

[10] M. Antognozzi, A. D. L. Humphris, and M. J. Miles, Appl. Phys. Lett. **78**, 300 (2001).

[11] S. Jeffery *et al.*, Phys. Rev. B **70**, 054114 (2004).

[12] N. E. Levinger, Science **298**, 1722 (2002).

[13] I. R. Piletic *et al.*, J. Phys. Chem. A **110**, 4985 (2006).

[14] H.-S. Tan *et al.*, Phys. Rev. Lett. **94**, 057405 (2005).

[15] D. E. Moilanen, N. E. Levinger, D. B. Spry, and M. D. Fayer, J. Am. Chem. Soc. **129**, 14311 (2007).

[16] H.-S. Tan, I. R. Piletic, and M. D. Fayer, J. Chem. Phys. **122**, 174501 (2005).

[17] M. R. Harpham, B. M. Ladanyi, N. E. Levinger, and K. W. Herwig, J. Chem. Phys. **121**, 7855 (2004).

[18] J. Grobelny, N. Pradeep, D.-I. Kim, and Z. C. Ying, Appl. Phys. Lett. **88**, 091906 (2006).

[19] O. Noel, P.-E. Mazeran, and H. Nasrallah, Phys. Rev. Lett. **108**, 015503 (2012).

[20] R. D. Piner *et al.*, Science **283**, 661 (1999).

[21] H. Choe *et al.*, Phys. Rev. Lett. **95**, 187801 (2005).

[22] L. Sirghi, R. Szoszkiewicz, and E. Riedo, Langmuir **22**, 1093 (2006).

[23] M. Lee, B. Sung, N. Hashemi, and W. Jhe, Faraday Discuss. **141**, 415 (2009).

[24] B. Sung *et al.*, Appl. Phys. Lett. **103**, 213107 (2013).

[25] *Noncontact Atomic Force Microscopy Vol. 2*, edited by S. Morita, F. J. Giessibl, and R. Wiesendanger (Springer-Verlag, Berlin, 2009), Chap. 6.

[26] M. M. Kohonen and H. K. Christenson, Langmuir **16**, 7285 (2000).

[27] T. E. Balmer, H. K. Christenson, N. D. Spencer, and M. Heuberger, Langmuir **24**, 1566 (2008).

[28] J. Kim, B. Sung, B. I. Kim, and W. Jhe, J. Appl. Phys. **114**, 054302 (2013).

[29] H. Kim, B. Smit, and J. Jang, J. Phys. Chem. C **116**, 21923 (2012).

[30] C. D. Willett, M. J. Adams, S. A. Johnson, and J. P. K. Seville, Langmuir **16**, 9396 (2000).

[31] Y. Men, X. Zhang, and W. Wang, J. Chem. Phys. **131**, 184702 (2009).

[32] S. An *et al.*, Appl. Phys. Lett. **101**, 053114 (2012).

[33] J. N. Israelachvili, *Intermolecular and Surface Forces*, 3rd ed. (Academic Press, Amsterdam, 2011).

[34] F. Caupin, E. Herbert, S. Balibar, and M. W. Cole, Chem. Phys. Lett. **463**, 283 (2008).

[35] R. Lakes, *Viscoelastic Materials* (Cambridge University Press, New York, 2009).

[36] R. Proksch and D. G. Yablon, Appl. Phys. Lett. **100**, 073106 (2012).

[37] S. Patil, G. Matei, A. Oral, and P. M. Hoffmann, Langmuir **22**, 6485 (2006).

[38] D. C. Hurley *et al.*, Macromolecules **46**, 9396 (2013).

[39] K. B. Jinesh and J. W. M. Frenken, Phys. Rev. Lett. **96**, 166103 (2006).

[40] B. Kim *et al.*, Phys. Rev. Lett. **111**, 246102 (2013).

[41] A. Verdaguer, G. M. Sacha, H. Bluhm, and M. Salmeron, Chem. Rev. **106**, 1478 (2006).

[42] F. Restagno, L. Bocquet, and T. Biben, Phys. Rev. Lett. **84**, 2433 (2000).

[43] S. N. T. Ishiyama *et al.*, J. Am. Chem. Soc. **133**, 16875 (2011).

[44] T. Ishiyama and A. Morita, J. Phys. Chem. C **113**, 16299 (2009).

Chapter 6

Time-resolved dynamic force spectroscopy and its applications

6.1 Introduction

In this chapter, the time-resolved dynamic force spectroscopy technique for studies of temporally-changing mechanical properties of nanomaterials and its applications are introduced. In particular, experimental evidence is presented that controlling the tip-sample distance affects the effective temperature in the formation of the nanometric water column. It is also observed that the time constant of growth of the nanometric water column is up to several seconds, thus it takes several tens of seconds to reach a steady state. Additionally, the method to measure and compensate the effect of thermal drift during such a long time measurement to observe the molecular transport is also addressed.

6.2 The effect of approach rate on the formation of the nanometric water column

The nanometric water column plays a significant role in adhesion and friction, the formation of the water column has been extensively investigated. [1–4] In particular, Bocquet *et al.* showed that the water capillary condensate give rise to ageing phenomenon in granular media. [1] In addition, it was established a theoretical foundation for the nucleation and metastability in capillary condensation, [2] and it was demonstrated that capillary condensation is a thermally-activated process by friction force measurements. [3] Griener *et al.* illustrated that friction can be handled by controlling the capillary condensation via local heating. [4]

Recently, it was demonstrated that the activation time in the formation of the nanometric water column is directly measured and the formation process of the nanometric water column follows Poisson process by using non-contact atomic force microscopy. [5] The formation rate was shown to be extracted from the histogram of the activation time for a tip-sample distance. It was also exhibited that the formation rate increases as the tip-sample distance gets smaller. In addition, the formation of the nanometric water column when the tip is not contact with the sample was also thermally-activated process, which is consistent with the previous experiment using friction force microscope. [3]

It was also observed that the formation rate is enhanced when the approach rate (or approach speed) gets faster. [6] However, the effect of the ap-

proach rate (or approach speed) on the formation rate has not been understood even qualitatively yet. In this section, the experimental method is briefly introduced and how the approach rate affects the formation of the nanometric water column is discussed.

To monitor temporal changes of the signal due to the dynamics of the water column, a novel technique called time-resolved dynamic force spectroscopy (TRDFS) is introduced. TRDFS records all the data as a function of not only tip-sample distance but also time, with the help of large stiffness of quartz tuning fork. In TRDFS technique, measurements at every τ_{m} is followed by controlling the distance at every staying period τ_{s}. A new setup based on field programmable gate array is installed, and programs to operate the setup is developed for measurements (see Appendix D).

Figure 6.1 shows the amplitude and phase signal using TRDFS technique at the moment of the formation of the nanometric water column between the tip and sample. The measurement interval τ_{m} is 20 ms and the staying period τ_{s} is 2 s in Fig. 6.1. In addition, the tip-sample distance is controlled at an interval Δ of 0.15 nm. It is clearly observed that abrupt decrease in amplitude and increase in phase when the distance between the tip and sample is kept fixed. The change in amplitude and phase indicates the formation of the nanometric water column. [7, 8] Interestingly, an incubation delay before the formation occurs, which is called activation time t_{A}, is observed. It is also found in other activation processes such as noise-activated switching [9] and crystallization of glassy solid. [10]

It was found that the activation time t_{A} has an exponential distribution

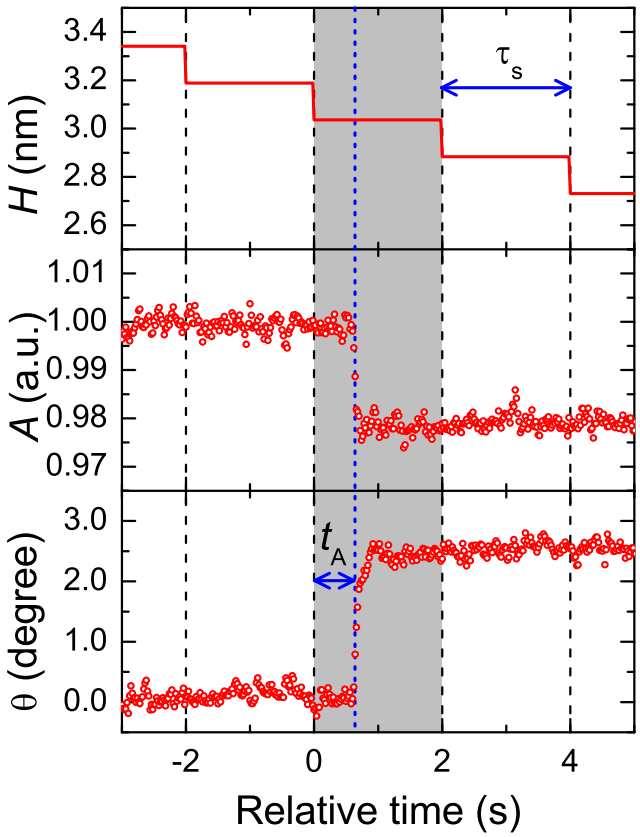

Figure 6.1: The tip-sample distance H, amplitude A and phase θ around the formation of nanometric water column are depicted as a function of time. The staying period and the activation time of the formation are represented by τ_{s} and t_{A}, respectively. The drop of amplitude and the rise of phase in the grayed area indicates the formation of the nanometric water column. Reproduced from Sung *et al.* [5]

for each tip-sample distance at which the formation occurs H_c obtained from hundreds of approaches. [5] The exponential distribution of the activation time indicates that the formation of the nanometric water column obeys the Poisson statistics, which is represented by the formation rate Γ given by

$$p(t) = p(0)\exp(-\Gamma \cdot t) \tag{6.1}$$

where $p(t)$ is the probability that the formation of the water column does not happen until the time t. In addition, the formation rate follows the Arrhenius law given by

$$\Gamma = \Gamma_0 \exp\left(-\frac{\Delta\Omega}{k_B T}\right) \tag{6.2}$$

where $\Delta\Omega$ represents the energy barrier of the formation, Γ_0 is the formation rate when there is no energy barrier, k_B is the Boltzmann constant and T is the absolute temperature.

Figure 6.2(a) shows the formation rate Γ as a function of the approach rate f_{app} for each tip-sample distance. It is clearly observed that the formation rate increases as the approach rate is raised. It was suggested that the motion-induced momentum applied on the prewetted layer of the sample may enhance the formation. [6]

A deeper understanding is given by combining the effects of both the approach rate and the tip-sample distance on the formation rate. The energy barrier is the difference between the cost of surface energy and the gain of volume energy of the nanometric water column. [2] For very small water column, the surface energy is dominant to the volume energy in the energy barrier. Since

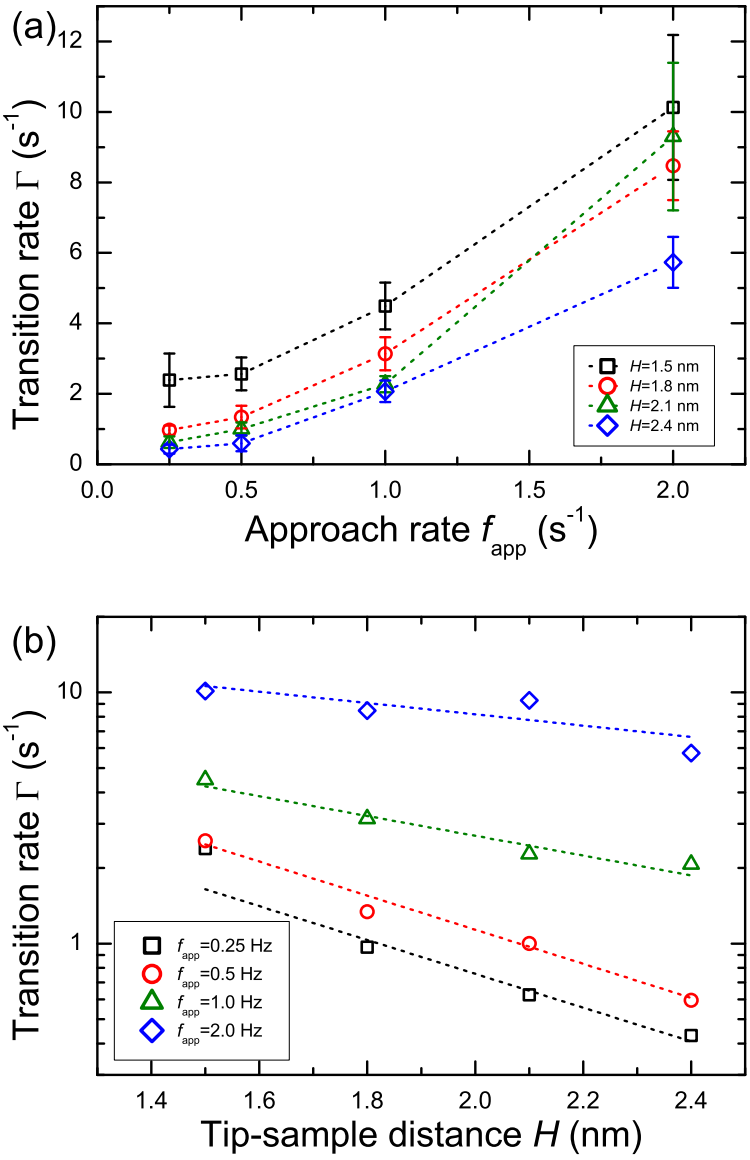

Figure 6.2: (a) The formation rate Γ is depicted as a function of the approach rate f_{app}. (b) The semi-log plot of the formation rate Γ is presented as a function of the tip-sample distance H. Reproduced from Figure 4.8 in Sung's Ph.D dissertation. [6]

the surface energy is proportional to the length of the water column, [2] the energy barrier can be assumed to be $\Delta\Omega \approx \beta H$. Then the formation rate Γ is now given by

$$\Gamma = \Gamma_0 \exp\left(-\frac{\Delta\Omega}{k_{\mathrm{B}}T}\right) \approx \Gamma_0 \exp\left(-\frac{\beta H}{k_{\mathrm{B}}T}\right) \tag{6.3}$$

where β is a proportionality constant. Taking a logarithm on both sides of Eq. (6.3) leads to

$$\ln\Gamma \approx \ln\Gamma_0 - \frac{\beta}{k_{\mathrm{B}}T} \cdot H \ , \tag{6.4}$$

The formation rate as a function of tip-sample distance H is depicted in Fig. 6.2(b). The measured values for each approach rate fit well with a linear curve, which indicates the assumption $\Delta\Omega \approx \beta H$ is supported. The slope of the linear curve is $\beta/k_{\mathrm{B}}T$ from Eq. (6.4). Interestingly, the slope of the linear curve decreases as the approach rate increases. It implies that T in Eq. (6.4) can be replaced by the effective temperature T_{eff}, which increases as f_{app} is enhanced because the energy barrier is independent of f_{app}.

Figure 6.3 depicts the effective temperature divided by a constant $T_{\mathrm{eff},0.25}$ versus the approach rate. The constant $T_{\mathrm{eff},0.25}$ is the effective temperature when $f_{\mathrm{app}} = 0.25$ Hz. In Fig. 6.3, it is clearly observed that the effective temperature increases as f_{app} enhances when f_{app} is larger than 0.5 Hz. The effective temperature may be divided into two regions, one is slow approach region ($f_{\mathrm{app}} < 0.5$ Hz in Fig. 6.3) and the other is fast approach region ($f_{\mathrm{app}} > 0.5$ Hz). In slow approach region, the formation of the nanometric water column might be thermally-activated, thus the formation rate is independent of the approach

rate. The formation rate rises as the approach rate increases in fast approach region, which may indicate the formation is attributed to the motion of the tip and sample. The behavior in the fast approach region and the crossover from thermally-activated to motion-induced formation of the nanometric water column with a larger number of approach rate would be interesting studies.

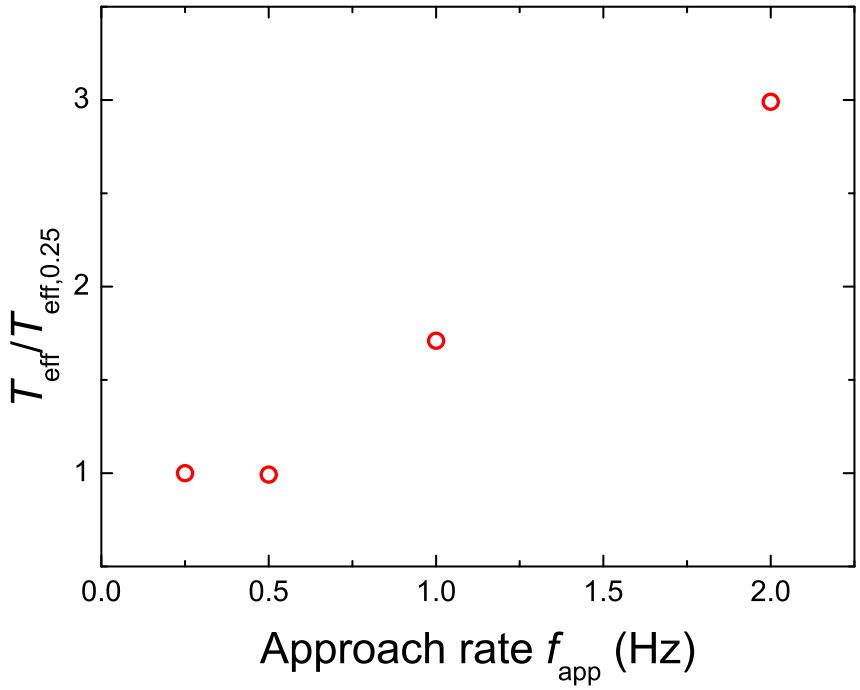

Figure 6.3: The effective temperature T_{eff} normalized by $T_{\mathrm{eff},0.25}$ when the approach rate is 0.25 Hz as a function of the approach rate f_{app} is represented.

6.3 Observation of growth of the nanometric water column

The interaction between solid surfaces in nanoscale is of interest due to its importance on micro- and nanoscale systems. The water formed between hydrophilic surfaces plays a crucial role in adhesion and friction. Understanding the transport mechanism of water molecules in nanoscale is important to the dynamic behavior of water confined in porous media as well as the growth of water droplet in atmosphere.

The growth of water capillary condensate and its transport mechanisms have been investigated in the literatures. [11–13] It was reported that the observed rate of condensation of water in high vapor pressure is much lower than values calculated from the model based on Langmuir's theory by using surface force apparatus (SFA). [11] The growth of the water meniscus as the contact time increases was observed via pull-off force using contact AFM. [13]

However, a real-time measurement of growth has not performed yet in ambient conditions. In this section, the an *in-situ* measurement of the growth process of the nanometric water column is demonstrated by using dynamic force spectroscopy. The time constant of the growth is found to be up to several seconds. It is suggested that the slow growth may be attributed to the transport of water molecules via flow of surface water.

Figure 6.4 shows an approach-retraction curve of interaction stiffness when the nanometric water column is formed. The hysteresis during the ap-

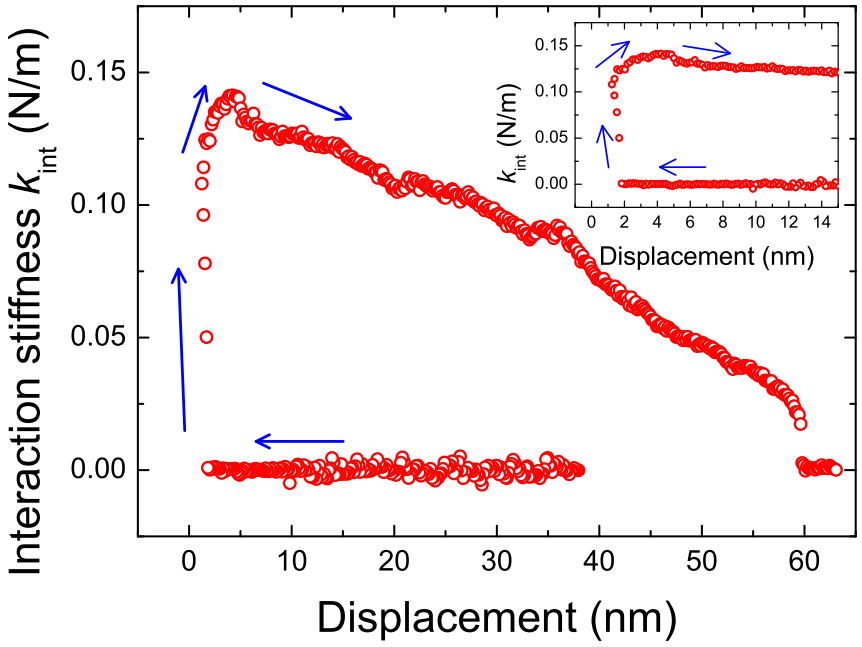

Figure 6.4: The interaction stiffness due to the water column with rupture distance of roughly 60 nm as a function of displacement is presented. The interaction stiffness increases during retraction of early stage. The inset shows a magnified plot near the formation of the water column.

proach and retraction indicates the formation of the water column. The striking result in Fig. 6.4 is that the interaction stiffness increases during retraction in the early stage whereas it decreases during retraction since then. It is also observed in previous studies, especially for a large water column. [7,14] The water column is elongated and becomes narrower during retraction, thus the interaction stiffness as well as the damping coefficient decrease in general. In addition, the formation of the water column gets difficult and the rupture becomes easy as the tip-sample distance increases. [15]

The rise during retraction may be attributed to the growth of the nanometric water column. Since this behavior is often observed for the water column of large volume, the time takes to form a large water column consists of many water molecules, accompanied by the transport of water molecule for growth. It is worth noting that the response of QTF is fast enough to follow the change of the signal and reach a steady state because the staying period τ_s is 500 ms which is very longer than the response time of QTF, about 50 ms.

Figure 6.5 shows the interaction stiffness as a function of tip-sample distance to observe its temporal behavior during growth. The left and right insets of Fig. 6.5 represents tip-sample distance and interaction stiffness as time passes. In particular, the right inset of Fig. 6.5 shows the temporal changes of interaction stiffness with the tip-sample distance fixed. The time evolution of the mechanical response was recorded with the tip-sample distance H kept fixed when a water column is formed during approach, at $H = 1.5$ nm in Fig. 6.5. After the temporal response was recorded, the sample further come close to the tip to detect the tip-sample contact, and then it retracts. In the right inset of Fig. 6.5, it is clearly demonstrated that the the growth of the nanometric water column takes up to 15 seconds.

The interaction stiffness in the right inset of 6.5 shows a relaxation-like behavior, which is qualitatively consistent with the behavior of pull-off force as a function of contact time. [13] The exponential fit in the right inset of 6.5 has the time constant of 4.6 seconds, much longer compared with the previous study. [13] Two transport mechanisms of water molecules in growth were suggested: (i)

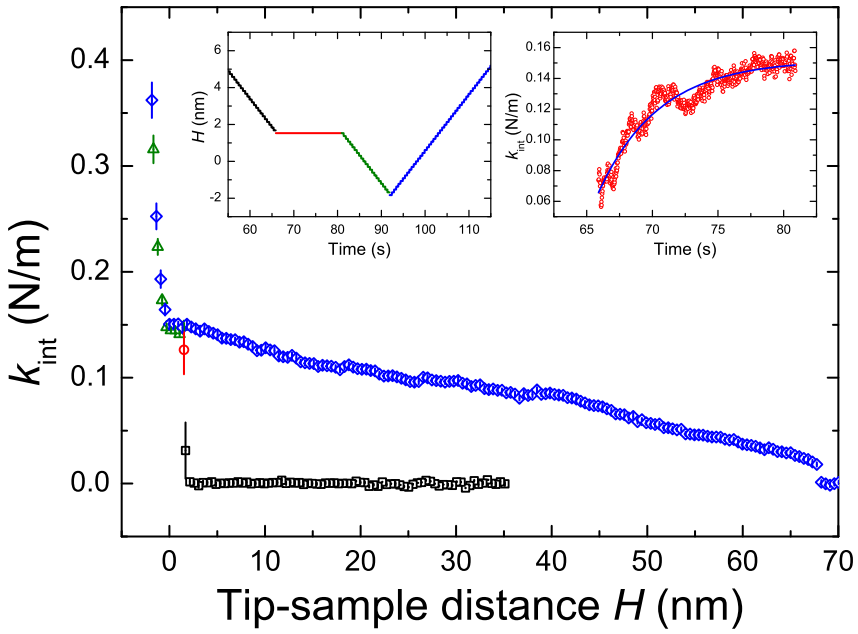

Figure 6.5: The interaction stiffness as a function of tip-sample distance is depicted. The left inset shows the tip-sample distance as time passes. Squares (black), circles (red), triangles (green) and diamonds (blue) represent the signal during approach until the water column forms, during growth, during further approach to determine the tip-sample contact, and during retraction, respectively. Each color of line in the left inset corresponds to points of same color in the main figure. The right inset shows the change of the interaction process as a function of time during growth. The solid (blue) curve denotes its exponential fit.

Knudsen diffusion of water molecules in the nanoscopic gap and (ii) adsorption on the surface region and flow of the surface water. [13] Since the growth of the nanometric water column when the tip is not contact with the sample, the Knudsen diffusion with the gap is expected to be faster than the diffusion in contact because the Knudsen diffusion coefficient is proportional to the size of the pore. In addition, the flow of the surface water becomes slow as the nanogap between the tip and sample due to reduction of the radial gradient of disjoining pressure. Thus, the flow of the surface water may be also responsible for the transport of water molecules in the growth process in the presence of nanoscopic gap.

6.4 Compensation of thermal drift in dynamic force spectroscopy

Atomic force microscope has been widely employed for imaging the solid surface in atomic resolution and detecting the interaction forces between the tip and sample. Recently, the forces exerted on individual adsorbed atoms or molecules by using an atomic force microscope for manipulation of individual atoms and molcules. [16] One of the technical difficulty for realization of the manipulation in room temperature is thermal drift which distorts the image of surface and force spectroscopy whereas it is negligible when the measurement is carried out in low temperature. [17]

The time-resolved dynamic force spectroscopy technique requires rela-

tively long-time measurement at each tip-sample distance. In addition, experiments are frequently performed in ambient conditions to observe the formation and growth of the nanometric water column. It was reported that three-dimensional thermal drift was compensated by using feedforward and atom tracking feedback techniques in ultrahigh vacuum at room temperature. [17]

However, there is still lack of detection and compensation technique of thermal drift in force spectroscopy in ambient conditions. In ambient conditions, the formation of the water meniscus between two hydrophilic surfaces is allowed, which hinders reproducible data acquisition in force spectroscopy due to its kinetic behavior such as growth and evaporation. In this section, a simple but robust method to determine and compensate the effect of thermal drift in force spectroscopy is suggested. It is demonstrated that the thermal drift is extracted and compensated by successive approach-retraction cycles. With the help of this technique, the reproducibility of force spectroscopy is assured even in the presence of capillary condensation in ambient conditions.

Figure 6.6(a) shows the amplitude and phase signals measured during three consecutive approach-retractions. The amplitude and phase signals were measured and recorded every $\tau_{\mathrm{m}} = 10$ ms as a function of the tip-sample distance. The sample moves at a unit displacement step of $\Delta = 0.15$ nm to control the distance and stays for $\tau_{\mathrm{z}} = 500$ ms at each distance. Thus, the speed of approach or retraction was 300 pm/s, which is much slower than that in previous studies. [8,12] The average of those temporal raw data points was also obtained at each tip-sample distance. The hysteresis during an approach-retraction cycle

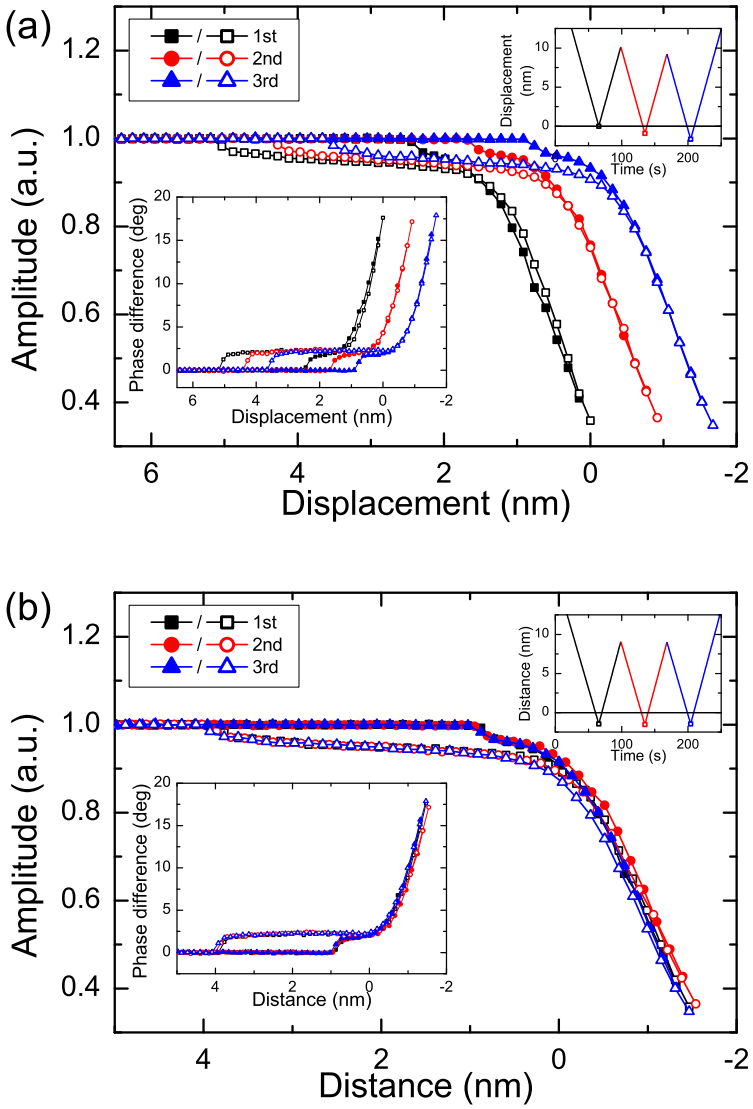

Figure 6.6: The measured amplitude during successive approaches (retractions) is represented by solid (open) point, and the phase signal versus the displacement is also presented in the inset at the bottom. (a) The approach-retraction curves are shifted by thermal drift. The displacement as a function of time is drawn in the inset at the top. (b) The amplitude and phase signals after compensation of thermal drift shows the curves with no drift.

in Fig. 6.6(b) is evidence of a water nanomeniscus. [7, 8, 12] With the help of high stiffness of the QTF, it is possible to manipulate the nanomeniscus without mechanical instability of the tip during approach-retraction cycles. Each retraction started at the position where the oscillation amplitude was smaller than 50% at free oscillation. The relative displacement with the first retraction point defined as zero is positive (negative) when the tip moves away from (toward) the sample as shown in Fig. 6.6(a).

Strikingly, the returning points of three successive approach-retraction cycles approached negative, which indicates the tip-sample distance becomes slightly increased because the tip approaches the sample closer than the previous cycle due to thermal drift. The thermal drift, usually due to local change of temperature, was assumed to have a constant speed v_{drift}. This is also observed in studies for imaging with atomic resolution in ultrahigh vacuum at room temperature. [17] The drift speed in the measurement of 6.6(a) was 12 pm/s, which was extracted from the temporal drift of the retraction points. The compensated position along the z-axis (displacement that controls the tip-sample distance) z' is defined by

$$z' = z - v_{\text{drift}} t \tag{6.5}$$

where t and z are the time and piezo displacement of the original measurement, respectively. The amplitude and phase signals that compensated the thermal drift are depicted in Fig. 6.6(b). Interestingly, they are overlapped onto one approach-retraction cycle, which shows their reproducibility. This repetitive approach-retraction method makes sure that the measurement of the mechani-

cal properties of the water nanomeniscus is reproducible and it enables one to extract and compensate the effect of thermal drift, especially for slow approach or retraction speed.

In summary, the method for compensation of the effect of thermal drift has been presented, which suggests that the drift speed of thermal drift can be acquired from successive approach-retraction cycles with an assumption of constant speed. It has been demonstrated that the effect of the thermal drift is compensated by the repetitive approach-retraction cycle, which makes certain of the reproducibility of force spectroscopy. This technique is expected to be used for precise measurement of the tip-sample distance using AFM in ambient conditions.

References

[1] L. Bocquet, E. Charlaix, S. Ciliberto, and J. Crassous, Nature **396**, 735 (1998).

[2] F. Restagno, L. Bocquet, and T. Biben, Phys. Rev. Lett. **84**, 2433 (2000).

[3] R. Szoszkiewicz and E. Riedo, Phys. Rev. Lett. **95**, 135502 (2005).

[4] C. Greiner *et al.*, Nano Lett. **10**, 4640 (2010).

[5] B. Sung *et al.*, Appl. Phys. Lett. **103**, 213107 (2013).

[6] B. Sung, Ph.D. thesis, Seoul National University, Seoul, Republic of Korea, 2013.

[7] H. Choe *et al.*, Phys. Rev. Lett. **95**, 187801 (2005).

[8] M. Lee, B. Sung, N. Hashemi, and W. Jhe, Faraday Discuss. **141**, 415 (2009).

[9] C. Stambaugh and H. B. Chan, Phys. Rev. B **73**, 172302 (2006).

[10] B.-S. Lee *et al.*, Science **326**, 980 (2009).

[11] M. M. Kohonen, N. Maeda, and H. K. Christenson, Phys. Rev. Lett. **82**, 4667 (1999).

[12] L. Sirghi, R. Szoszkiewicz, and E. Riedo, Langmuir **22**, 1093 (2006).

[13] L. Sirghi, Langmuir **28**, 2558 (2012).

[14] S. An *et al.*, Curr. Appl. Phys. **13**, 1899 (2013).

[15] Y. Men, X. Zhang, and W. Wang, J. Chem. Phys. **131**, 184702 (2009).

[16] M. Ternes *et al.*, Science **319**, 1066 (2008).

[17] M. Abe *et al.*, Appl. Phys. Lett. **90**, 203103 (2007).

Chapter 7

Summary and Perspectives

In this dissertation, the mechanical properties of a nanometric water column was investigated by using atomic force microscopy employing a quartz tuning fork as a force sensor. In Chapter 3, the effective stiffness of qPlus sensor and QTF was measured and then compared with the cantilever beam theory, which has been widely used to estimate the stiffness for quantitative measurement of the interaction in nanoscale using QTF as a force sensor. Comparing with the stiffness and the resonance frequency in the measurements, it was found that those calculated based on the beam theory are considerably overestimated. For consistent analysis of experimental and theoretical results, the formula to calculate the stiffness of qPlus sensor or QTF was presented based on the resonance frequency. It was also demonstrated that the effective stiffness of QTF is twice that of qPlus sensor, which agrees with the recently suggested model. From this study, quantitative measurements of interaction force at the nanoscale with

QTF is allowed in scanning probe microscopy.

In Chapter 4, control of force sensitivity in Q-controlled amplitude modulation (AM) atomic force microscopy (AFM) based on the high-Q quartz tuning fork was presented. It was found that the phase noise is identical to the amplitude noise divided by oscillation amplitude in AM-AFM. In particular, it was observed that while Q-control does not compromise the signal-to-noise ratio, it enhances the detection sensitivity because the minimum detectable force gradient is inversely proportional to the effective quality factor for large bandwidths, due to reduction of frequency noise. Q-control in AM-AFM is expected to be a useful technique for enhancement of the force sensitivity with increased Q or improvement of the scanning speed with decreased Q.

In Chapter 5, the experimental measurements of the mechanical properties of the nanometric water column as a function of the tip-sample distance was presented using dynamic force spectroscopy technique. It was found that the mechanical relaxation time of the water nanobridge increases with its elongation. In addition, the volume of the nanobridge is not relevant to the mechanical relaxation time. The findings of this study suggest that the mechanical relaxation time does not depend on the size of the water nanobridge but does depend on its interfacial area.

In Chapter 6, the time-resolved dynamic force spectroscopy technique and its applications were introduced. In the formation of the nanometric water column, experimental evidence that periodic movement of the tip and sample is responsible for an increase of effective temperature was presented via analyz-

ing the formation rate as a function of tip-sample distance and approach rate. The time constant of the growth of the water column was up to several seconds, which is longer than the result by using friction force microscopy. It was demonstrated that the effect of thermal drift in force spectroscopy is determined and compensated by successive approach-retraction cycles.

This research has thrown up many questions in need of further investigation. One of the most crucial point is that the mechanical properties including the interaction stiffness, damping coefficient and mechanical relaxation time of the nanometric water column depends on the driving frequency. It is a significant factor in understanding its mechanical properties. Since the properties of water at the air/water interface may be affected by the relative humidity, the dependence of the mechanical relaxation time on the relative humidity would be also an interesting future study. In addition, the current experimental investigation of the formation of the water column had studied by insufficient number of approach rate to observe the crossover behavior and it is lack of theory. A systematic data acquisition and theoretical investigations may consolidate the increase of the effective temperature. Additionally, it would be interesting to investigate the Poisson's ratio of the nanometric water column.

Appendices

Appendix A

Calibration of the experimental setup

Figure A.1 shows the circuit of the amplitude-modulation (AM) AFM based on a QTF. The function generator is to apply constant amplitude and frequency to operate the QTF. The voltage divider which consists of three resistors is employed to get much smaller driving amplitudes for small oscillation of the force sensor. The oscillation of the quartz tuning fork is expressed by the current flowing through the circuit, which is converted and amplified into the voltage by the preamplifier. The lock-in amplifier plays a role in extracting the amplitude and phase information from the amplified voltage.

Figure A.2 shows the gain as a function of driving frequency and various driving amplitudes when Agilent 33220A as a function generator and Stanford Research Systems SR830 as a lock-in amplifier are employed. The frequency

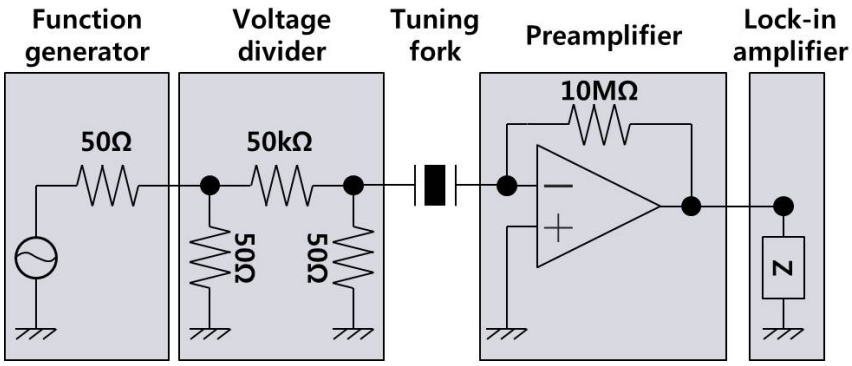

Figure A.1: Schematics of the amplitude-modulation atomic force microscope based on a quartz tuning fork is depicted.

range was set from 20 to 100 kHz. As shown in Fig. A.2, the error of the gain is less than 0.6% in the range of frequency.

It is worth noting that a resistor with resistance of 50 Ω is connected to the cable between the function generator and the lock-amplifier in parallel for impedance matching during the measurement for Fig. A.2. If the resistor is absent, the voltage read at the lock-in amplifier is twice as much as that applied by the function generator due to its reflected wave. It is because the impedance of the function generator is set to 50 Ω and that of the lock-in amplifier is set to 10 MΩ.

To get much smaller driving amplitudes for small oscillation of the force sensor, a voltage divider with three resistors was made. To set its gain to be 1/1000, 50 kΩ and 50 Ω and 50 Ω was employed for impedance matching as shown in Fig. A.1.

Since typical QTFs have the motional resistance in the order of several

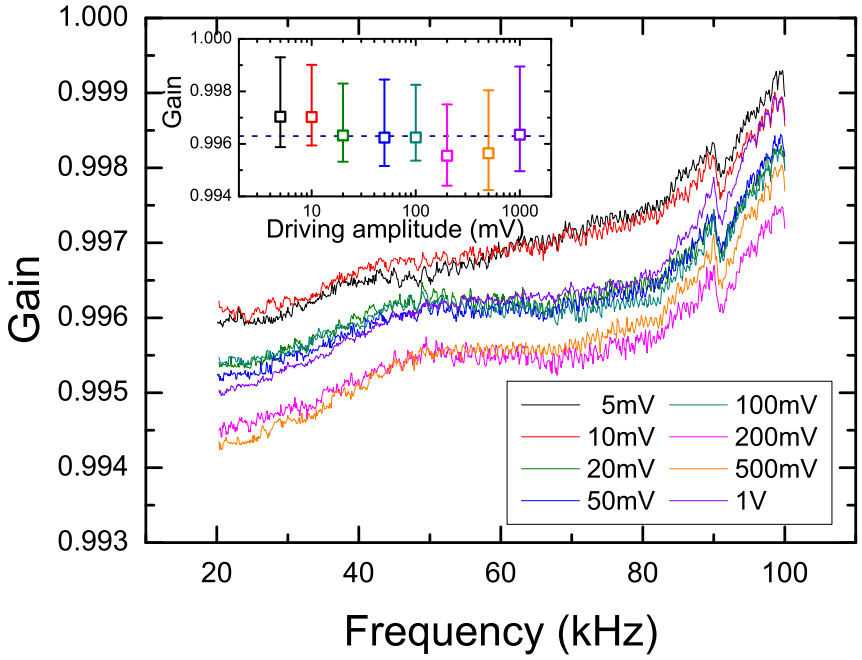

Figure A.2: The gain of lock-in amplifier as a function of driving frequency is presented. The inset shows the average of the gain for each driving amplitude. The error bars in the inset denote the minimum and maximum values of the gain. Dotted line represents the average of measured gains for all driving amplitudes.

tens of kiloohms,* or $R = 1/(Q\omega_0 C)$, the impedance of each component is designed to increase from the function generator to the lock-in amplifier.

As shown in Fig. A.3, the average gain of the combination of the function generator, voltage divider and lock-in amplifier is found to be 1.021×10^{-3}. Its standard deviation is 3.97×10^{-6}. The value of the gain is employed to convert the electric voltage signal to mechanical amplitude signal. For example, when the driving voltage of the function generator is $V_{\rm d} = 200$ mV and the gain of

*Seiko Epson Corporation, "kHz range crystal unit", Retrieved November 7, 2013 from *http://www.epsondevice.com/docs/qd/en/DownloadServlet?id=ID000661*

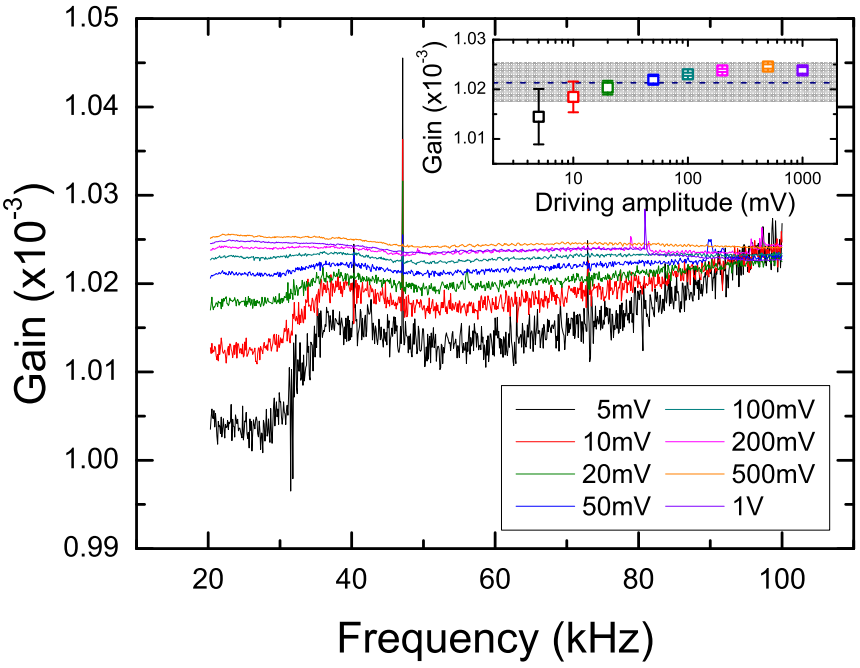

Figure A.3: Gain of voltage divider as a function of driving freqency is depicted. The inset shows the average of the gain for each driving amplitude. The error bars in the inset denote the minimum and maximum values of the gain. Dotted line and shaded region represent the average and its standard deviation of measured gains for all driving amplitude, respectively.

the voltage divider is $G_{\mathrm{VD}} = 1.021 \times 10^{-3}$, the quartz tuning fork is considered to be driven by $V_{\mathrm{d}} \cdot G_{\mathrm{VD}} = 0.204$ mV during the analysis.

On the other hand, the frequency response of LF356N is not linear, as shown in A.4. In particular, the I-V gain of the preamplifier introducing LF356N as the operational amplifier is dependent upon the capacitance of the QTF, which results in difficulty using various kinds of QTF have different capacitances.

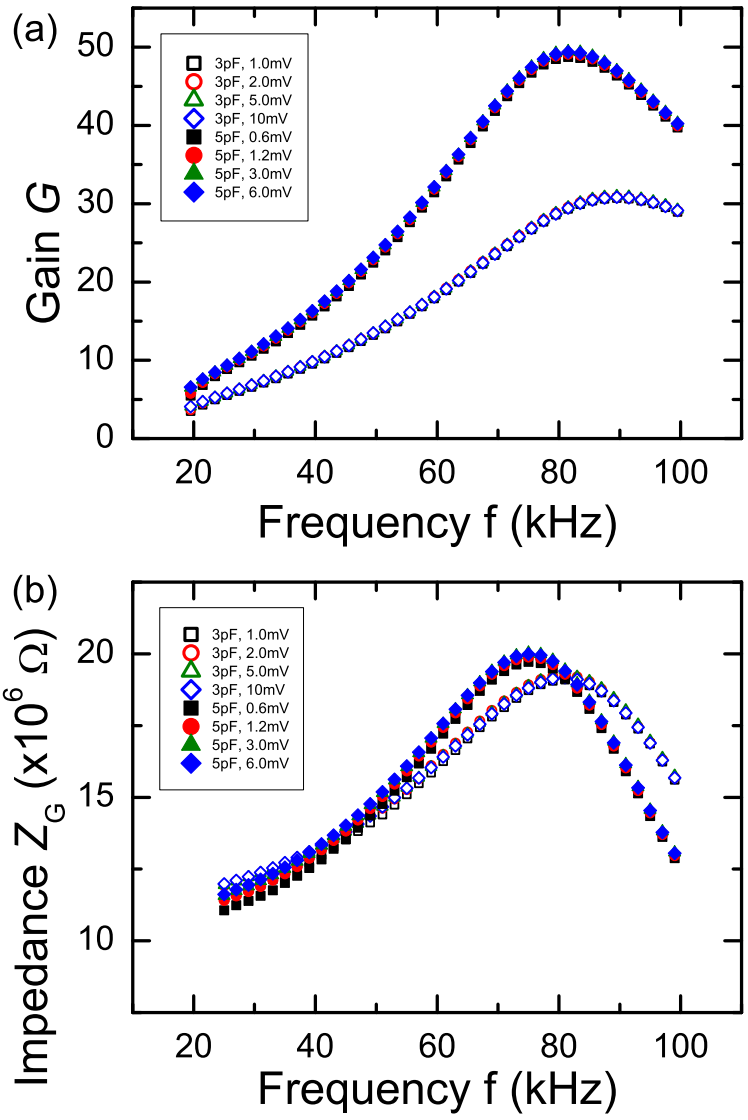

Figure A.4: (a) Gain and (b) impedance of preamplifier using LF356N as a operational amplifier are depicted as a function of driving frequency

Appendix B

Analysis of response of quartz tuning fork to interaction forces

B.1 Geometric interpretation of electrically-driven quartz tuning fork

The amplitude A_{m} and phase θ_{m} of a driven damped harmonic oscillator of spring constant k_0, angular resonance frequency ω_0 and quality factor Q are respectively given by

$$A_{\mathrm{m}}(\omega) = \frac{F_0/k_0}{\left[\left(1-\omega^2/\omega_0^2\right)^2 + \left(\omega/\omega_0 Q\right)^2\right]^{1/2}} , \tag{B.1}$$

$$\theta_{\mathrm{m}}(\omega) = -\tan^{-1}\left(\frac{\omega^2-\omega_0^2}{\omega_0\omega/Q}\right) , \tag{B.2}$$

where ω is the driving frequency and θ_{m} is the phase difference with respect to the phase at the resonance frequency. Let $x_{\mathrm{m}}(\omega) = A_{\mathrm{m}} \cos\theta_{\mathrm{m}}$ and $y_{\mathrm{m}}(\omega) = A_{\mathrm{m}} \sin\theta_{\mathrm{m}}$, then $x_{\mathrm{m}}^2 + y_{\mathrm{m}}^2 = A_{\mathrm{m}}^2$. In addition, $x_{\mathrm{m}}(\omega)$ is written by

$$\begin{aligned} x_{\mathrm{m}}(\omega) &= A_{\mathrm{m}}(\omega)\cos\theta_{\mathrm{m}}(\omega) \\ &= -\frac{F_0/k_0}{\left[\left(1-\omega^2/\omega_0^2\right)^2 + \left(\omega/(Q\omega_0)\right)^2\right]^{1/2}} \frac{\omega_0\omega/Q}{\left[\left(1-\omega^2/\omega_0^2\right)^2 + \left(\omega/(Q\omega_0)\right)^2\right]^{1/2}} \\ &= \frac{\left[A_{\mathrm{m}}(\omega)\right]^2}{A_0} \end{aligned}$$

where $A_0 = QF_0/k_0$. Then $x_{\mathrm{m}}^2 + y_{\mathrm{m}}^2 = 2rx_{\mathrm{m}}$ holds, i.e.,

$$(x_{\mathrm{m}} - r)^2 + y_{\mathrm{m}}^2 = r^2 \tag{B.3}$$

where r is $r = A_0/2$.

The equation represents a circle of radius r with its center at $(r,\ 0)$, as shown in Fig. B.1(a). The point which indicates the oscillation at Fig. B.1(a) starts at the origin and rotates clockwise as the driving frequency increases. The distance of the segment between the origin and a point on the circle denotes A_{m}. In addition, the angle between the segment and the positive x-axis denotes θ_{m} as shown in Fig. B.1(b). At the resonance frequency, the point is at the intersection of the circle and the positive x-axis, which has the largest amplitude and zero phase. The distance between the points of adjacent frequencies becomes farther as the driving frequency gets closer to the resonance frequency. This analysis is always valid for resonators of which the quality factor Q is very large compared to ω/ω_0.

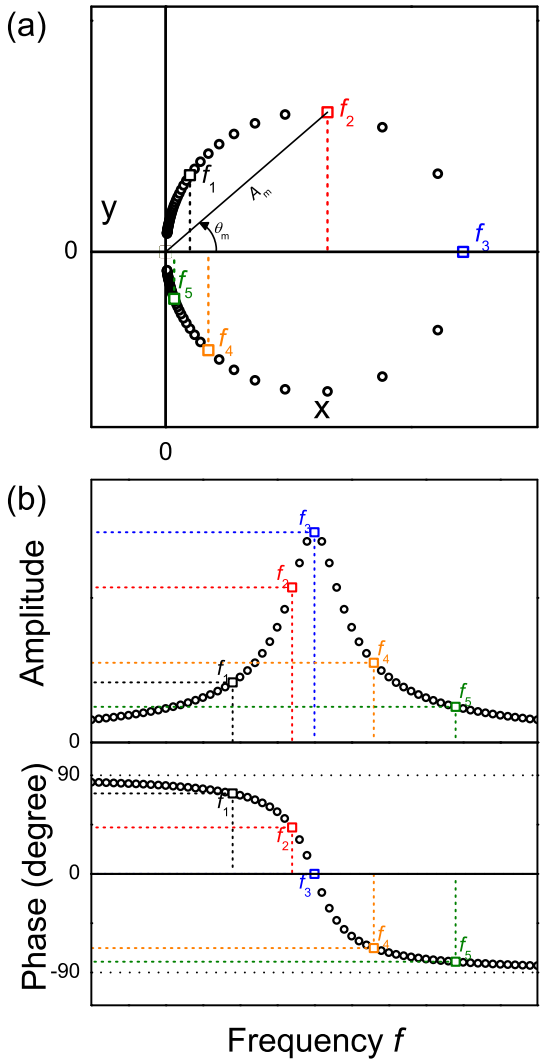

Figure B.1: (a) Geometrical interpretation of harmonic oscillator is depicted. The amplitude and phase is extracted by the point on the circle. The driving frequencies f_i gets large as the subscript i become large. (b) The amplitude and phase curve as a function of driving frequency f are represented, respectively. The amplitude and phase which correspond to the driving frequency shown in (a) are also depicted by open points.

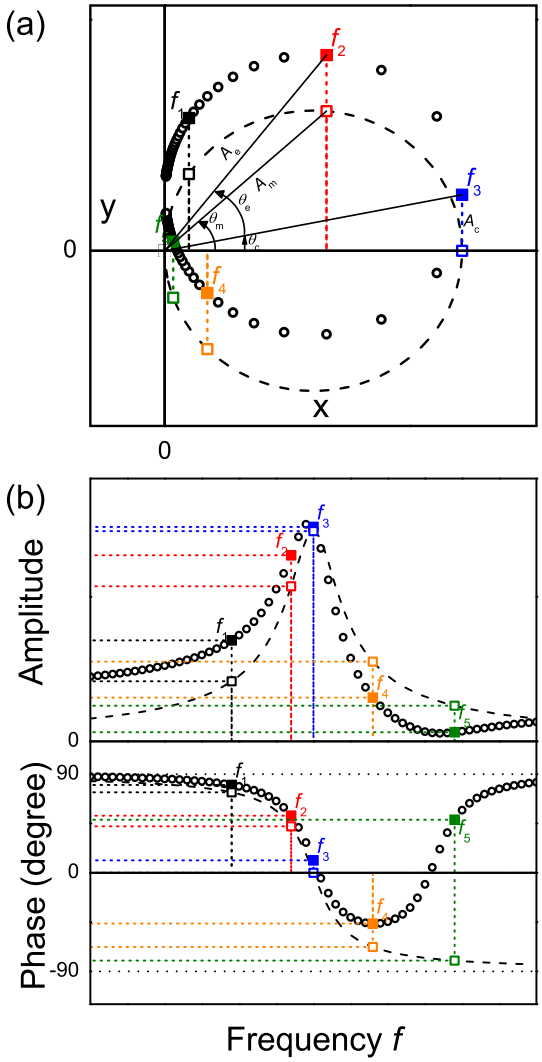

Figure B.2: (a) Geometrical interpretation of ED-QTF is depicted. The circle shown in Fig. B.1 is shifted along the y-axis as much as A_c. (b) The amplitude and phase curve as a function of driving frequency f are presented, respectively. The amplitude and phase which correspond to the driving frequency shown in (a) are also depicted by filled points. The open points are the same as those in Fig. B.1.

When a quartz tuning fork (QTF) is driven electrically, it is considered as Butterworth-van Dyke equivalent circuit (a stray capacitance connected to LRC series circuit in parallel) The stray capacitance distorts the resonance curve of QTF, which will be addressed geometrically. The signal due to the stray capacitance has a phase lead of 90 degrees over the mechanical signal at the resonance, thus the circle in Fig. B.1(a) is parallel translated as much as $A_{\rm c}$ along the y-axis as shown in Fig. B.2(a). The amplitude $A_{\rm e}$ and phase $\theta_{\rm e}$ for the electrically-driven QTF are expressed by

$$\begin{aligned} A_{\rm e} &= \left(A_{\rm m}^2 + 2A_{\rm m}A_{\rm c}\sin\theta_{\rm m} + A_{\rm c}^2\right)^{1/2} , \\ \theta_{\rm e} + \theta_0 &= \tan^{-1}\left(\frac{A_{\rm m}\sin\theta_{\rm m} + A_{\rm c}}{A_{\rm m}\cos\theta_{\rm m}}\right) , \end{aligned}$$

in terms of $A_{\rm m}$ and $\theta_{\rm m}$ by analogy with Fig. B.1. Here θ_0 is given by $\tan^{-1}(A_0/A_{\rm c})$. Figure B.2(b) shows the amplitude and phase as a function of driving frequency.

In the experiment, the resonance curve of QTF is obtained as a function of driving frequency in advance. And then $A_{\rm e}$ and $\theta_{\rm e}$ are acquired as a function of tip-sample distance to measure the interaction force exerted on the probe tip when the driving frequency is fixed to the resonance frequency in AM-AFM. To compensate the effect of stray capacitance from the measured $A_{\rm e}$ and $\theta_{\rm e}$, the formulas given below are used.

$$A_{\rm m} = \left[A_{\rm e}^2 - 2A_{\rm e}A_{\rm c}\sin(\theta_{\rm e} + \theta_0) + A_{\rm c}^2\right]^{1/2} , \tag{B.4}$$

$$\theta_{\rm m} = \tan^{-1}\left[\frac{A_{\rm e}\sin(\theta_{\rm e} + \theta_0) - A_{\rm c}}{A_{\rm e}\cos(\theta_{\rm e} + \theta_0)}\right] . \tag{B.5}$$

Figure B.3 presents typical resonance curves of an electrically-driven QTF. The parasitic capacitance distorts both the amplitude and phase as shown

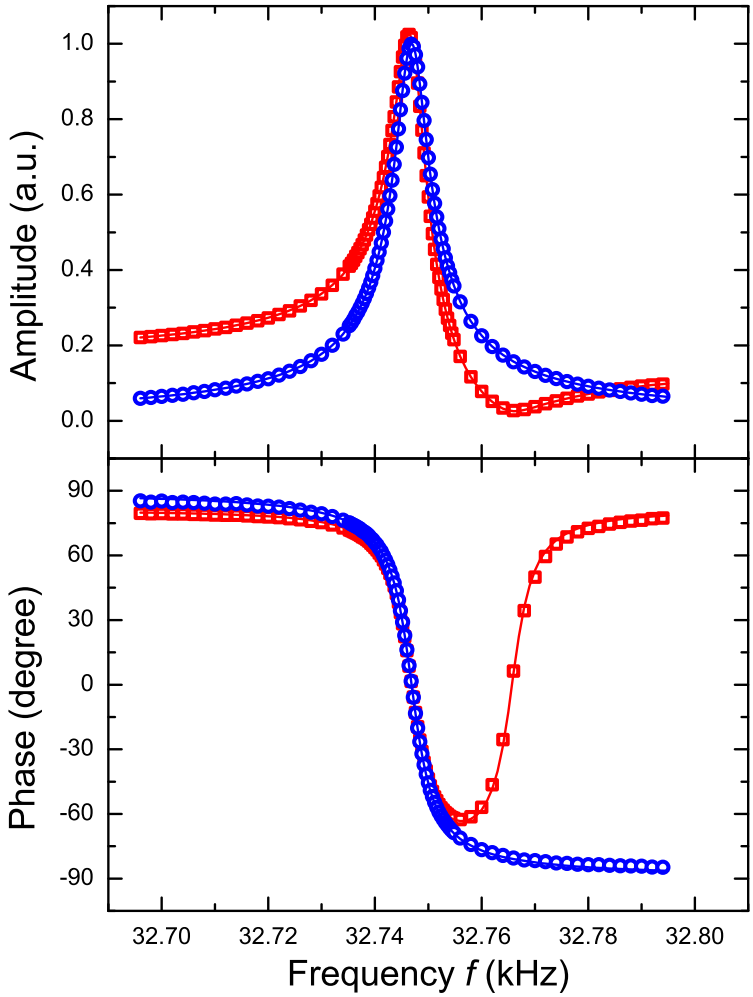

Figure B.3: Typical resonance curves of a electrically-driven quartz tuning fork is depicted. Red squares denote the amplitude and phase difference in the presence of the effect of the parasitic capacitance versus the driving frequency. Blue circles represent the amplitude and phase difference obtained from Eqs. (B.4) and (B.5). Each solid lines represents the calculated values using its optimum fitting parameters.

in Fig. B.3. It is demonstrated that Eqs. (B.4) and (B.5) well compensates the effect of the parasitic capacitance.

B.2 Equivalence of formulas for interaction stiffness and damping

According to the previous studies, [1,2] the formulas for the interaction stiffness $k_{\rm int}$ and damping coefficient $b_{\rm int}$ due to the external interaction exerted on the force sensor oscillating at the resonance frequency of ω_0 are written by

$$k_{\rm int} = k_0 \left[\frac{A_0^{(\rm r)}}{QA} \sin\phi - \left(1 - \frac{\omega^2}{\omega_0^2} \right) \right], \quad b_{\rm int} = b_0 \left[\frac{\omega_0 A_0^{(\rm r)}}{\omega A} \cos\phi - 1 \right], \tag{B.6}$$

where ω is the driving frequency, Q is the quality factor, $A_0^{(\rm r)}$ is the peak amplitude at the resonance frequency without interaction, A and ϕ are the amplitude and phase of the tip motion in the presence of interaction, respectively. In addition, k_0 and $b_0 (= k_0/Q\omega_0)$ are the stiffness and damping coefficient of the force sensor itself, and one should check the equivalence of Equation (B.6) and the equations used in this work.

The equation of motion of a driven damped harmonic oscillator with mass m_0, damping coefficient b_0, spring constant k_0, the driving force F_0 and the angular driving frequency ω is $m_0\ddot{x} + b_0\dot{x} + k_0 x = F_0 \exp(\imath\omega t)$. By letting the displacement $x(t) = A_0 \exp[\imath(\omega t - \pi/2 + \psi)]$, the solutions for the amplitude A_0

and the phase ψ in the absence of interaction are

$$A_0(\omega) = \frac{F_0}{\sqrt{(k_0 - m_0\omega^2)^2 + (b_0\omega)^2}} = \frac{F_0}{\sqrt{K_{\rm x}^2 + K_{\rm y}^2}}, \tag{B.7}$$

$$\psi(\omega) = \tan^{-1}\left(\frac{k_0 - m_0\omega^2}{b_0\omega}\right) = \tan^{-1}\left(\frac{K_{\rm y}}{K_{\rm x}}\right), \tag{B.8}$$

where

$$K_{\rm x} = b_0\omega = k_0 \cdot \frac{\omega}{Q\omega_0}, \quad K_{\rm y} = k_0 - m_0\omega^2 = k_0\left(1 - \frac{\omega^2}{\omega_0^2}\right). \tag{B.9}$$

It is noted that A_0 and ψ are dependent on the driving frequency ω. The peak amplitude $A_0^{(\rm r)}$ at the resonance frequency ω_0 is written by

$$A_0^{(\rm r)} = A_0(\omega = \omega_0) = \frac{F_0}{b_0\omega_0} = \frac{\sqrt{K_{\rm x}^2 + K_{\rm y}^2}}{b_0\omega_0} \cdot A_0, \tag{B.10}$$

and here ϕ in Equation (B.6) means the phase difference between without interaction at the resonance frequency ω_0 and with interaction at the driving frequency ω. Let θ be the phase difference between with and without the interaction at the driving frequency ω, then $\phi = \psi + \theta$. Figure B.4 shows the definitions of the amplitude and phase terms clearly.

To obtain the equations used in this article from Equation (B.6), $A_0^{(\rm r)}\sin\psi$ and $A_0^{(\rm r)}\cos\psi$ are firstly written by

$$\begin{aligned}
A_0^{(\rm r)}\sin\psi &= \left(\frac{\sqrt{K_{\rm x}^2 + K_{\rm y}^2}}{b_0\omega_0} \cdot A_0\right)\frac{K_{\rm y}}{\sqrt{K_{\rm x}^2 + K_{\rm y}^2}} \\
&= \frac{K_{\rm y}}{b_0\omega_0} \cdot A_0 = Q\left(1 - \frac{\omega^2}{\omega_0^2}\right)A_0, \\
A_0^{(\rm r)}\cos\psi &= \left(\frac{\sqrt{K_{\rm x}^2 + K_{\rm y}^2}}{b_0\omega_0} \cdot A_0\right)\frac{K_{\rm x}}{\sqrt{K_{\rm x}^2 + K_{\rm y}^2}} \\
&= \frac{K_{\rm x}}{b_0\omega_0} \cdot A_0 = \frac{\omega}{\omega_0} \cdot A_0.
\end{aligned}$$

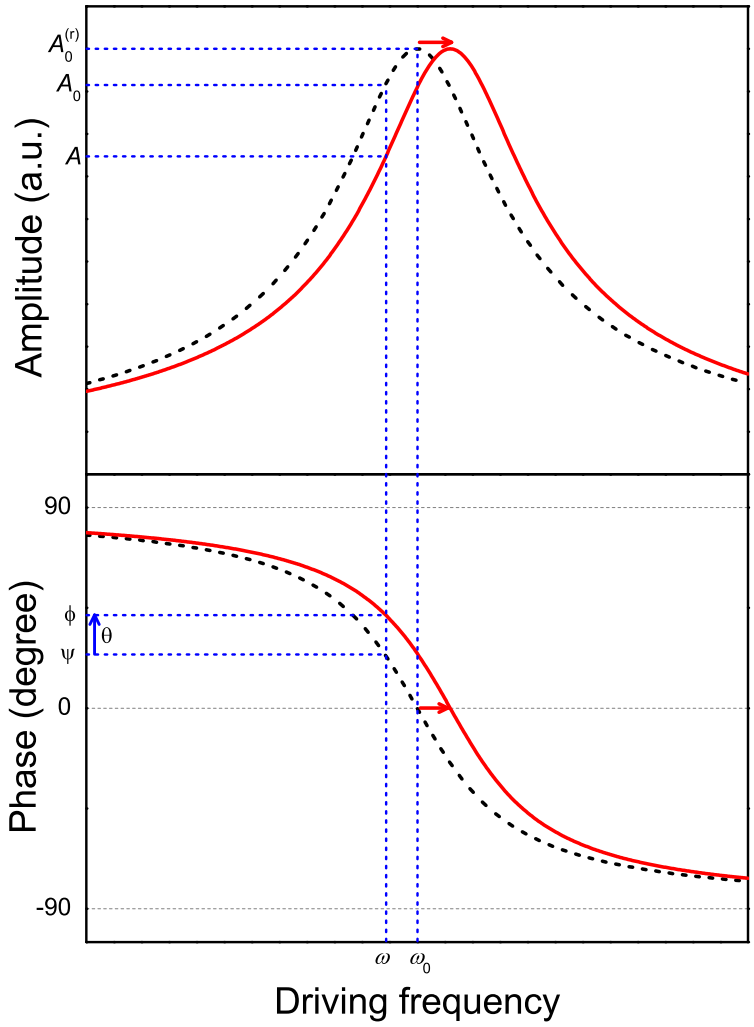

Figure B.4: The amplitude and phase as a function of the driving frequency. The dashed (solid) lines represent the resonance curves without (with) an interaction. If the driving frequency is equal to the resonance frequency, i.e., $\omega = \omega_0$, the amplitude and phase are written as $A_0^{(\mathrm{r})}$ and 0, respectively, in the absence of interaction. A_0 and ψ (A and ϕ) are the amplitude and phase without (with) the interaction, respectively, when the driving frequency is not same as the resonance frequency. The phase change between the absence and presence of the interaction is expressed by θ, i.e., $\phi = \psi + \theta$.

Then, the interaction stiffness $k_{\rm int}$ is expressed by

$$\begin{aligned}
k_{\rm int} &= k_0 \left[\frac{A_0^{(\rm r)}}{QA} \sin\phi - \left(1 - \frac{\omega^2}{\omega_0^2} \right) \right] \\
&= k_0 \left[\frac{A_0^{(\rm r)}}{QA} (\sin\psi\cos\theta + \cos\psi\sin\theta) - \left(1 - \frac{\omega^2}{\omega_0^2} \right) \right] \\
&= k_0 \left[\frac{A_0}{QA} \left\{ Q \left(1 - \frac{\omega^2}{\omega_0^2} \right) \cos\theta + \frac{\omega}{\omega_0} \sin\theta \right\} - \left(1 - \frac{\omega^2}{\omega_0^2} \right) \right] \\
&= k_0 \left[\frac{\omega}{Q\omega_0} \frac{A_0}{A} \sin\theta + \left(1 - \frac{\omega^2}{\omega_0^2} \right) \left(\frac{A_0}{A} \cos\theta - 1 \right) \right],
\end{aligned}$$

and the interaction damping coefficient $b_{\rm int}$,

$$\begin{aligned}
b_{\rm int} &= b_0 \left[\frac{\omega_0 A_0^{(\rm r)}}{\omega A} \cos\phi - 1 \right] \\
&= \frac{k_0}{Q\omega_0} \left[\frac{\omega_0 A_0^{(\rm r)}}{\omega A} (\cos\psi\cos\theta - \sin\psi\sin\theta) - 1 \right] \\
&= \frac{k_0}{\omega} \frac{\omega}{Q\omega_0} \left[\frac{\omega_0 A_0}{\omega A} \left\{ \frac{\omega}{\omega_0} \cos\theta - Q \left(1 - \frac{\omega^2}{\omega_0^2} \right) \sin\theta \right\} - 1 \right] \\
&= \frac{k_0}{\omega} \left[\frac{\omega}{Q\omega_0} \left(\frac{A_0}{A} \cos\theta - 1 \right) - \left(1 - \frac{\omega^2}{\omega_0^2} \right) \frac{A_0}{A} \sin\theta \right],
\end{aligned}$$

which are obtained from Equation (B.6). It is thoroughly checked that the formulas are exactly equivalent.

References

[1] M. Lee, J. Jahng, K. Kim, and W. Jhe, Appl. Phys. Lett. **91**, 023117 (2007).

[2] M. Lee, B. Sung, N. Hashemi, and W. Jhe, Faraday Discuss. **141**, 415 (2009).

Appendix C

Temporal behavior of the water nanomeniscus during approach and retraction

The transient behaviors of k_{int} and b_{int} that appear right after each stepwise change of the tip-sample distance contribute to the nonzero value of $\omega\tau_{\mathrm{R}}$, which are associated with the finite response time of QTF (time constant of about 50 ms for the resonance frequency $f_0 = 32$ kHz and the quality factor $Q = 5000$). The formation of the water meniscus is also observed in $47 < t < 47.5$ s in Fig. C.1, which is consistent with our previous study on the nucleation of the meniscus. [2] It is interesting to notice that a rise of the mechanical relaxation time in the range $47 < t < 48$ s followed by a subsequent decrease, as shown Fig. C.1, is observed.

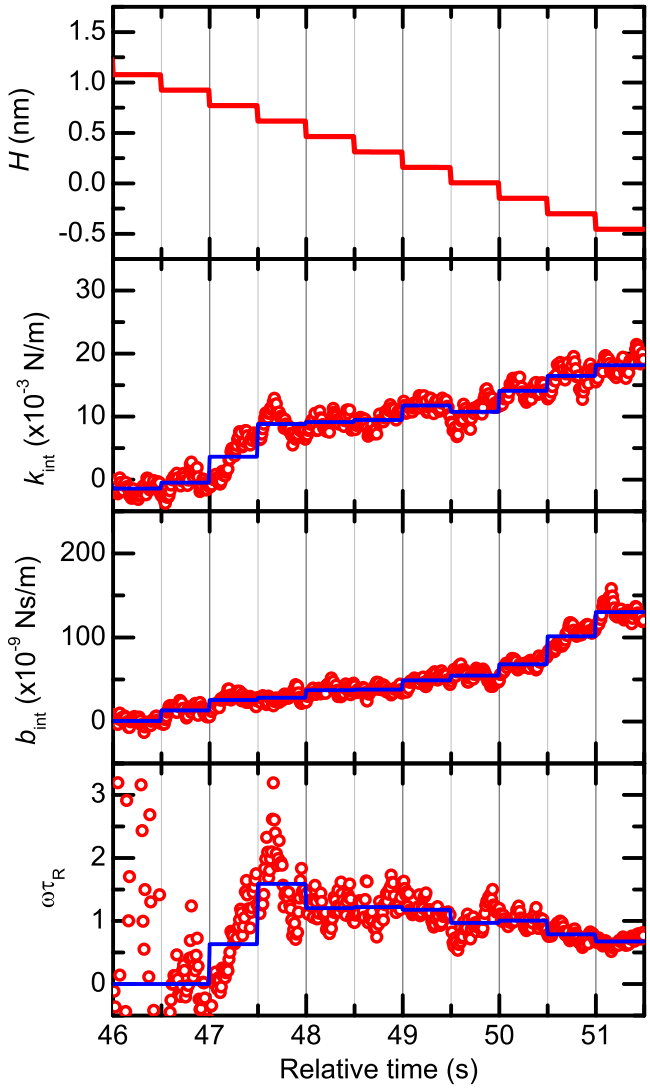

Figure C.1: Temporal behaviors of $k_{\rm int}$, $b_{\rm int}$ and $\omega\tau_{\rm R}$ during approach, shown in Fig. 5.2, are presented. The open circles (red) and the step-like lines (blue) in $k_{\rm int}$, $b_{\rm int}$ and $\omega\tau_{\rm R}$ denote their measured and averaged values at each tip-sample distance (presented in Fig. 5.2), respectively. Adapted from Kim *et al.* [1]

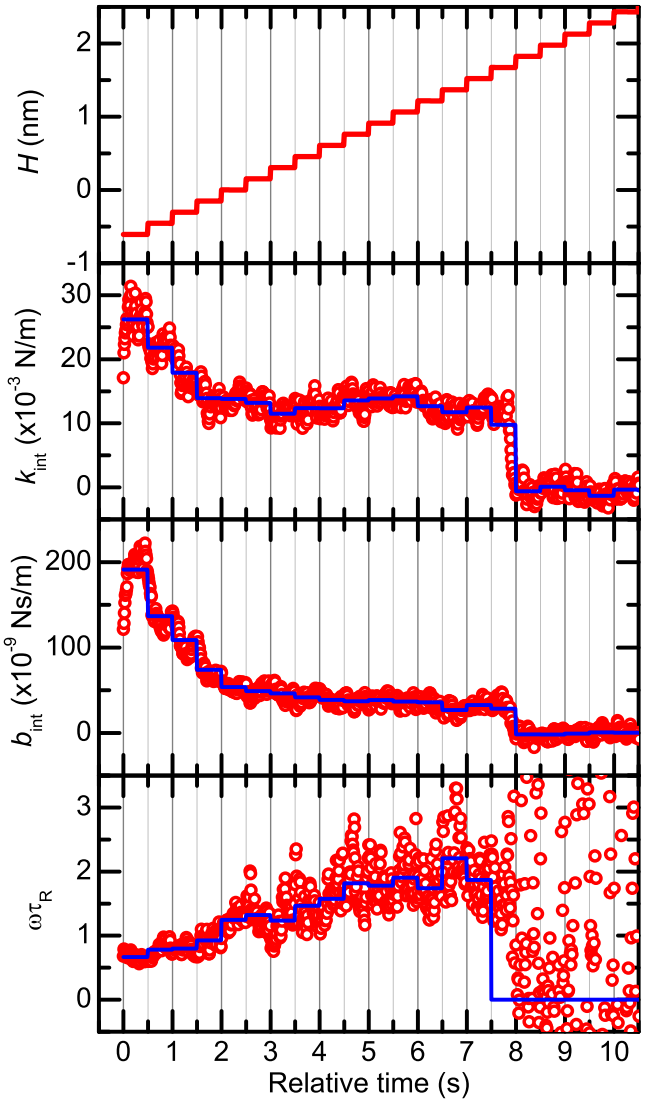

Figure C.2: Temporal behaviors of $k_{\rm int}$, $b_{\rm int}$ and $\omega\tau_{\rm R}$ during retraction, shown in Fig. 5.2, are presented. The open circles (red) and the step-like lines (blue) in $k_{\rm int}$, $b_{\rm int}$ and $\omega\tau_{\rm R}$ denote their measured and averaged values at each tip-sample distance (presented in Fig. 5.2), respectively. Adapted from Kim *et al.* [1]

For $7.5 < t < 8$ s in Fig. C.2, there is a stepwise drop of k_{int} and b_{int} accompanying the incubation delay, which clearly indicates the rupture of the water meniscus.

References

[1] J. Kim, D. Won, B. Sung, and W. Jhe, J. Phys. Chem. Lett. , accepted.

[2] B. Sung *et al.*, Appl. Phys. Lett. **103**, 213107 (2013).

Appendix D

Manuals of Programs by using LabVIEW software package

D.1 Time-resolved Data Acquisition System

Field programmable gate array (FPGA) 기반의 data acquisition system (DAQ)를 위하여 시간 분해능 (time-resolved) 측정이 가능한 LabVIEW software를 이용하여 프로그램을 작성하였고, 이것을 Time-resolved dynamic force microscopy (TRDFM)라 명명하였다. 이 프로그램의 특징은 다음과 같다.

1. TRDFM에서는 프로그래밍할 수 있는(programmable) 측정이 가능하다. 기존의 프로그램과는 다르게, 필요한 조건에 맞춰 자동으로 조작이 가능하다. 예를 들면 진폭이 일정값 이하로 떨어지고 나서 일정 시간동안 대기하면서 신호의 변화를 관찰한다든가, 접근/후퇴를 반복하고 일정 거리만큼 x, y축으로 이동을 한다든가 하는 것이 그것이다. 기존에는 PZT의 움직임이

달라지면 프로그램을 다시 작성하거나 수정하여야 했으나, 그것이 필요하지 않고, 명령어 세트를 프로그램에 입력하면 그 기능을 모두 구현할 수 있다.

2. 시간 분해능 측정이 가능하며, 데이터 처리 속도의 척도인 FPGA 루프(loop)의 주기가 1-2 μs로 매우 빠르다.

3. 주변기기인 함수 발생기(function generator), 록인 증폭기(lock-in amplifier), PZT(piezoelectric transducer), 피코모터(picomotor)를 프로그램을 통해 제어하고 상태를 읽어올 수 있다.

이 프로그램에서는 National Instrument 사의 FPGA 모듈(module)인 PXI-7833R을 기준으로 작성되었다. PXI-7833R은 3M 크기의 게이트 어레이(gate array)를 가지고 있으며 40 MHz의 클럭 속도(clock speed)로 동작한다. 또한 아날로그 입력(analog in, AI)과 아날로그 출력(analog out, AO)를 각각 8 채널씩 가지고 있으므로 차등 모드(differential mode)로 동작할 경우 아날로그 입출력이 각각 4채널을 통해 가능하다.

그림 D.1은 FPGA 기반의 장치 구성을 나타낸다. 호스트(Host)인 PC와 FPGA는 각각의 LabVIEW 프로그램이 구동되며 서로 통신하게 된다. 실제 데이터의 처리는 FPGA에서 이루어지는데, 록인 증폭기에서 받는 진폭과 위상의 전압 신호를 입력받으며, PC와의 데이터 처리 속도 차이를 극복하기 위해 FIFO (first in first out)의 버퍼(buffer)를 사용하여 저장한다. 또한 PZT에 x, y, z 세 축의 이동에 필요한 전압을 인가하며, 추후에 전기장 등의 인가를 위해 하나의 채널을 더 출력할 수 있도록 하였다.

호스트인 PC에서는 사용자가 실험에 필요한 조건을 설정하고 FPGA와의 통신을 통해 데이터를 처리하며, 주변 기기를 제어 및 설정 상태를 확인하는 역할을 한다. 데이터 획득이 시작되면 함수 발생기에서는 현재 설정되

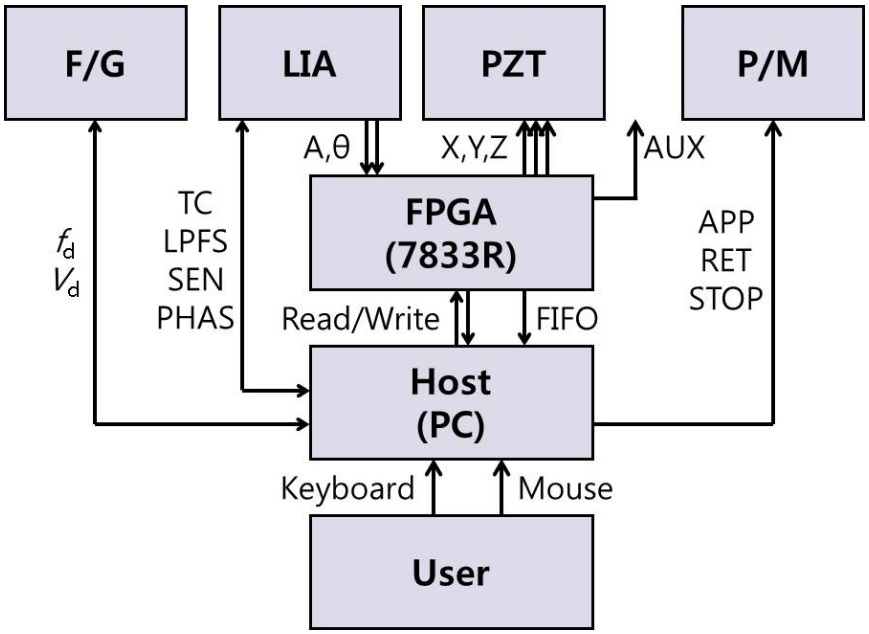

Figure D.1: Schematic diagram of the setup based on FPGA

어 있는 driving frequency f_d와 amplitude V_d를, lock-in amplifier에서는 time constant TC, low-pass filter slope LPFS, sensitivity SEN, reference phase PHAS를 읽어와서 정보 파일에 기록하게 되며, 이것을 데이터의 해석에 활용하도록 설계되어 있다. PZT의 제어는 FPGA 모듈을 통해서 가능하며, 개략적 접근(coarse approach)를 위한 피코모터(picomotor)의 제어 역시 가능하다.

참고로 함수 발생기는 Agilent 사의 33120A, 33220A에 맞게 설계되어 있으며, 록인 증폭기는 Stanford Research Systems의 SR830과 SR844를 지원한다. 주변 기기와의 통신은 라이브러리화 되어 있기 때문에 해당 제어 파일을 수정하면 다른 기종의 함수 발생기나 록인 증폭기를 사용할 때에도 쉽게 수정이 가능한 장점이 있다. 또한 현재 함수 발생기와 록인 증폭기는 GPIB (general

purpose interface bus)를 이용하고 피코모터는 직렬 포트(serial port, RS-232)를 이용한 통신을 하도록 되어 있는데, 이것 역시 자유롭게 조절할 수 있도록 프로그램을 작성하였다. 자세한 내용은 그림 D.4과 그 설명을 참고하면 된다.

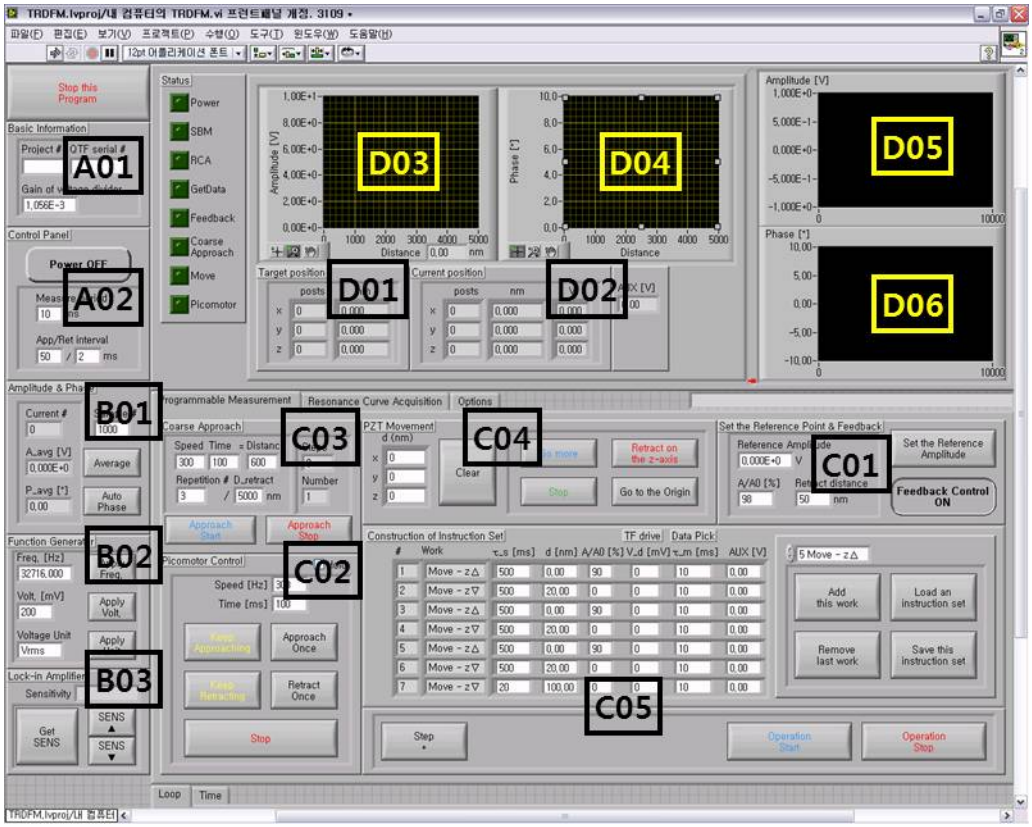

Figure D.2: Control panel of TRDFM.

그림 D.2은 TRDFM의 주 제어판을 나타내었다. 크게 A, B, C, D 네 부분으로 나뉘어져 있는데, A 부분은 실험의 프로젝트를 기술하는 부분(A01)과 프로그램의 전원 및 기본 측정/이동 간격을 설정할 수 있는 부분(A02)이다. B 부분은 현재 입력되고 있는 진폭과 위상의 평균을 구하고, 자동 위상

설정(B01)을 할 수 있는 부분과 함수 발생기(B02)와 록인 증폭기(B03)에 대해 설정을 할 수 있는 부분으로 이루어져 있다.

C 부분은 제어에 있어 가장 중요한 부분으로, 팁과 시료의 충돌을 방지하기 위한 진폭의 되먹임 설정(C01)부분, 피코모터를 구동하기 위한 부분(C02), 개략적 접근(C03)과 촘촘한 접근(C04)을 위한 부분과 함께 실험을 위한 설정 부분(C05)로 이루어져 있다.

D 부분은 상태를 보여주는 부분으로 목표 위치(D01)와 현재 위치(D02)를 보여주며 C03에서의 제어를 통해 개략적 접근을 하게 되면 PZT의 변위에 대한 진폭(D03)과 위상(D04)을 보여주는 부분, 현재 측정되고 있는 진폭(D05)과 위상(D06)을 시간의 흐름에 따라 계속 보여주는 부분으로 이루어져 있다. 이 프로그램에서 진폭의 단위는 V(volt)이며 위상의 단위는 도(degree)이다.

A01 부분은 현재의 프로젝트 번호와 QTF 및 탐침의 일련번호 및 분압기(voltage divider)에 대한 값을 입력하는 곳이다. 참고로 탐침의 일련번호에서 맨 첫 알파벳 혹은 맨 마지막 알파벳에 QTF의 종류를 넣으면 해석 프로그램(IDPU)에서 그 값을 기반으로 QTF의 용수철 상수(stiffness) k_0의 값과 압전 커플링 상수(piezoelectric coupling constant) α의 값을 설정하게 됨을 알려둔다.

A02 부분의 각각의 단추에 대한 설명은 다음과 같다. 'Power' 단추는 눌러 ON 상태가 되면 아래 간격마다 측정 및 이동을 할 수 있다. 'Measure period' 변수는 기본 측정의 시간 간격을 밀리초(ms) 단위로 설정한다. 'Staying interval' 변수는 기본 이동의 시간 간격을 밀리초(ms) 단위로 설정한다. 시간 만약 마이크로초의 단위를 사용하고자 한다면, 음수로 입력하면 된다. (예를 들어 -500을 입력하면 500마이크로초로 동작한다)

B01 부분에서 'Average' 단추는 위의 횟수만큼 진폭과 위상을 측정하여 오른쪽에 그 평균값을 표시한다. 'Auto Phase' 단추는 측정된 위상의 평균값으로부터 록인증폭기의 기준 위상을 조절함으로써 현재 측정되고 있는 위상의 평균이 0이 되도록 설정한다.

B02 부분에서 'Apply Freq.', 'Apply Volt.', 'Apply Unit.'는 왼쪽에 있는 진동수(Hz), 전압(mV), 전압단위(Vrms 혹은 Vpp) 값을 함수 발생기에 적용하도록 하는 단추이다. 또한 B03 부분에서 'Get SENS' 단추는 현재 록인증폭기의 민감도(sensitivity)를 전압 단위로 받아오며, 그 값을 기준으로 현재 입력되고 있는 진폭의 실제 전압값을 표시한다. 또한 'SENS ▲'와 'SENS ▼' 단추는 록인증폭기의 민감도의 값을 각각 증가, 감소시키는 단추이다.

제어부인 C 부분에 대한 설명은 다음과 같다. C01 부분에서 되먹임 제어는 'Feedback Control'이 'ON'인 상태에서 기준 진폭 'Reference Amplitude'와 비율'A/A0'로부터 설정할 수 있다. 되먹임 설정은 측정된 진폭이 기준 진폭과 비율의 곱보다 작은 경우, 탐침에 외부 힘이 작용했다고 판단하고, 'Retract distance'만큼 z축의 piezo displacement를 후퇴시켜 탐침과 시료의 거리를 떨어뜨리게 된다. 'Set the Reference Amplitude' 단추를 누르면 현재 측정된 진폭을 기준 진폭으로 설정하게 되며, 사용자가 직접 기준 진폭을 설정할 수도 있다.

C02 부분은 탐침과 시료 사이의 거리를 큰 간격으로 조절하기 위해 피코모터를 제어하는 부분이다. 'Keep Approaching' 버튼과 'Keep Retracting' 단추는 각각 탐침 쪽에 연결된 피코모터를 구동하여 접근 혹은 후퇴를 지속적으로 일어나도록 한다. 이 때 이동속도는 'Speed [Hz]' 단추에 의해 결정된다. 또한 움직이고 있는 피코모터는 'Stop' 단추를 누르면 정지한다. 또한 피코모터를 일정 시간동안 1회 접근 혹은 후퇴를 하게 하려면 'Approach Once' 혹은

'Retract Once' 단추를 누르면 된다. 피코모터는 스텝 모터가 아니고 마찰을 이용하기 때문에 구동할 때마다 이동하는 거리가 다를 수 있음에 주의해야 한다. 자세한 내용은 피코모터의 사용자 설명서를 참고하라.

C03 부분은 피코모터와 PZT를 움직여서 시료와 탐침의 개략적 접근이 이루어질 수 있도록 하는 부분이다. 'Approach Start' 단추를 누르면 PZT의 z축 방향이 움직이면서 시료와 탐침이 점점 가까워지게 된다. 이 때 진폭과 위상 신호의 변화는 표시부인 D03과 D04에 나타난다. 거리가 가까워졌다는 것을 탐침의 신호 변화로부터 인식하게 되는데, 신호의 변화는 C01 부분의 되먹임 제어에 있는 설정값을 기준으로 동작하며, 현재 측정 진폭이 기준 진폭 'Reference Amplitude'와 진폭 비율 'A/A0'의 곱보다 작으면 신호의 변화로 감지한다. 신호의 변화가 감지된 경우에는 C01 부분의 되먹임 제어에서 후퇴 거리 'Retract distance'만큼 z축을 후퇴한 다음 C03 부분의 'Repetition #'에 주어진 횟수만큼 반복하게 되며, 해당 횟수만큼 신호가 감지된 후에는 C03의 'D_retract'에 주어진 거리만큼 후퇴한 상태에서 개략적 접근이 종료된다. PZT의 전체 범위만큼 움직여도 탐침의 신호에 변화가 없을 경우에는 피코모터를 움직여서 시료와 탐침이 서로 가까워지게 한 다음, 다시 PZT를 움직여서 신호의 변화가 있을 때까지 이 과정을 반복한다. 이 때 피코모터를 속력 'Speed'와 시간 'Time'으로 움직이면 이동거리 'Distance'만큼 이동한다고 간주하고 PZT의 전체 범위를 이동거리 'Distance'로 나눈 값의 횟수만큼 이동하게 된다. 예를 들면, PZT의 전체 범위가 5000 nm이고 'Speed'는 300, 'Time'은 100, 'Distance'가 600 nm라면, PZT를 움직여서 신호의 변화가 없다면 300의 속력으로 100밀리초만큼 피코모터를 구동하는 과정을 8회(5000 nm / 600 nm) 반복한다는 의미이다.

C04 부분은 PZT를 이동하는 부분이다. PZT를 이동하고자 하는 목표 위치와 현재 위치는 각각 D01과 D02 부분에 표시된다. C04 부분의 'd (nm)'에 거리를 기록하고 'Go more' 단추를 누르게 되면 '목표 위치'로부터 추가로 이동하도록 설정된다. '현재 위치'가 아닌 '목표 위치'의 추가 변화임에 유의해야 한다. 참고로 PZT의 움직임은 FPGA에서 제어하게 되는데, '현재 위치'에서 '목표 위치'를 향해 'staying time'마다 1비트(bit)씩 움직이며, '목표 위치'의 x, y, z축의 값이 '현재 위치'의 그것들과 모두 다를 경우의 우선순위는 z축, x축, y축이다. 'Stop' 단추는 '목표 위치'를 '현재 위치'와 같게 만들어서 PZT가 움직이지 않게 한다. 'Retract on the z-axis' 단추는 '목표 위치'의 z축 값을 0으로 만들어서 z축으로 후퇴하게 하여 탐침과 샘플이 멀어지게 만들며, 'Go to the Origin' 단추는 '목표 위치'의 x, y, z축의 값을 모두 0으로 만들어준다. 'Clear' 단추는 왼쪽의 'd (nm)'에 기록된 거리를 모두 0으로 초기화시키는 역할을 한다.

C05 부분은 실제 실험을 수행하고 데이터를 수집하게 하는 부분으로 앞서 언급한대로 프로그래밍할 수 있는(programmable) 측정을 가능하게 하기 위해서 명령어 세트를 작성하게 된다. 명령어 세트는 번호순으로 실행되며, 작업(Work)은 정지(rest)와 x, y, z축으로 각각 증가/감소 등 총 7개의 작업이 가능하며, 이 중 정지는 PZT를 움직이지 않은 상태에서 기다리거나, 시간의 흐름에 따라 신호의 변화를 관찰하기 위해서 사용한다. 다음 명령으로 넘어가기 위한 조건은 거리 조건 'd [nm]'이나 진폭 비율 조건 'A/A0 [%]'인데, 둘 중 하나만 만족하면 다음 명령으로 넘어가며, 값이 0인 경우에는 그 조건에 대해 판단을 하지 않는다. 측정 중의 이동 간격은 'τ_s [ms]'에 의해 정해지며, 측정 간격은 'τ_m [ms]'에 의해 정해지고, 'V_d [mV]'는 함수 발생기에서 발생되는

구동 전압을 바꿀 수 있는 부분이며, 'AUX [V]'는 필요한 경우 한 채널(CH 3)로 전압을 출력(0-10 V)할 수 있는 기능으로, 탐침에 전기장을 인가하는 등의 기능을 필요할 때 사용 가능하다.

작업의 추가는 위에서 명령을 선택한 후 'Add this work' 단추로, 마지막 작업의 삭제는 'Remove the last work' 단추로 가능하다. 현재 화면에 보이는 7개의 작업까지 편집이 가능하며, 그보다 많은 개수의 작업을 만들거나 편집하려면 메모장으로 명령어 세트를 작성한 후에 'Load an instruction set' 단추로 불러오는 것이 편리하며, 'Save this instruction set' 단추를 이용하면 저장이 가능하다.

D부분의 상태 표시는 앞서 설명한대로 D01은 '목표 위치'를 나타내며 D02는 '현재 위치'를 보여준다. 개략적 접근할 때의 PZT 변위에 대한 진폭과 위상은 각각 D03과 D04에 나타난다. D05와 D06에는 현재 시간 경과에 대한 진폭과 위상 그래프를 나타낸다.

그림 D.3에서는 탐침의 공명 곡선을 얻기 위한 탭과 그것을 설정하기 위한 E 부분으로, 'Programmable Measurement' 옆에 있는 'Resonance Curve Acquisition'이라는 탭을 선택하면 볼 수 있다. 이 탭을 선택하는 경우 프로그램이 실행 중이라면 위쪽에 나타났던 그림 D.2의 D03과 D04가 D07과 D08로 바뀌는 것을 확인할 수 있으며, 이것은 진동수에 대한 진폭과 위상을 각각 나타낸다. 또한 D09에서는 시간의 경과에 대한 진동수의 변화 내용을 나타낸다.

E01 부분에서는 측정하고자 하는 진동수의 범위를 지정할 수 있는데, 공명 진동수 근처에서 좀 더 조밀하게 측정할 수 있도록 기능이 구현되어 있다. 'Sparse'인 구간과 'Dense'하게 측정하고자 하는 구간의 범위와 진동수 간격을 설정할 수 있다. 또한 번거로움을 줄이기 위하여 E02에서는 함수 발생기에 현

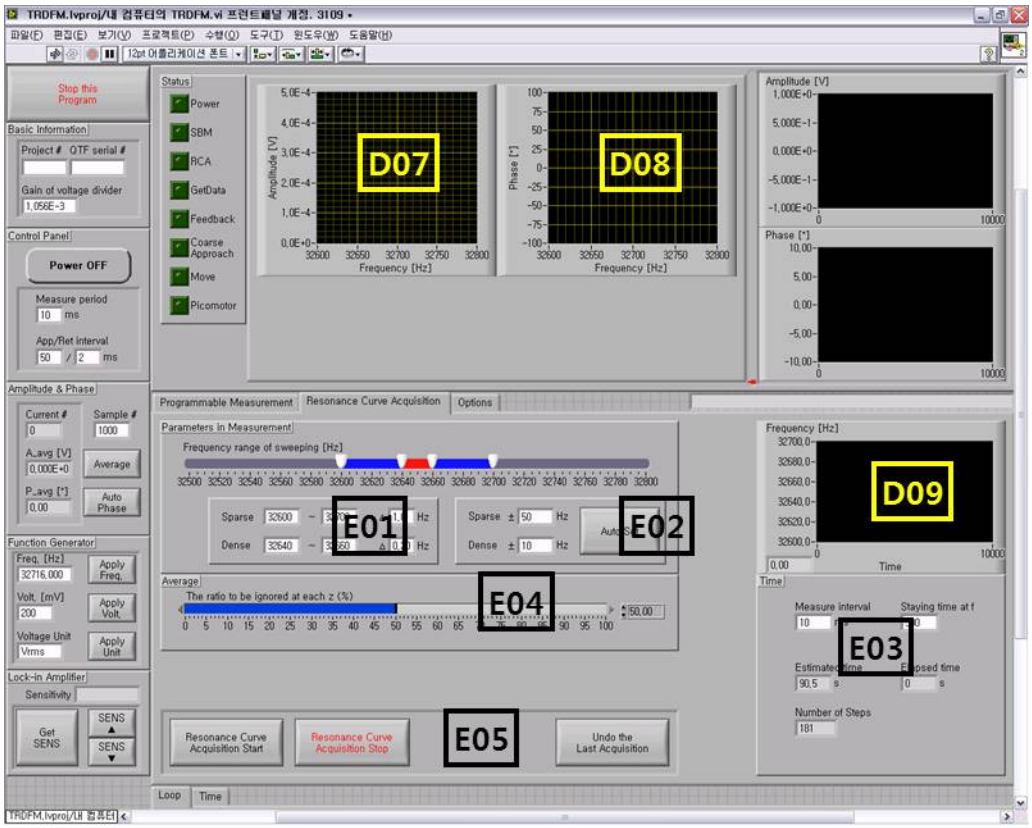

Figure D.3: Control panel for acquisition of resonance curve of TRDFM

재 설정되어 있는 진동수를 기준으로 좌우로 얼마나 측정할지를 정하고 'Auto Set'을 누르면 원하는 범위를 자동으로 설정해 준다.

E03 부분에서는 측정의 시간 간격('Measure interval')과 진동수 변화의 시간 간격('Staying time at f')을 설정할 수 있다. 진동수 변화의 시간 간격은 탐침의 Q값을 고려하여 정해야 한다. E04에서는 각각의 진동수에서 여러 번 측정된 값을 몇 퍼센트나 무시하고 평균을 취할지를 지정할 수 있다. 이 기능은 탐침의 구동 진동수가 변화하여 한 상태에서 다른 상태로 바뀔 때 천이

(transition)하는 데 시간이 필요하기 때문에 천이하는 동안의 신호를 무시하기 위하여 사용한다. 예를 들어 값이 0%이면 해당 진동수에서 얻어진 모든 값을 평균내게 되며, 50%라면 한 진동수에서 여러 번의 측정 중 앞의 절반은 무시하고 뒤의 절반만을 이용하여 평균을 내게 된다.

E05 부분에서는 공명 곡선을 얻기 위한 측정의 시작('Resonance Curve Acqusition Start')과 정지('Resonance Curve Acquisition Stop') 단추가 있다. 그리고 맨 마지막에 측정한 결과를 삭제할 수 있는 단추('Undo the Last Acquisition')가 있다.

그림 D.4는 'Options' 탭을 보여준 화면이다. 이 탭에서는 프로그램의 사용에 필요한 설정을 하게 되는데, 함수 발생기, 록인 증폭기, 피코모터와의 통신 방법을 정의하게 된다. 또한 록인 증폭기의 민감도를 설정하는 란이 있으며, PZT가 이동가능한 최대 범위를 설정할 수 있다. 또한 측정한 자료 파일이 저장될 폴더와, 접근 곡선(approach curve)과 공명 곡선을 측정할 때의 실험 조건을 자동으로 기록되는 정보 파일의 이름도 지정할 수 있다.

그림 D.5는 프로그램의 구동 흐름을 나타낸다. TRDFM를 실행하게 되면 처음으로 주변 장비를 초기화하고 정상적으로 동작하는지를 확인하며 프로그램에 필요한 값들을 읽어오게 된다. 그 다음으로는 프로그램 내부에서 사용되는 변수들을 초기화하게 된다. 이후에는 사용자 입력에 따라 루프를 반복하게 되는데, 우선 사용자 입력을 받은 후, FPGA에서 데이터와 측정값, 변수를 받아 온 다음 사용자 입력과 FPGA의 변수를 바탕으로 판단을 한 다음, FPGA로 그 다음 동작에 필요한 변수의 값을 출력하게 된다. 이 루프를 반복하다가 측정이 끝나면 FPGA를 닫고 데이터를 저장한 후 프로그램을 마치게 된다.

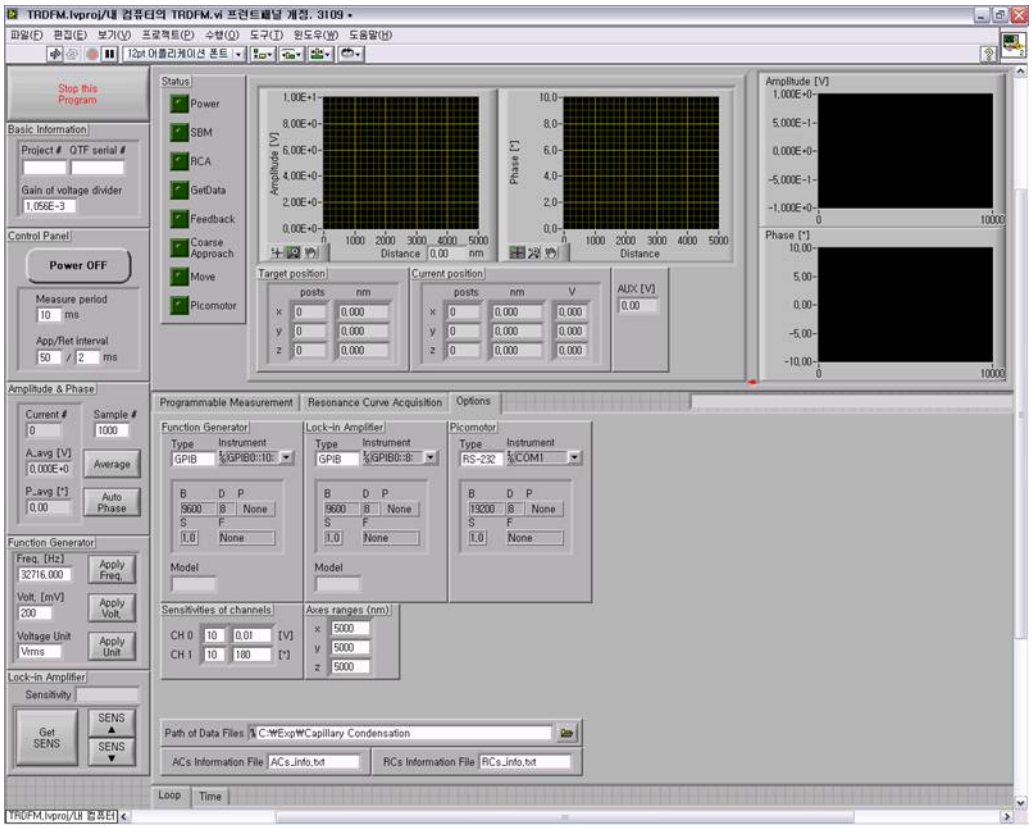

Figure D.4: Control panel of setting the options of TRDFM

그림 D.6는 FPGA에서 실행되는 프로그램의 제어판을 나타낸다. LabVIEW 프로젝트 기능을 사용하여 PC(host)에서 구동되는 그림 D.2의 프로그램과 함께 구동되면, host의 지배를 받기 때문에 실질적으로 설정을 하거나 제어를 할 기회는 없다. 그러나 실험 중 현재 어떠한 조건에서 구동되고 있는지를 확인하려면 이 화면을 참고하면 된다.

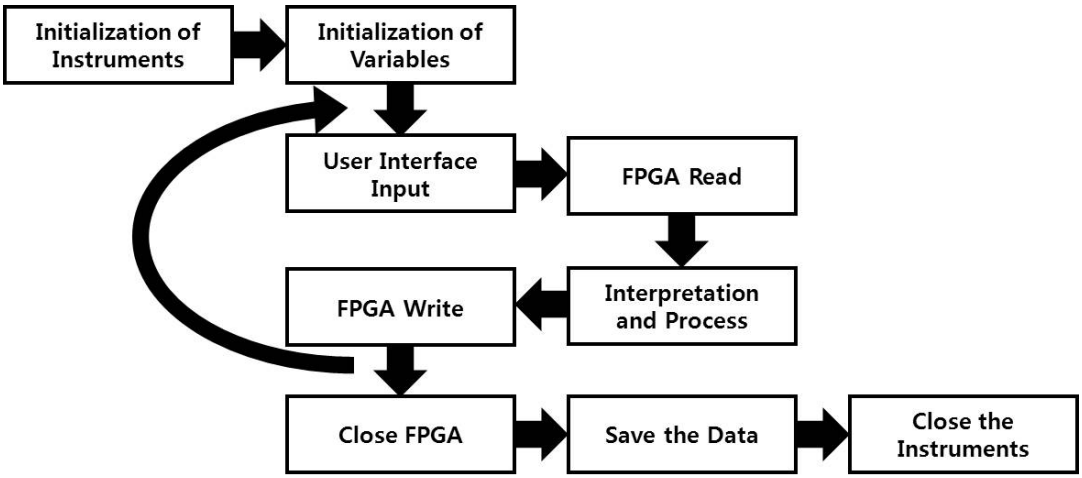

Figure D.5: Flow chart of TRDFM

D.2 Integrated Data Processing Unit

TRDFM를 통해 얻은 데이터는 시간, PZT의 z축 변위값, 진폭, 위상, 작업 번호가 기록된다. 측정된 값으로부터 물리적인 의미를 이해하기 위해서는 물리적인 의미를 가지고 있는 k_{int}, b_{int}로 변환이 필요하다. 이것을 하기 위해서 공명 곡선(resonance curve)을 측정하여 얻은 힘 센서의 특성으로부터 변환을 시행하여야 하는데, 데이터의 크기가 방대하고, 여러 번 실험의 결과를 좀 더 편리하고 자동으로 해석하기 위해서 이와 같은 프로그램을 만들어 Integrated Data Processing Unit (IDPU)라 명명하였다.

측정된 데이터는 크게 두 종류로 구분된다. 하나는 공명 곡선이 그것이며, 다른 하나는 접근 곡선(approach curve)이다. 공명 곡선은 탐침의 성질을 측정하기 위하여 사용하며, 구동 함수 발생기의 구동 진동수를 변화시키면서 탐침의 변화를 관찰하여 탐침의 성질을 알기 위한 것이다. IDPU는 이와 같은 측정된 데이터의 해석을 위한 프로그램이며, 주요 기능으로는 공명 곡선의

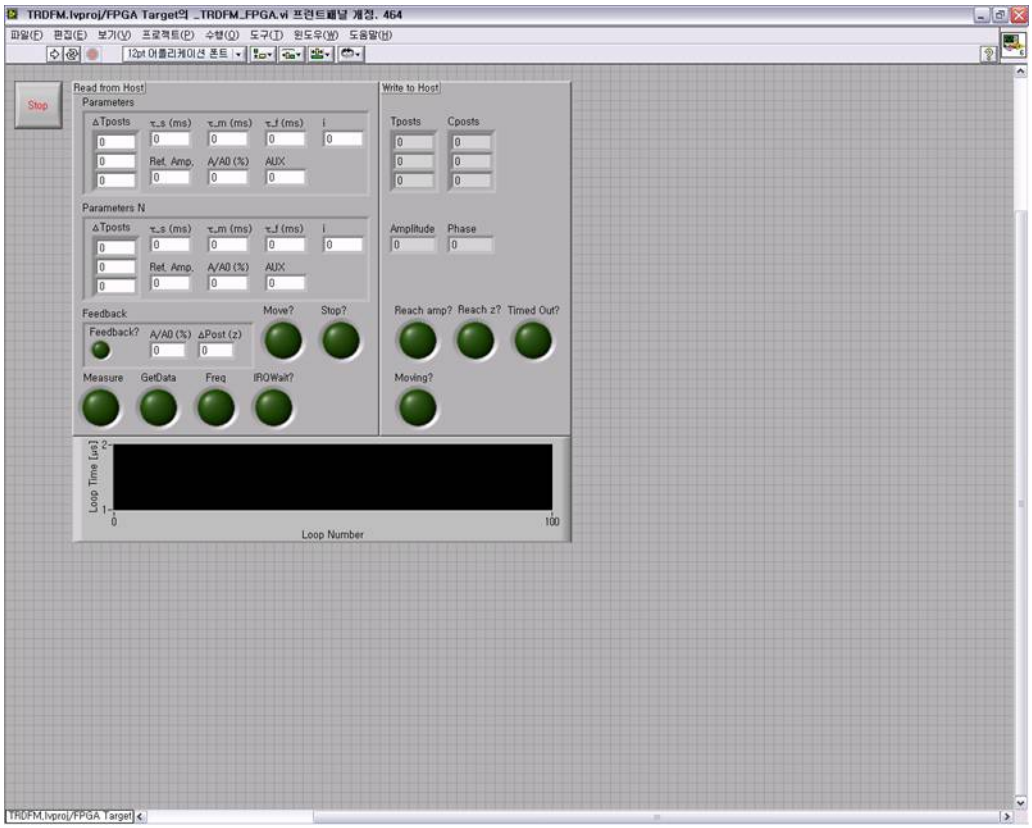

Figure D.6: Control panel of FPGA of TRDFM

위상의 오프셋(offset) 찾기와 변환의 기능이 있다. 이 프로그램의 특징은 측정된 접근 곡선을 가장 최근에 측정된 공명 곡선을 이용하여 자동으로 원하는 변환을 수행해준다는 것이다.

그림 D.7은 위상의 오프셋을 찾기 위한 화면을 보여준다. 공명 곡선은 8개의 맞춤 매개변수(fitting parameters)로 전증폭기(preamplifier)의 저항(R_g), 그와 병렬로 연결된 축전 용량(C_g)와 분압기(voltage divider)의 분압비율(gain) 값(G_VD), 함수 발생기의 구동 전압(V_d), 공명 진동수(f_0), Q값

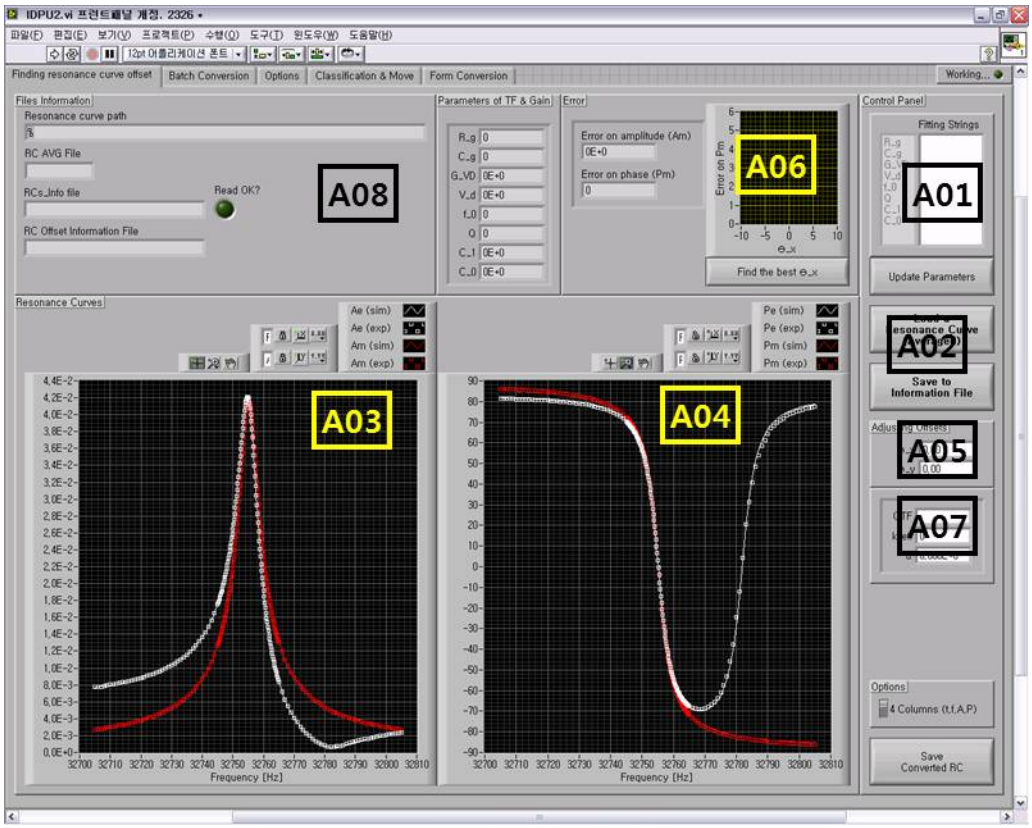

Figure D.7: Control panel of IDPU: Finding the phase offset

(Q), 진동 축전용량(C_1), 기생 축전용량(C_0) 등 8개이며 현재는 Origin 8.0 프로그램을 이용하여 맞춤한다.

접근 곡선은 진폭 변조(amplitude modulation)의 경우에는 함수 발생기로 일정한 진동수로 구동하며 외부 힘이 탐침에 작용함에 따라 탐침의 진폭과 위상을 기록하여 작용한 외부 힘의 특성을 이해할 수 있다. 그런데 전기 구동 QTF의 경우에는 기생 축전기의 영향이 공명 곡선을 왜곡하기 때문에 그것의 영향을 제거해야 한다.(자세한 내용은 B.1절 참고) 현재 Origin 8.0에서 공명

곡선의 맞춤은 진폭을 이용하는데, 위상의 경우에는 록인 증폭기의 기준 위상에 따라서 측정되는 위상의 값이 변화하게 되므로, 실험은 맞춤을 통해 알게 된 공명 진동수(f_0)에서 구동할 때의 위상을 0으로 하여 접근 곡선을 얻어서 변환을 하는 것이 좋다.

공명 곡선에서 위상의 오프셋을 찾기 위해서 처음 해야할 일은 맞춤 매개변수를 입력하는 과정이다. Origin 8.0에서 얻은 맞춤 매개변수는 그림 D.7의 A01에 입력한다. 그 후 'Load a Resonance Curve'(A02)를 눌러 평균된 공명 곡선 데이터를 하나 불러오게 되면 A03와 A04에 각각 진폭과 위상에 대한 공명 곡선이 출력된다. 이 때 점은 측정값, 실선은 맞춤 매개변수에 의해 계산되는 이론값이며, 흰색과 빨간색은 각각 전기적으로 구동된 탐침과 기계적으로 구동된 탐침의 공명 곡선을 의미한다. A03의 경우에는 Origin 8.0에서 맞춤한 그래프와 동일한 형태로 맞춤이 되어야 하며, A04에서 위상의 경우에 이론값은 전기적으로 구동할 때의 위상(P_e)과 기계적으로 구동할 때의 위상(P_m)이 공명 진동수에서 0이 되도록 설정되기 때문에 실험적으로 측정된 값에 오프셋을 주어 실험값과 이론값을 일치시킬 필요가 있다. 그것을 위해 A05에서 두 개의 오프셋을 조정할 수 있도록 제공되는데, 하나는 θ_x이고 하나는 θ_y이다. θ_x는 변환 전 측정된 위상값에 오프셋을 주는 것이고, θ_y는 변환 후 값에 오프셋을 준다. A04에 나타나는 P_e의 실험값과 이론값을 일치시키고, P_m의 실험값과 이론값을 일치시켜 오차를 최소로 하는 것이 필요하다. A05에 주어진 오프셋 값을 변화시켜도 가능하다. 이것을 자동으로 계산해주는 기능이 A06에 제시되어 있다. A06의 'Find the best θ_x' 단추를 누르면 0.01도 단위로 오차를 계산하여 오차가 최소인 θ_x 값을 찾아서 그 값으로 설정해 준다.

A07에서는 측정된 공명 곡선의 정보 파일에 기록된 그 측정에 사용된 탐침에 대한 정보를 가져와서 첫 글자 혹은 마지막 글자에 기록된 QTF의 종류를 인식하여, 그에 해당하는 QTF의 용수철 상수와 압전 커플링 상수의 값을 받아오게 된다. 또한 A08에는 불러오는 파일과 저장할 파일에 대한 정보가 기록되어 있다. 앞의 3장에 사용된 모델에 대해 A부터 G까지 용수철 상수와 압전 커플링 상수가 정의되어 있으며, 바꾸고자 하면 IDPU에 저장되어 있는 상수의 값을 바꾼 후 그 값을 기본값으로 하면 가능하다.

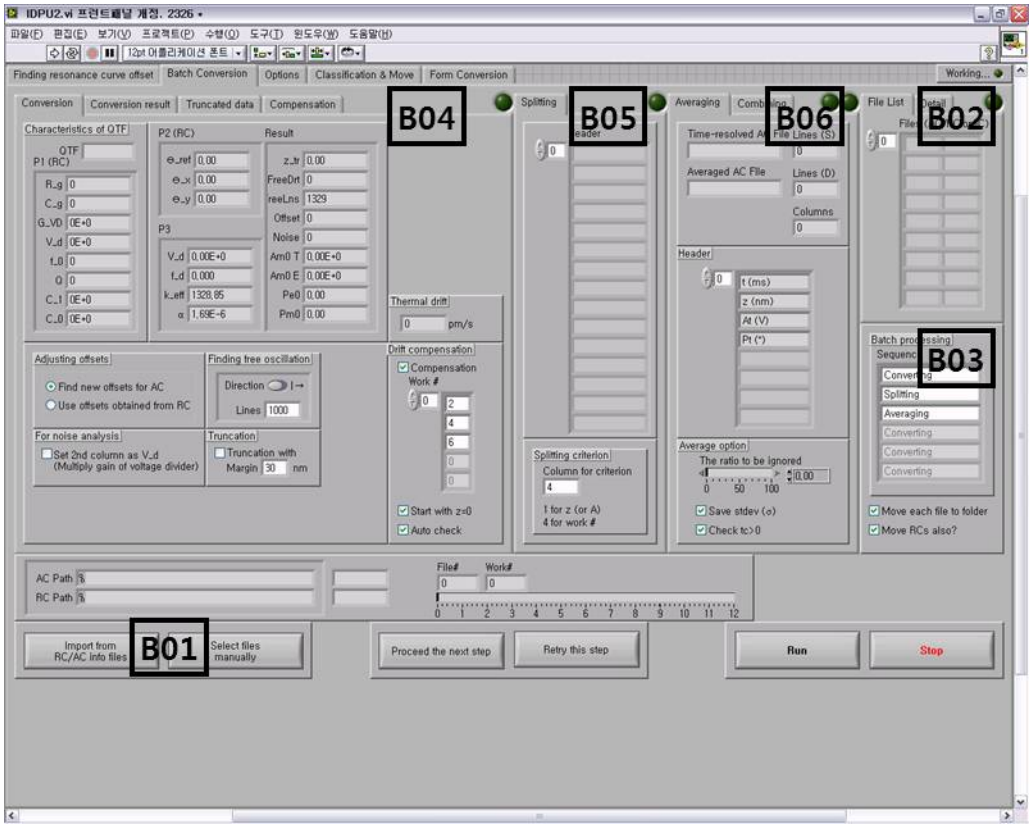

Figure D.8: Control panel of IDPU: Conversion, split and taking average

그림 D.8는 실제로 접근 곡선의 해석을 수행하기 위한 탭인 'Batch Conversion'의 화면이 나타나 있다. 우선 B01 부분을 살펴보면 두 가지 단추가 있는데, 왼쪽의 'Import from RC/AC Info files' 단추는 공명 곡선과 접근 곡선의 정보 파일로부터 측정된 전체 데이터를 불러와서 하나의 접근 곡선 데이터 파일에 그것 이전에 측정된 가장 최근의 공명 곡선 데이터 파일을 자동으로 대응시킨다. 오른쪽의 'Select files manually' 단추는 해석을 하고자 하는 몇 개의 파일을 선택하여 해석을 위한 변환을 할 수 있게 한다. 각각의 접근 곡선 파일에 어떤 공명 곡선 파일이 대응되는 지에 대한 내용은 B02에 나타나 있다.

변환을 할 때 어떤 과정을 거칠지를 B03에서 정하게 된다. 일반적인 접근 곡선 파일은 물리적 의미를 갖는 값으로의 변환(conversion), 작업 번호에 따른 분리(split), 같은 z값을 갖는 값들의 평균(averaging)의 과정을 거치게 된다. 그런데 예를 들어 잡음(noise)의 측정과 같은 경우 함수 발생기의 구동 진폭을 변화시키며 측정을 하게 되는데, 이 경우에는 분리를 우선으로 한 후 변환을 하고 평균을 낸 후 다시 합치는 형태로 진행이 필요하다. 이와 같이 원하는 과정을 순서대로 배열하여 프로그램을 실행하면 각 데이터에 대해 자동으로 반복하게 된다.

B04에는 변환에 필요한 내용이 나타나 있다. 변환은 공명 곡선에서 얻은 탐침의 특성을 바탕으로 접근 곡선에서 측정된 진폭과 위상으로부터 물리적 의미를 갖는 변수들을 계산하게 된다. 변환하여 얻을 변수들에 대한 선택과 그것에 대한 정보는 위의 'Options' 탭에서 확인 및 지정이 가능하다. 아울러 열 요동(thermal fluctuation)에 의한 표류(drift) 역시 보상할 수 있는 기능을 갖추었다. 앞서 언급한대로 적어도 3번 이상의 접근-후퇴 순환을 수행하고 표류가 일정하게 작용한다고 가정하면, 시간과 PZT z축의 변위가 어떻게 변

하는지를 관찰하여 최소 자승법을 사용하면 표류 속력(drift speed)를 얻을 수 있고, 보상 역시 'Drift compensation'의 'Compensation'이 ON으로 되어 있을 때 가능하다. 열적 표류에 필요한 시간과 PZT z축 변위에 대한 정보는 'Work #' 배열에 기록되어 있는 작업 번호의 데이터 첫 행에 있는 시간과 PZT z 축 변위를 사용한다. 'Auto check' 기능은 접근-후퇴 순환을 3번 반복 수행할 때 사용 가능하며, 한 번에 n개의 작업을 3회 반복한다고 하여 전체 작업의 개수가 3n+1 (n은 정수, 나머지 한 개는 마지막 후퇴를 위한 작업)일 때 n, 2n, 3n으로 'Work #'의 배열을 지정해 주는 역할을 한다.

B05에서는 분리에 필요한 설정을 하는데, 어느 것을 기준으로 분리할 것인지를 지정할 수 있다. 예를 들어 이 값을 1이라고 설정하는 경우, 접근 곡선이 시간(0), PZT z축 변위(1), 진폭(2), 위상(3), 작업 번호(4)의 순이기 때문에 z축 변위가 같은 것에 대해 한 파일로 묶이게 되며, 4라고 지정하는 경우에는 작업 번호가 달라질 때를 경계로 하여 다른 파일로 자르게 된다.

B06에서는 주어진 데이터의 평균을 내고 다시 합치는 기능에 대해 설정하는 부분이다. 일정한 PZT z축 변위 값에서 측정된 여러 번의 진폭과 위상을 그대로 평균을 취하게 되면 한 상태에서 다른 상태로 천이되는 동안 측정된 값들도 모두 평균에 영향을 미치게 된다. 이와 같이 천이 중 데이터가 평균에 영향을 미치는 것을 방지하기 위해서 평균을 취해야 할 전체 자료 중 앞 부분을 얼마나 무시할 것인지를 정해주는 설정은 'The ratio to be ignored'에서 가능하다. 또한 표준 편차를 함께 저장할 것인지를 설정할 수 있으며, 지연 시간(retardation time)이나 풀림 시간(relaxation time)과 같은 특성 시간(characteristic time)의 표준편차가 평균보다 클 경우, 그 평균값을 0으로 지정하여 다른 열에 추가로 저장하게 할 수 있다.

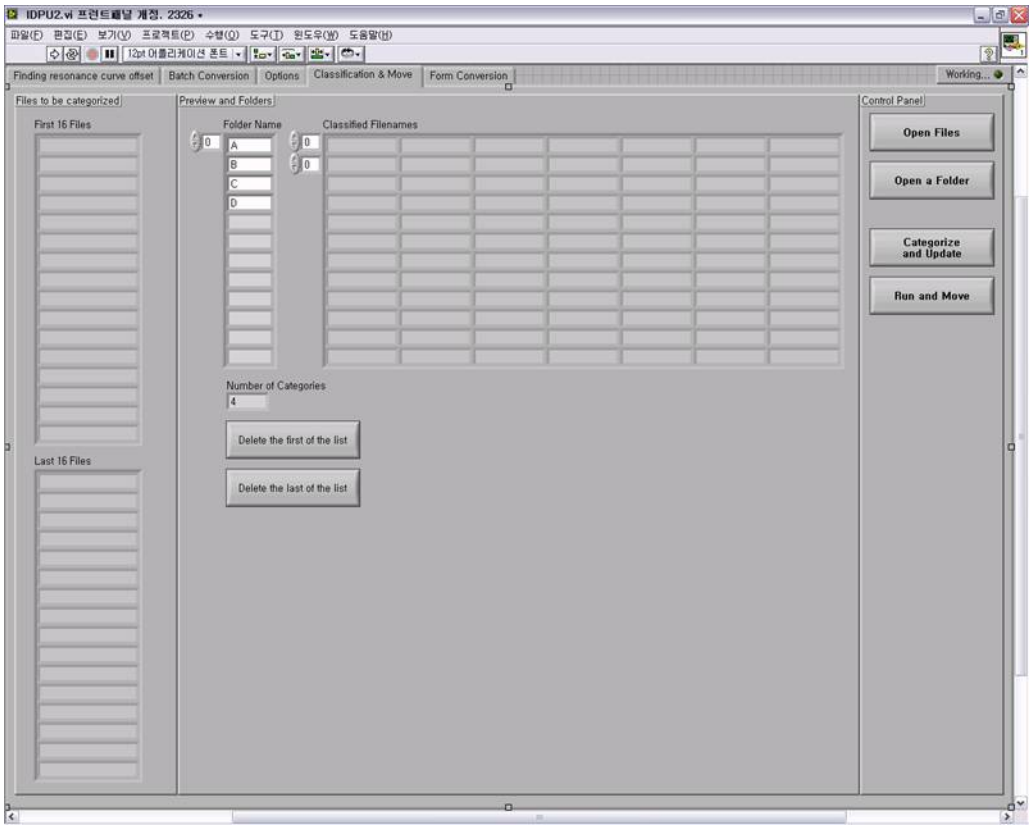

Figure D.9: Control panel of IDPU: Classification and move

그림 D.9은 반복적인 측정을 한 데이터 파일을 분리 기능을 이용하여 여러 파일로 쪼갰을 때 원하는 파일을 지정한 폴더에 분류하여 넣어주는 역할을 한다. 예를 들어 접근과 후퇴의 주기를 계속 반복하였다면, 접근할 때의 데이터와 후퇴할 데이터를 각각 다른 폴더에 이동하게 할 수 있는 것이다. 분류하고자 하는 파일은 몇 개의 파일만 목록에서 선택할 수도 있고, 폴더를 통째로 리스트에 정할 수도 있다.

그림 D.10는 측정된 데이터의 저장 형태를 변환하고자 할 때 사용한다.

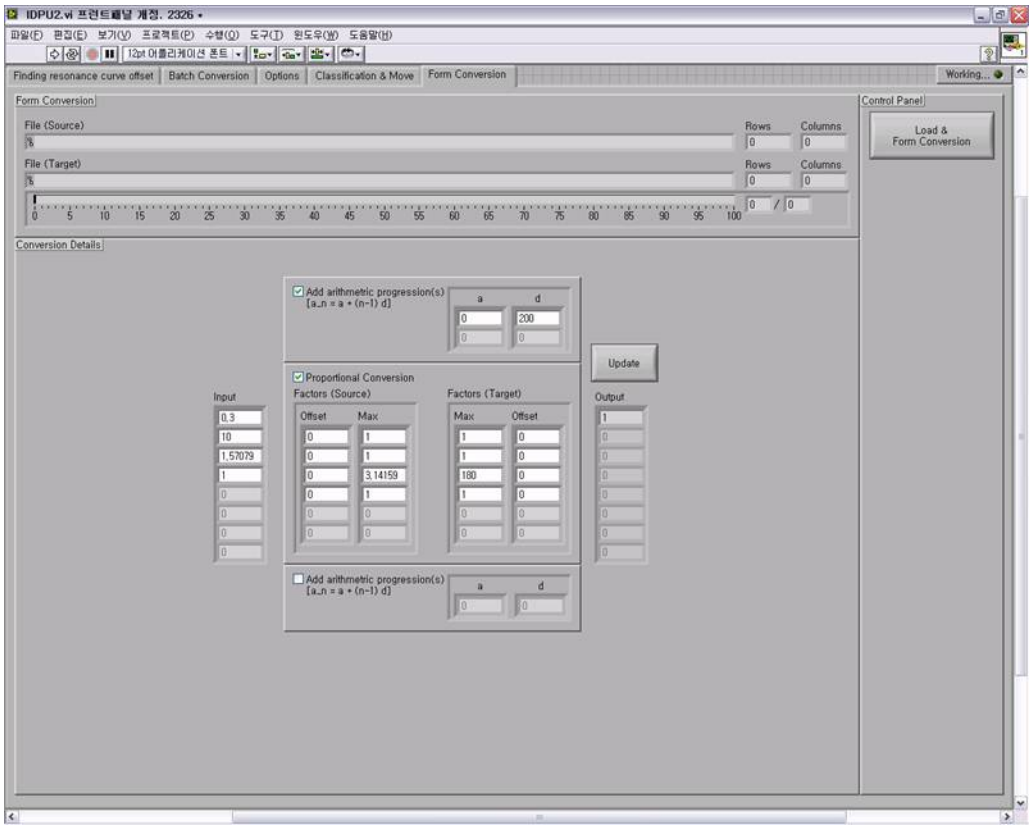

Figure D.10: Control panel of IDPU: Form conversion

예를 들어, 위상이 호도법(radian)으로 저장된 데이터를 60분법으로 변환하고자 하거나, 진폭의 데이터의 축소/확대 비율을 변환하고자 할 때 사용한다. 또한 열을 추가할 필요가 있을 때에도 등차수열의 형태로 추가할 수 있는 기능 역시 구현되었다.

D.3 Resonance Curve Acquisition

이 프로그램은 함수 발생기의 인가 진동수를 변화시키며 록인 증폭기에서 측정하는 진폭과 위상 신호를 기록하여 공명 곡선을 얻을 수 있는 프로그램이다. 프로그램의 이름은 RCA_DAQmx라고 하였으며, 여기서 DAQmx는 LabVIEW에서 제공하는 일반적인 아날로그 입출력을 이용한 데이터 수집 패키지로, FPGA와 구분하기 위하여 사용하였다. 이 프로그램의 장점은 시간에 대한 측정값과 그것의 평균값을 모두 저장할 수 있기 때문에 한 진동수에서 다른 진동수로 인가 진동수를 바꾸어서 측정된 데이터가 천이할 때의 거동을 관찰할 수 있다는 점이다. 그리고 원하는 경우 측정된 그래프를 겹쳐서 보여줄 수 있으므로 공명 곡선을 비교할 때 유용하다. 또한 필요한 경우 변화시킬 진동수의 범위를 자동으로 설정하여 주며, 전증폭기(preamplifier)의 증폭비율(gain)값을 얻는 데에도 유용하게 사용할 수 있으며, 진동수를 변화시키는 대신 잡음 측정을 위해 진폭을 변화시키는 기능 역시 포함되어 있다.

그림 D.11은 RCA_DAQmx의 주 제어판을 나타낸다. 기본적인 내용은 앞의 D.1절의 내용과 동일하다. 측정하고자 하는 진동수의 범위를 공명 진동수 근처에서 좀 더 조밀하게 측정하도록 설정할 수 있으며, 자동으로 필요한 범위를 적절하게 설정해주는 'Auto Set' 단추도 포함되어 있다. 적절한 구간을 지정하고 'Optimization' 단추를 누르면 적당한 범위에서 조밀하게 측정해야 하는 범위도 자동으로 설정해 준다. 예를 들어 32.768 kHz의 QTF의 Q인자(quality factor)가 5000 정도라면 이 범위는 50 Hz가 알맞으며, 65.536 kHz의 QTF는 100 Hz 정도, 100 kHz의 QTF는 200 Hz 정도로 설정하면 원하는 공명 곡선을 무난하게 얻을 수 있다. 그 왼쪽에는 이전에 측정된 그래프와 겹쳐서

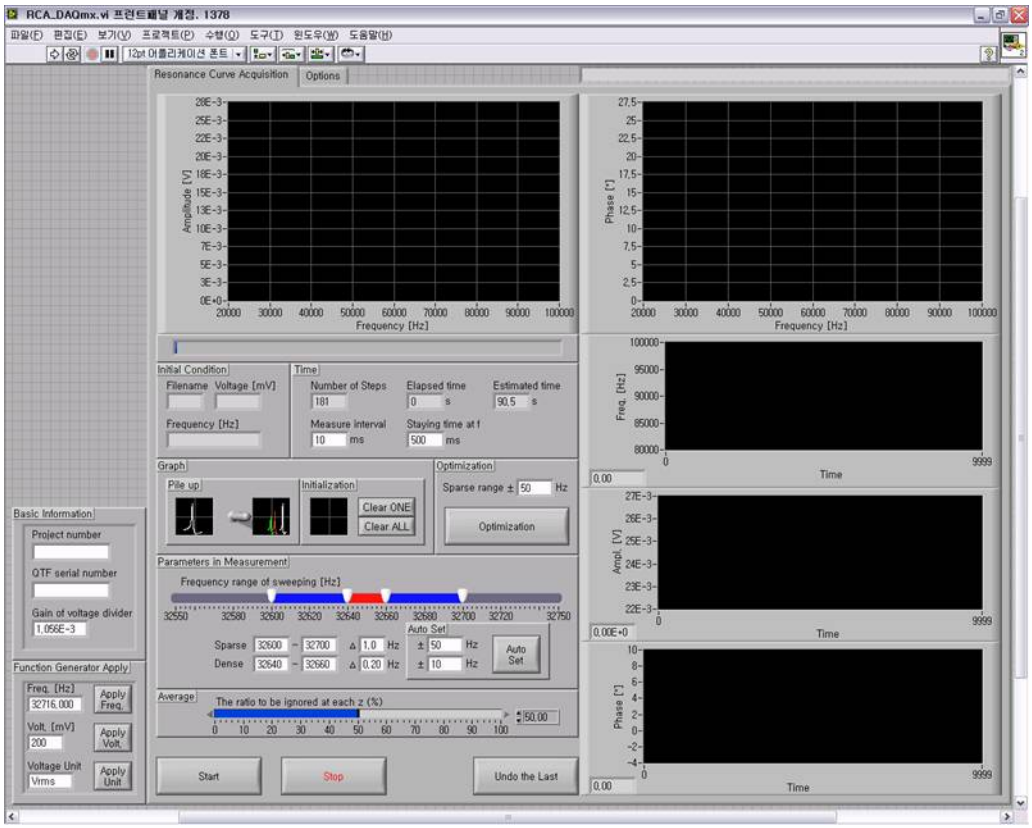

Figure D.11: Control panel of RCA_DAQmx

보여줄 것인지 아니면 최근 하나의 그래프만 보여줄 것인지 선택할 수 있으며, 그래프를 하나만 혹은 모두 지울 수 있는 단추도 포함되어 있다. 'Measure interval'에서는 측정 시간 간격을, 'Staying time at f'에서는 얼마의 시간마다 진동수를 변화시킬지를 결정할 수 있다. 아래쪽에는 각 진동수에 대해 측정한 진폭 및 위상 신호에 천이되는 구간이 존재하기 때문에 평균을 구할 때 얼마만큼의 비율을 무시한 후 평균을 취할 지를 결정할 수 있다. 'Start' 단추를 누르면 측정을 시작하며, 'Stop' 단추는 측정을 중단하고자 할 때 사용한다. 그

리고 원하는 설정이 제대로 되지 않은 상태에서 측정된 경우, 'Undo the Last' 단추를 누르면 최근 측정 데이터 파일과 측정에 관한 정보를 간단히 삭제할 수 있다.

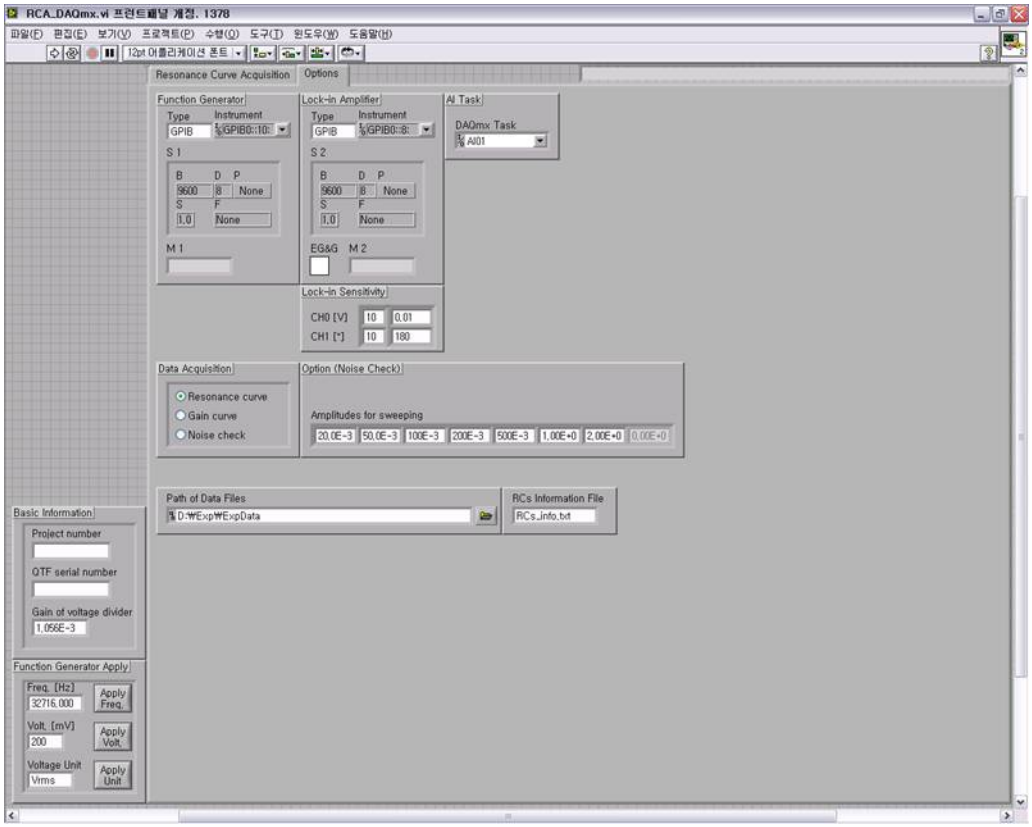

Figure D.12: Control panel of RCA_DAQmx: Options

그림 D.11에서 위쪽의 두 그래프는 각각 진동수에 대한 진폭과 위상 신호를 보여준다. 오른쪽 아래의 세 개의 그래프는 각각시간 변화에 대한 진동수, 진폭, 위상 신호를 나타내며, 측정의 종류에 따라 시간 변화에 대해 진폭과 위상 신호가 정상 상태에 도달하는지 확인할 필요가 있다. 특히 Q인자

(quality factor)가 클수록 정상 상태(steady state)에 도달하는 데 시간이 더 많이 필요하므로 'Staying time at f'의 값을 더 크게 설정하여야 정상 상태의 신호를 측정 및 수집이 가능하다.(자세한 내용은 2.4절 참고)

그림 D.12는 RCA_DAQmx에서 설정할 수 있는 선택사항을 나타내었다. 함수 발생기와 록인 증폭기와의 통신방법을 선택할 수 있다. 참고로 프로그램을 실행했을 때 주변기기와 정상적으로 통신이 된다면 M에 모델명이 표시된다. 그리고 'Data Acquisition'에서 어떤 측정을 할 지를 선택할 수 있는데, 'Resonance curve'는 흔히 얻는 진동수를 변화시켜 가며 진폭과 위상 신호를 측정하는 것이며, 'Gain curve'는 'Resonance curve'에서 얻은 진폭에 함수 발생기에서 인가한 진폭을 나누어 증폭비율을 함께 구해준다. 그리고 'Noise check'의 경우에는 오른쪽에 제시되어 있는 진폭을 함수 발생기에서 'Staying time at f'에 기록된 시간만큼 인가하면서 매 'Measure interval'마다 신호의 변화를 기록하게 된다.

D.4 Noise Spectrum Acquisition

이 프로그램은 Agilent 사의 Digital Signal Analyzer인 35670A 모델을 기준으로 작성되었다. 해당 모델은 측정한 데이터를 3.5인치의 플로피 디스크로 받게 되어 있어 데이터를 컴퓨터에 옮겨서 저장하는 것이 불편하여 GPIB로 통신하여 데이터를 받아올 수 있도록 프로그램을 작성하였다.

그림 D.13은 프로그램의 제어판을 나타낸다. 프로그램을 실행시켰을 때 맨 먼저 위쪽 상태에 'Model' 란에 '35670A'라는 문자열이 보이면 정상적으로 통신하고 있는 것이다. 평균에 대해 설정할 내용으로는 평균을 취할

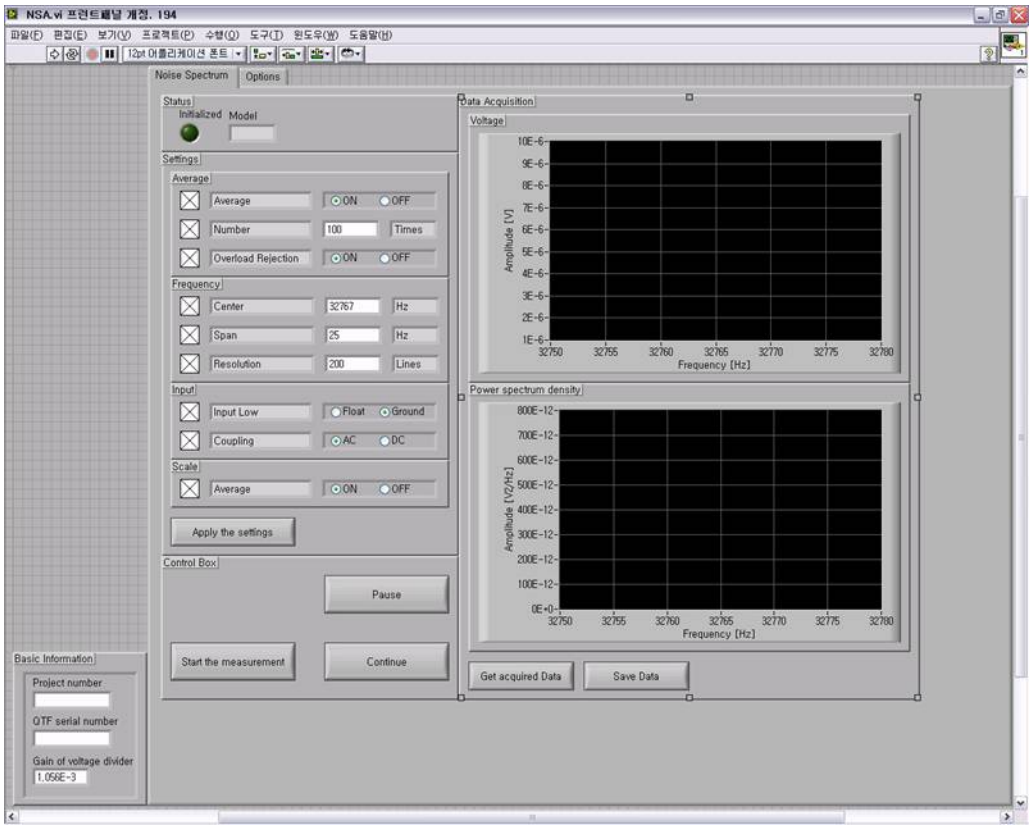

Figure D.13: Control panel of Noise Spectrum Acquisition

지 여부('Average'), 평균을 취하기 위한 반복 횟수('Number'), 과부하 배제 여부('Overload Rejection')가 있다. 주파수에 대한 설정 내용으로 중앙 주파수('Center')와 범위('Span') 그리고 해상도('Resolution')이 있다. 또한 입력에 대한 설정으로 'InputLow'에서는 입력 기준을 'Float'이나 'Ground'로 설정할 수 있으며 'Coupling'도 'AC' 혹은 'DC'로 설정할 수 있다. 그리고 척도에서 'Average'를 'ON'이나 'OFF'로 설정할 수 있으며, 'Apply the setting'를 누르면 한 번에 해당 내용을 설정하게 된다.

아래에는 측정에 대해서 제어할 수 있는 측정 시작('Start the measurement')과 일시 정지('Pause'), 계속('Continue') 단추가 마련되어 있다. 오른쪽에 있는 위와 아래의 그래프는 각각 주파수에 대한 전압(V)과 파워 스펙트럼 필도(power spectrum density, V^2/Hz)를 나타낸다. 'Get acquired data' 단추를 누르면 기기로부터 컴퓨터로 데이터를 전송하여 보여주며, 'Save data' 단추를 누르면 저장할 수 있다.

초 록

계면에서의 물은 여러 측면에서 중요한 역할을 한다. 특히 거친 고체 표면 사이에서 자연적으로 형성되는 물기둥은 마이크로미터 크기보다 작으며, 접착, 마찰 등의 자연 현상과 주사 탐침 현미경, 미세전자기계시스템 등의 기구를 이용한 측정에도 지대한 영향을 미친다. 이러한 나노미터 크기 물기둥의 역학적 성질을 탐구하기 위하여 정량적인 힘의 측정이 가능한 수정 소리굽쇠(quartz tuning fork) 기반의 원자 힘 현미경을 제작하였다. 또한 여러 고유진동수의 수정 소리굽쇠에 대해 선형의 반응을 보이는 전증폭기를 구성하였고, 다양한 종류의 수정 소리굽쇠에 대해 압전 커플링 상수, 반응 시간, 잡음 수준을 측정하고 원자 힘 현미경의 힘 센서로 사용하기에 최적의 수정 소리굽쇠를 선택하였다. [2장]

수정 소리굽쇠의 용수철 상수 값을 결정하는 것은 나노미터 크기에서 작용하는 작은 힘을 정량적으로 이해하기 위해 매우 중요하다. 수정 소리굽쇠와 함께 수정 소리굽쇠의 한 갈래를 고정시킨 큐플러스(qPlus) 센서의 용수철 상수의 결정에 대해 연구하였다. 수정 소리굽쇠와 큐플러스 센서의 용수철 상수를 계산할 수 있는 새로운 식을 제시하였으며, 고유 진동수가 다른 여러 가지 종류의 수정 소리굽쇠와 큐플러스 센서에 대해 질량 부착법을 이용하여 용수철 상수를 측정하였다. 측정된 결과와 제시한 이론식이 일치함을 증명하였으며, 기존에 널리 사용되던 캔틸레버(cantilever)에서의 용수철 상수 계산식을 이용할 경우 오차가 매우 크다는 것을 확인하였다. 또한, 큐플러스 센서와 수정 소리굽쇠의 용수철 상수를 비교하여 수정 소리굽쇠의 용수철

상수가 큐플러스 센서의 그것의 2배가 됨을 실험적으로 증명하였다. [3장]

원자힘 현미경에서 잡음을 정량화하고 최소 측정가능 힘에 대해 파악하는 것은 매우 중요하다. 잡음을 정량화하여 측정 가능한 최소 힘을 구할 수 있는 새로운 방법을 제시하였다. 또한 원자 힘 현미경에서 민감도를 향상시키기 위해 사용되어 온 양질 계수(quality factor) 제어가 최소 측정가능 힘에 미치는 특성을 이해하였다. 되먹임 회로를 이용하여 양질 계수를 조절하는 경우 신호 대 잡음비(signal-to-noise ratio)는 변화하지 않음을 확인하였다. 반면, 신호 대 잡음비가 변화하지 않음에도 불구하고 최소 측정가능 힘은 양질 계수 제어에 의해 변화할 수 있음을 확인하였다. 그것은 주파수 요동이 유효 양질 계수에 반비례하여 감소하기 때문이다. 그리고 최소 측정가능 힘과 힘 센서의 반응 시간의 관계로부터 힘 민감도의 최적화에 대해 논의하였다. [4장]

대기 조건에서 형성된 물기둥의 역학적 성질을 QTF 기반 비접촉 원자힘 현미경을 이용하여 측정하였다. 탐침-시료 거리를 증가시켜 나노 크기 물기둥을 늘이게 되면 물기둥의 풀림 시간이 증가하는 것을 확인하였다. 반면, 풀림 시간의 값과 물기둥의 부피의 상관관계는 발견되지 않았다. 늘이는 동안 풀림 시간의 증가는 물기둥의 표면적의 증가와 관계있을 가능성이 있다. 이 결과로부터 대기 조건에서 형성된 물기둥뿐만 아니라 나노 크기에서 구속된 물에 대한 이해를 높일 수 있을 것으로 기대한다. [5장]

시간 분해능 동적 힘 분석법을 이용하여 시간 경과에 따른 역학적 특성 변화를 연구할 수 있는 방법을 제시하였다. 나노 크기 물기둥의 생성과 성장에 대해 이 방법을 적용함으로써 물기둥이 생성될 때 활성화 시간을 정량적으로 측정할 수 있음을 보였다. 물기둥이 생성될 때의 접근 속도가 물기둥의 생성에 있어 유효 온도를 상승시키는 효과가 있다는 실험적 근거를 제시하였다.

또한 물기둥의 성장은 시간 상수가 수 초 정도까지 매우 느려질 수 있음을 확인하였고, 이는 물기둥의 성장에 있어 확산이 매우 느리다는 것을 가능성이 있음을 의미한다. 그리고 측정하는 동안 나노 크기에서의 열적 표류의 영향을 정량화하고 보상할 수 있음을 보였다. [6장]

요약하면, 수정 소리굽쇠 기반의 원자 힘 현미경을 이용한 나노 크기 물기둥의 역학적 특성에 대해 연구하였다. 힘 센서로 사용되는 수정 소리굽쇠의 가장 중요한 역학적 특성인 용수철 상수와 압전 커플링 상수에 대한 이해를 한층 높이고 잡음을 정량화하는 방법과 양질 계수 제어의 의미와 그 한계에 대해 관찰하였다. 이로써 수정 튜닝포크 기반 원자 힘 현미경 기술을 발전시켰으며 두 방법은 다른 시료나 대상에 대해 원자 크기에서 작은 힘을 정량적으로 측정하기 위한 방법으로 활용될 수 있을 것이다. 또한, 나노 크기 물기둥을 늘일수록 역학적 풀림 시간으로부터 길어지지만, 그것의 부피는 거의 무관하다는 것을 발견하였다. 이것은 증가한 역학적 풀림 시간이 나노 물기둥의 표면적 증가에 의한 것이라는 가능성과 함께 비접촉 원자힘 현미경이 공기/물 계면의 특성을 연구하는 새로운 도구가 될 수 있음을 제시한다. 아울러 시간 분해능 동적 힘 분석법은 나노 크기에서 일어나는 동역학적 현상을 이해하는데 중요한 도구가 될 것으로 기대한다.

주요어 : 점탄성, 풀림 시간, 수정 튜닝포크, 잡음, 시간 분해능 동역학적 힘 분석

학 번 : 2007-20412

Publication List

SCI Journals

1. Sangmin An, Jongwoo Kim, Kunyoung Lee, Bongsu Kim, Manhee Lee and Wonho Jhe, "Mechanical properties of the nanoscale molecular cluster of water meniscus by high-precision frequency modulation atomic force spectroscopy", *Appl. Phys. Lett.* **101**, 053114 (2012) [doi: 10.1063/1.4740083]

2. Sangmin An, Mun-heon Hong, Jongwoo Kim, Soyoung Kwon, Kunyoung Lee, Manhee Lee and Wonho Jhe, "Quartz tuning fork-based frequency modulation atomic force spectroscopy and microscopy with all digital phase-locked loop", *Rev. Sci. Instrum.* **83**, 113705 (2012) [doi: 10.1063/1.4765702]

3. Jongwoo Kim, Baekman Sung, Byung I. Kim and Wonho Jhe, "Optimization of force sensitivity in Q-controlled amplitude-modulation atomic force microscopy", *J. Appl. Phys.* **114**, 054302 (2013) [doi: 10.1063/1.4817279]

4. Sangmin An, Kunyoung Lee, Bongsu Kim, Jongwoo Kim, Soyoung Kwon, Qhwan Kim, Manhee Lee and Wonho Jhe, "Compensation of stray capacitance of the quartz tuning fork for a quantitative force spectroscopy", *Curr. Appl. Phys.* **13**, 1899 (2013) [doi: 10.1016/j.cap.2013.07.024]

5. Baekman Sung ‡, Jongwoo Kim ‡, Corey Stambaugh, Sung-jin Chang and Wonho Jhe, "Direct measurement of activation time and nucleation rate using non-contact atomic force microscopy", *Appl. Phys. Lett.*, **103**, 213107 (2013) [doi: 10.1063/1.4832879]
(‡ Both authors are equally contributed to this work.)

6. Jongwoo Kim, Donghyun Won, Baekman Sung, Sangmin An and Wonho Jhe, "Effective stiffness of qPlus sensor and quartz tuning fork", *Ultramicroscopy*, under review

7. Jongwoo Kim, Donghyun Won, Baekman Sung and Wonho Jhe, "Observation of universal solidification in the elongated water nanomeniscus", *J. Phys. Chem. Lett.*, accepted

International Conferences

1. "Time resolved lateral dynamic force microscopy for exploring nanoscopic water bridge",

Jongwoo Kim, Sungjin Chang, Baekman Sung, Soyoung Kwon, Gun-Sik Park, and Wonho Jhe, American Physical Society 2010 March Meeting, (March 15-19, 2010 in Portland, OR, USA)

2. "Dynamic Features of Damping Process due to Capillary Condensation", Soyoung Kwon, Sungjin Chang, Baekman Sung, Jongwoo Kim, and Wonho Jhe, 13th International Conference on Non-Contact Atomic Force Microscopy (July 31-August 4, 2010 in Kanazawa, Japan)

3. "Time-resolved study of phase transition in the nanoscale water bridge", Jongwoo Kim, Baekman Sung, Sung-Jin Chang, Soyoung Kwon, and Wonho Jhe, The 6th Annual Water Conference on the Physics, Chemistry and Biology of Water (October 20-23, 2011 in West Dover, VA, USA)

4. "Studies of the Phase Transitions of Nanoscale Water Bridges", Donghyun Won, Jongwoo Kim, Baekman Sung, and Wonho Jhe, International 3rd THz-Bio workshop, (February 2-6, 2012 in Seoul, Korea)

5. "Lateral Dynamic Force Microscopy based on Quartz Tuning Fork for Study of Nanoscopic Liquid Bridges", Jongwoo Kim, Baekman Sung, Donghyun Won, Soyoung Kwon, and Wonho Jhe, "15th International Conference on non-contact Atomic Force Microscopy (nc-AFM 2012) (July 1-5, 2012 in Český Krumlov, Czech)

6. “Dynamics of Electrical-driven Quartz Tuning Fork”,

Donghyun Won, Jongwoo Kim, Baekman Sung, and Wonho Jhe, ”15th International Conference on non-contact Atomic Force Microscopy (nc-AFM 2012) (July 1-5, 2012 in Český Krumlov, Czech)